NASA CONTRACTOR REPORT

NASA CR-1268

EVALUATION OF VACUUM UV DETECTOR-SPECTROSCOPY SYSTEMS FOR CAPSULE REENTRY MEASUREMENTS

by Ronald L. Ohlhaber, Mark W. P. Cann, and Harold V. Watts

Prepared by
IIT RESEARCH INSTITUTE
Chicago, Ill.
for Langley Research Center

NATIONAL AERONAUTICS AND SPACE ADMINISTRATION • WASHINGTON, D. C. • FEBRUARY 1969

NASA CR-1268

EVALUATION OF VACUUM UV DETECTOR-SPECTROSCOPY SYSTEMS FOR CAPSULE REENTRY MEASUREMENTS

By Ronald L. Ohlhaber, Mark W. P. Cann, and Harold V. Watts

Issued by Originator as IITRI Report V6045

Prepared under Contract No. NAS 1-7481 by
IIT RESEARCH INSTITUTE
Chicago, Ill.

for Langley Research Center

NATIONAL AERONAUTICS AND SPACE ADMINISTRATION

For sale by the Clearinghouse for Federal Scientific and Technical Information
Springfield, Virginia 22151 – CFSTI price $3.00

PREFACE

This technical report was prepared by IIT Research Institute, Chicago, Illinois 60616, for the National Aeronautics and Space Administration, Langley Research Center, on Contract No. NAS1-7481. The program was under the direction of the Thermal Measurements Section.

Personnel who have contributed to this project include, M. W. P. Cann, R. Marshall, R. L. Ohlhaber and H. V. Watts.

CONTENTS

FIGURES

TABLES

EVALUATION OF VACUUM UV DETECTOR-SPECTROSCOPY SYSTEMS FOR CAPSULE REENTRY MEASUREMENTS

By Ronald L. Ohlhaber, Mark W. P. Cann, and Harold V. Watts
IIT Research Institute

SUMMARY

During this program various vacuum ultraviolet detector-spectroscopy systems that could be employed for spectroscopic measurement of the shock wave created ahead of a capsule experiencing hypervelocity reentry conditions were analyzed and evaluated. A generalized set of measurement requirements and environmental conditions is established for a 50,000-ft/sec entry velocity. These conditions are then used to evaluate such detector-spectroscopy systems as ion chambers, proportional counters, Geiger-Mueller tubes, photoelectric tubes, wavelength shifters, photoconductive cells, photovoltaic cells, reverse biased diodes, miniature photodiode arrays, and photoelectric cathode with retardation grid analyzers. The most favorable system appears to be a wavelength dispersing device (grating) followed by an electronically scanned miniature detector array. The array elements could be chosen from either photodiodes, phototransistors, or photoconductors, whichever shows the best vacuum ultraviolet response.

I. INTRODUCTION

The results obtained on a study program delineating vacuum UV spectroscopy systems for possible use in reentry test bodies are reported herein. The general mission application is for Mars or Venus return vehicles reentering from hyperbolic orbit at entry velocities in the range 40,000 to 60,000 ft/sec. Before considering specific spectroscopy systems, it is necessary to define the measurement requirements and the conditions under which the measurements must be made. Each detector-spectrometer system is then evaluated with respect to the derived environmental conditions. The various detectors are gas ionization, photoelectric, photoconductive, photovoltaic, reversed biased diode, wavelength shifter, miniature photodiode array, and photoelectric cathode with retardation grid analyzer. The evaluations are based on simplicity and reliability, with consideration given to such other factors as form of data, size and weight of instrumentation, and cost. A determination of the most promising system is made and preliminary design of this system pursued.

II. MEASUREMENT REQUIREMENTS

A. Capsule Conditions

Configuration

As no specific mission has been defined for this study program, we have adopted the capsule configuration as proposed previously by Cauchon.[1*] Figure 1 shows the two contemplated body nose shapes. Drag coefficients are the only significantly different parameters resulting from these shapes. These differences will undoubtedly affect both the capsule attitude during reentry and features of the wake shock wave but are expected to have only a secondary effect on properties of the bow wave. Body A (blunt) is used in this study as the typical capsule shape. The principal dimensions of the capsule are

$R_N(A)$ body nose radius: 1.91 ft,

A Projected frontal area: 1.99 ft^2,

C_D drag coefficient: 1.5 .

Conforming with Cauchon's analysis, we adopted a nominal capsule weight (W) of 100 lb and a mean density of 64 lb/ft^3, which leads to a homogeneous volume (V) of 1.55 ft^3. However, a calculation based on the capsule dimensions yields a volume (V) = 0.82 ft^3. Our preliminary analysis will be based on a usable capsule volume of 1 ft^3.

The capsule configuration chosen represents only a starting point for our considerations. There is apparently a disagreement concerning the energy transfer characteristic of variously shaped bodies. Page and Arnold[2] state that about 10 percent of the total kinetic energy is transferred into a blunt body whereas, according to Seiff and Tauber[3], conical bodies typically show only a one percent transfer. According to Sullivan[4] the apparent advantage of the conical capsule is not realistic. In any event, we have chosen the worst conditions: a system capable of working under blunt capsule conditions will operate in the possibly more favorable conical body.

Progress in rocket technology indicates that a large capsule (up to 3 feet in diameter) will probably be available when flight experimentation is attempted. This study must be sufficiently flexible to accomodate such improvements, although new developments may relax tolerance requirements of the system.

*Indicates reference.

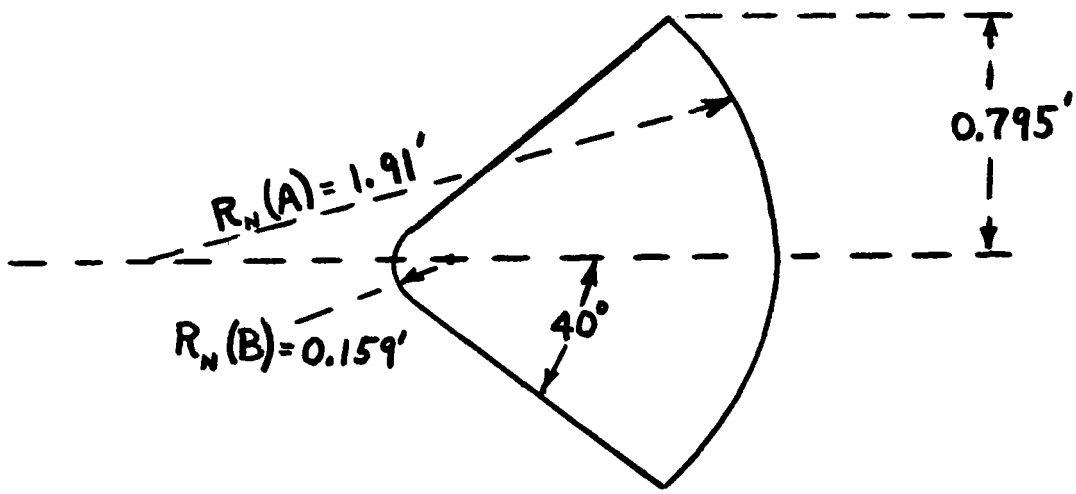

Body A (Blunt)	Body B (Cone)
Density $\approx$ 64 lb/ft^3	Density $\approx$ 64 lb/ft^3
Weight = 100 lb	Weight = 100 lb
M/C_DA = 1.0 slugs/ft^2	M/C_DA = 1.76 slugs/ft^2
C_D = 1.5	C_D = 0.85
A = 1.99 ft^2	A = 1.99 ft^2

R_N = Body nose radius

FIGURE 1. ASSUMED CAPSULE NOSE SHAPES AND PROPERTIES

General Features

It is probable that in an actual measurements mission, some observations of the "clean" shock front will be necessary. In the "Project Fire" experiments, the capsule forebody was composed of alternate layers of ablative materials (Teflon, polycarbonate phenolic asbestos) and calorimetric layers (generally metals such as beryllium). Through careful choice of material types and thicknesses, reentry observations were divided into clean spectral regions and measurement-blocking periods.

In the present study we have ignored the effects of ablative contamination, but we have considered introducing measurement-blocking periods. We have assumed also that the body nose radius, R_N, is fixed for the entire reentry period, although in reality R_N will change as ablation proceeds. We indicate our awareness of these factors but consider them of secondary importance in this preliminary study.

Forebody Orifice

The choice of forebody orifice is dependent on several factors. These include:

(a) Limitation of the radiative input to maintain acceptable intensities at the detector-spectroscopy system plane and avoid complexities such as ablation and/or excessive temperatures within the sampling cavity;

(b) The size of such orifice must not materially affect the gas-cap flow field (see work of Slocumb and Buchan[5]);

(c) The field of view must encompass a significant portion of the stagnation region if reliable data are to be obtained. With these considerations the work statement has stipulated a maximum orifice diameter of d_j = 3/16 in.

Helium Window

The provision of an optical path in the vacuum ultraviolet region poses severe problems. Solid transmission windows for entire coverage of the spectral region 2000Å to 500Å do not exist. Ceramic luminescent windows (for example MgO) employing a wavelength shifting feature are a possibility but

factors such as the retention of such windows for sufficient observation time and the complexities of calibration limit their use at the present time. Moreover, at the high reentry velocities ($>$ 40,000 ft/sec) radiative heating becomes predominant and the requirement of convective isolation between the gas cap and measurements system becomes less stringent. With these factors in mind, more serious consideration has been given to the use of effluxing gas windows.

Slocumb and Buchan[5] performed a preliminary feasibility study of the helium window system, which is suitable for the spectral range of interest because Helium is essentially transparent at wavelengths greater than 500Å. The results obtained by these scientists demonstrate that the sampling cavity overpressure can be maintained through the entire bow wave pressure-time profile and that the window function will not seriously influence the gas-cap flow field. The performance of the window is not yet optimum since a fixed overpressure for the duration of the bow shock wave is required. The best performance to date of several windows studied by these scientists had the following characteristics:

d_j: Orifice diameter 3/16 in.

P_1: Supply tank pressure 1200 psi

ΔP: Overpressure in the cavity nominally set at 1.0 psid.

The characteristics of this window system are shown in Figure 2 under conditions of a shock pressure P_3 which simulates the pressure-time profile for a blunt body entering the atmosphere at 50,000 fps.

The pressure regulator is a very important component of the gas window and improvements in the window performance may well originate in this part of the system. Principal features of the regulator designed and tested by Slocumb and Buchan are

Outlet pressure regulation response time is 20 msec

Flow of 100 $\pm$ 10 liters/min at 1.5 $\pm$ 0.5 psid

Inlet pressure of 200 to 3000 psi

Operational temperature range is 0° to 160°F

Regulator weight less than 1.40 lb.

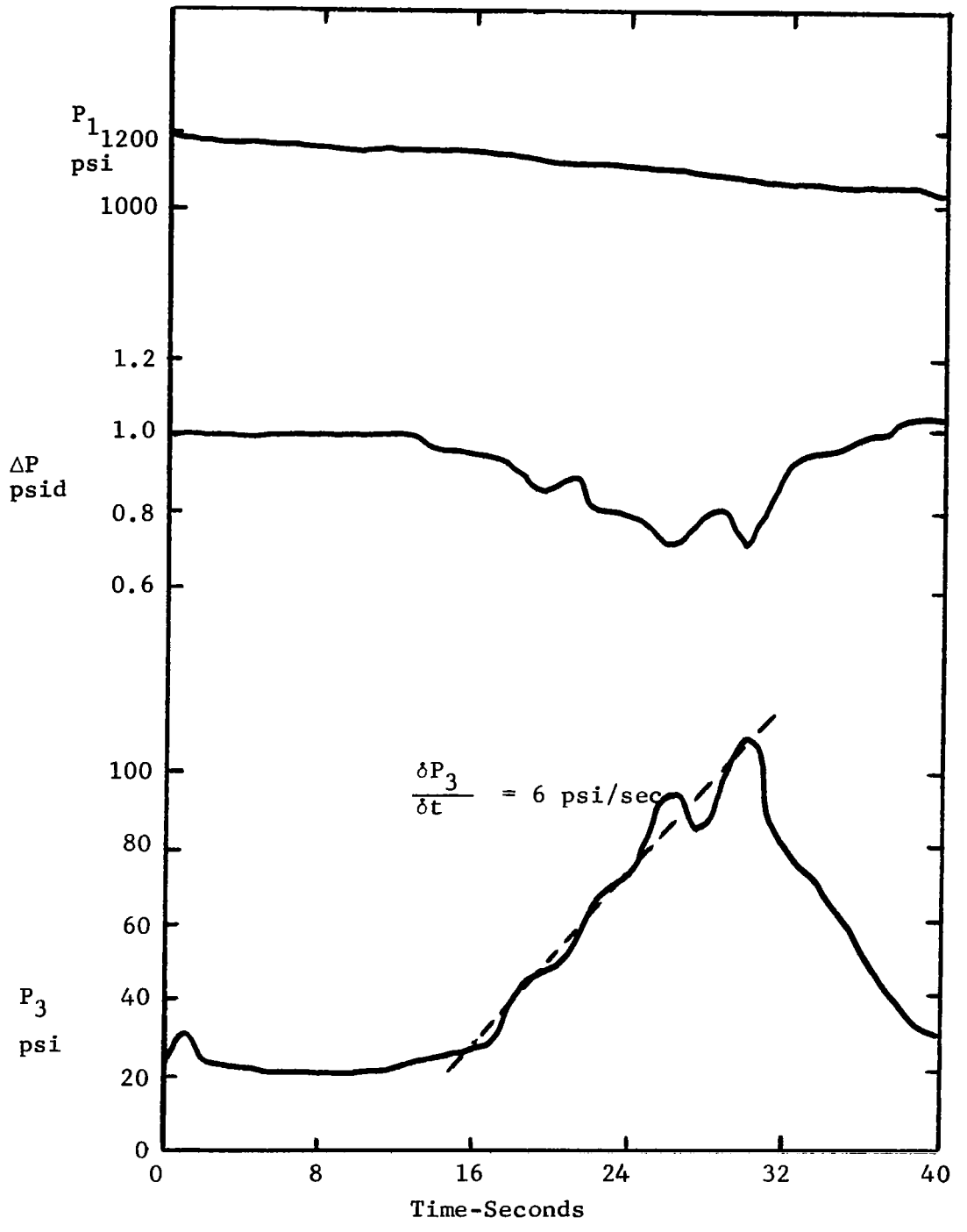

FIGURE 2. PERFORMANCE OF EFFLUXING GAS WINDOW

At this stage of the study we will assume that the characteristics of the gas window to be used in the actual flight experimentation are similar to those listed above.

The work statement has indicated a typical pressure differential of 10 psid which is substantially higher than those quoted here. Pressure differentials of this magnitude still will not disturb the flow field and would provide additional cooling and sweeping of ablative material; however, this would involve a significantly larger capacity system which probably could not be justified on actual window performance. We will thus assume that the lower (~1.0 psid) pressure differential is more appropriate.

Instrument Cavity

The regulator flow rate is set at a 100 liters/min maximum and we assume that the overpressure must be maintained for a maximum time of about 2 min. This gives a 200-liter total flow. A reasonable storage tank volume then is about 500 liters.

Referring to Figure 2, we see that from P_3, the simulated pressure-time profile typical gradients are of the order 6 psi/sec. Within the response time of the regulator (20 msecs) the pressure adjustment must be 0.12 psi and discharge 0.033 liters of gas at 1200 psi pressure. A volume of about 1.5 liters or 10 cubic inches will satisfy this requirement. Thus, a sample cavity of dimensions

Height:	2 in.,
Width:	2 in., and
Depth:	2-1/2 in.

will be used in these initial calculations.

Auxiliary Onboard Equipment

The capsule must accommodate support equipment for the helium window, data storage and telemetry facilities, tracking equipment, a refrigeration system, remote communication equipment, and internal power sources. The allowable capsule diameter, which is provisionally fixed at 2 feet, will probably have increased to about 3 feet by the time flight experimentation is attempted. Nevertheless, it is obvious that capsule space is an overriding consideration. The chosen spectroscopy system must combine simplicity of operation with compactness and require a minimum amount of auxiliary equipment.

B. Instrument Requirements

Spectral Coverage

Complete spectral coverage over the range 2μ to 500Å will probably be required in the actual mission. The region of interest in this study is the vacuum UV from 2000Å to 500Å. The lower limit is set by absorption of the helium resonance lines.

Resolution

It is assumed that a primary purpose of the mission under consideration is to determine the total radiative heat input. Thus the initial resolution requirements are not stringent and a 50Å element width is sufficient. It may, however, be necessary to set much higher resolution requirements (~2Å) if there is need to identify molecular species in the shock front. This would impose constraints on the choice of the spectroscopy system -- a simple system is sought that is amenable to resolution increase without significant sophistication.

Scan Rate

As will be discussed later in this report, the duration of the heat pulse is anticipated to be about 80 sec. A scan time of 5 sec (2000Å to 500Å) is acceptable as an initial goal. If 100 intensity units are sufficient to characterize the spectrum and assuming the 50Å resolution element, provision must be made for storing and subsequently telemetering 1.2×10^6 spectral inputs for the vacuum UV measurements.

Intensity Range

This subject is also discussed in detail later. In terms of radiation entering the cavity, the upper intensity limit is of the order 50 watts per 50Å element at the peak of the heat pulse. At the onset of equilibrium (~ 24 sec into the heat pulse) the intensity levels are about four orders of magnitude lower.

C. Flight Conditions

General Conditions

The conditions to be simulated in flight experimentation will be typical of those anticipated for reentry after

completion of a Mars or Venus mission. Direct reentry is assumed with the following conditions applying:

Reentry Velocity V_∞ : 50,000 fps (some calculations are presented for the 40 to 60 thousand fps range)

Angle of Attack: 0°.

Reentry Angle j: -15° (already there are indications that heating will be considerable relaxed at -12° entry angle).

Maximum Acceleration: 50g

Reentry Altitude h_0 is assumed to start at 400-thousand feet

In our original considerations we had used extensively the results of Cauchon[1] pertaining to the reentry conditions. However, it appears that the mission conceived by Cauchon and reported in March 1966, is no longer considered feasible. Primary difficulties stem from the nature of the trajectory which yields impossible g-loads and capsule heat inputs. Moreover, improved shock-front radiation calculations indicate considerable lower emittances than those calculated by Cauchon. An intermediate condition has been agreed to, whereby a Cauchon-type condition will apply to survivability. Thus the system functioning within these requirements will have a considerable safety margin in the real situation. The measurement conditions, on the other hand, will be set by the conditions imposed by a more realistic trajectory.

Trajectory Calculations

In Figure 3 the force diagram used in the trajectory calculations is shown. The equations of motion for computing the trajectory are[6]

$$M \dot{V} = - D - Mg \cos \theta$$

$$M V (\dot{\phi} + \dot{\theta}) = -L + Mg \sin \theta$$

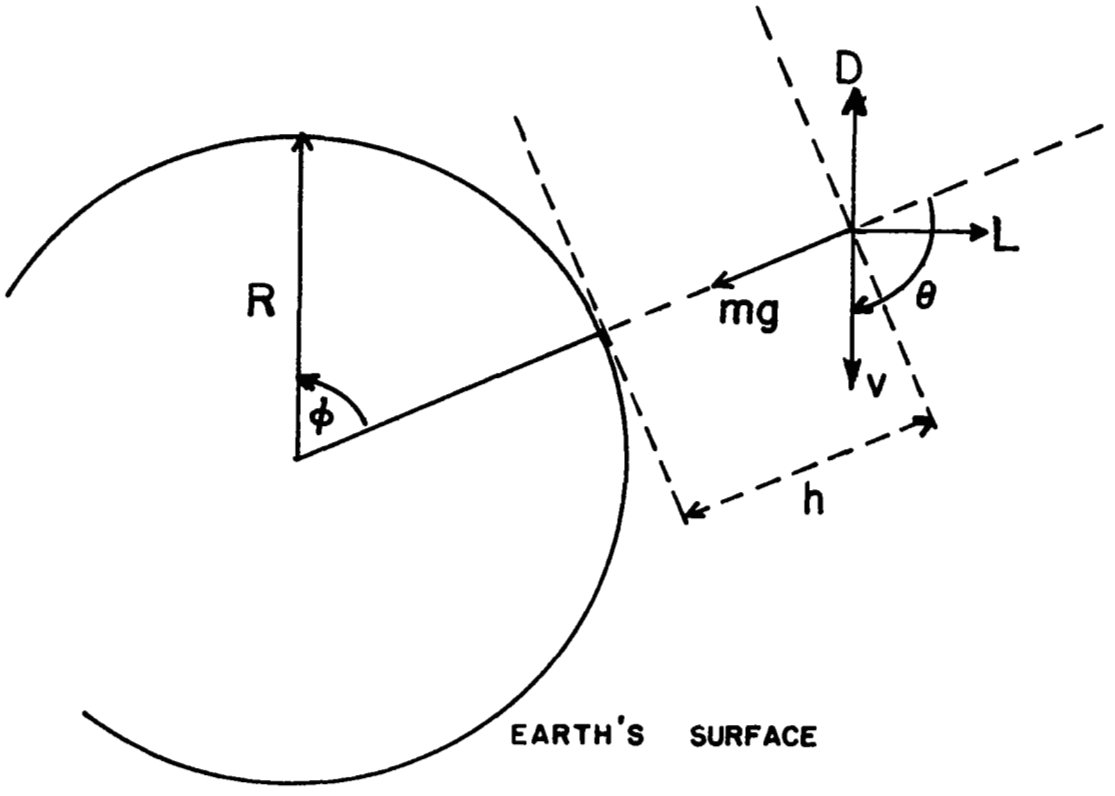

FIGURE 3. FORCE DIAGRAM FOR TRAJECTORY CALCULATIONS

$$(R + h)\,\dot{\phi} = V \sin\theta$$

$$\dot{h} = V \cos\theta$$

where

$$g = g_0 \left(\frac{R}{R + h}\right)^2$$

$$D = \frac{1}{2} C_D(\alpha)\, \rho(h)\, V^2 A$$

$$L = \frac{1}{2} C_L(\alpha)\, \rho(h)\, V^2 A$$

and $\rho(h)$: the atmospheric density profiles with h the height above the earth's surface

$C_D(\alpha)$: drag coefficient

$C_L(\alpha)$: life coefficient

α: angle of attack

A: effective cross-sectional area of vehicle

M: vehicle mass

V: vehicle velocity

R: Earth's radius

Several simplifications are possible. At a height of 400,000 ft, $g = 0.963\, g_0$; hence, take g as constant. Now the equations become

$$\dot{V} = -\left[\frac{M}{C_D A}\right]^{-1} \rho \frac{V^2}{2} - g \cos\theta$$

$$V(\dot{\theta} + \dot{\phi}) = g \sin\theta$$

$$\dot{h} = V \cos\theta$$

$$(R + h)\,\dot{\phi} = V \sin\theta$$

These equations were solved approximately by step-wise integration for the following zero-lift situation:

$h_0 = 400{,}000$ ft

$V_E = 50{,}000$ ft sec^{-1}

$\Phi_0 = 0$ - arbitrary

$\theta_0 = 105°$

$$\frac{M}{C_D A} = 1.0 \text{ slug ft}^{-2}$$

$$= 1.99 \text{ ft}^2$$

$L = 0$

$\alpha = 0.$

The values of $\rho(h)$ were obtained from Ref. 7. This corresponds with the blunt configuration shown in Figure 1 at zero angle of attack. The calculation was performed in steps of 10,000 ft down to 250,000 ft, and then in steps of 2,000 ft. The results are shown in Figure 4. This trajectory serves as an example: others can be computed using the same method, although it would be more economical to use a computer if several were required. Cauchon does not give full information on the trajectory to be used; however, his altitude-time plot is also shown in Figure 4. The discrepancy between these two curves is not understood - the one calculated here is in qualitative agreement with others (e.g., compare Figures 5 and 6). Reducing the entry angle would decrease the stresses encountered. Further reduction in the g-loads can be achieved by using a lifting body - if modulated lift is introduced, then it is possible to increase the entry corridor further[8]. Pritchard[8] considered the effect of lift on corridor width* (Figure 7). Pritchard's calculations were for a vehicle with constant $(M/C_L A) = 4.66$ slug ft^{-2} (the figure suggests that maybe this should be $(M/C_D A)$ for $(L/D) = 0$ with undershoot defined for a maximum of 12 g deceleration. Although this situation is somewhat different than the one just considered, Figure 7 shows that in the speed range 40,000 to 60,000 ft/sec it may not always be possible to obtain a sufficiently large entry corridor without using aerodynamic lift or retrobraking.

*Corridor width is defined as the difference in vacuum perigee of the two limiting trajectories: undershoot, set by the maximum acceptable g-load and overshoot, beyond which the vehicle is not captured. Some variations have been used; e.g., overshoot set by limiting trajectory that reaches the same target as the undershoot[6].

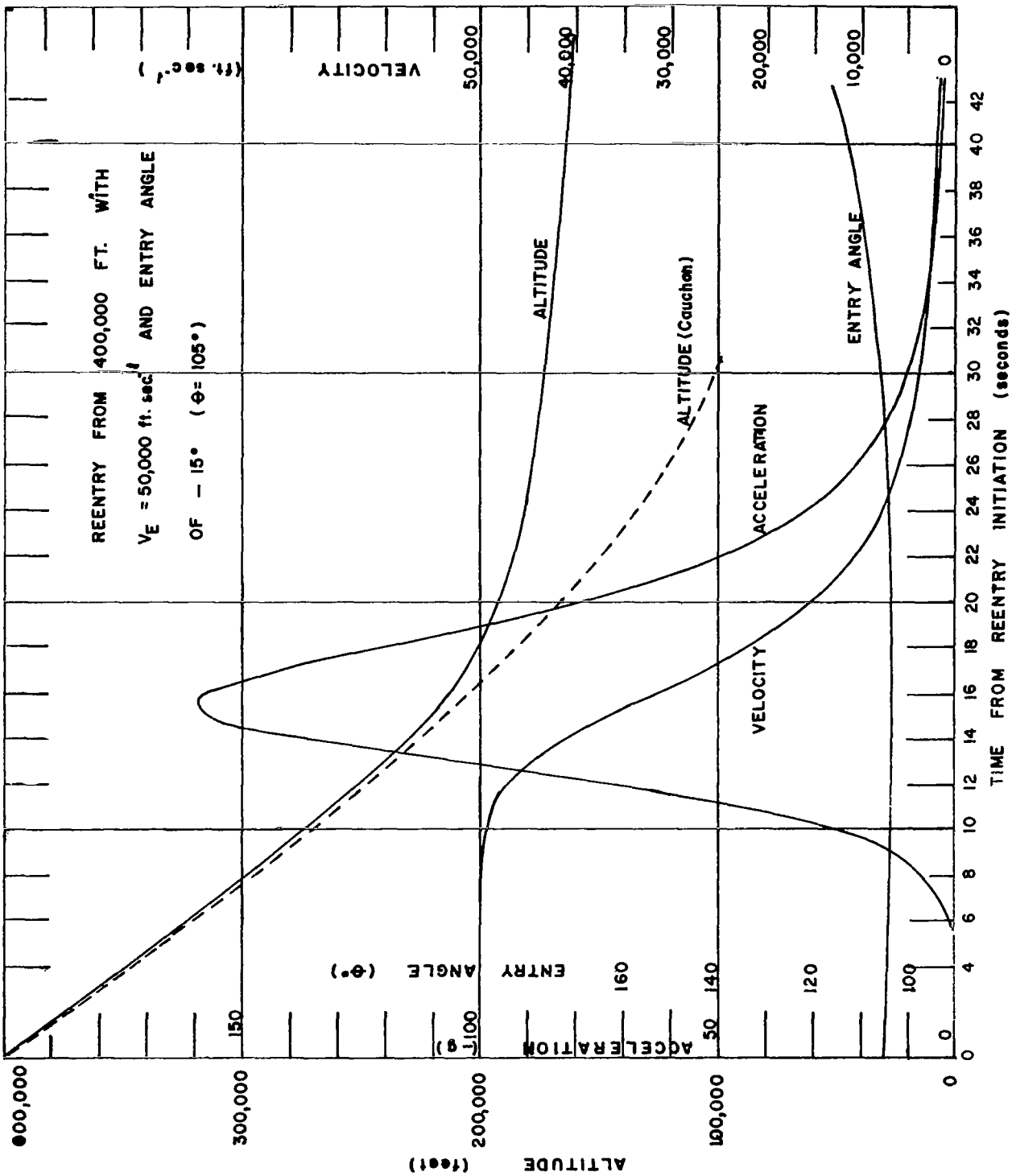

Figure 4. Reentry from 400,000 ft. with Velocity of 50,000 ft/sec.

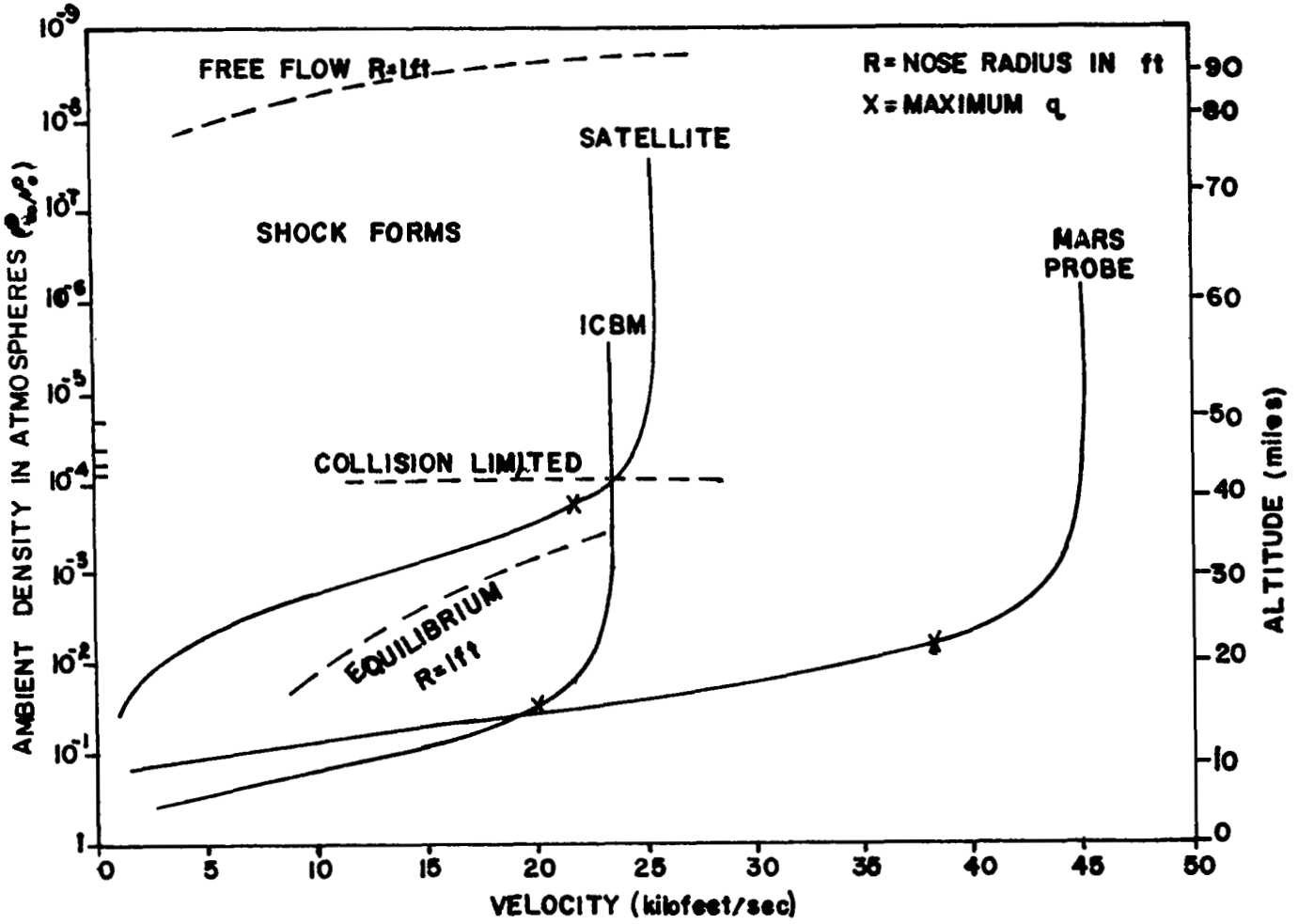

FIGURE 5. RADIATION REGIMES. (TAKEN FROM REF. 14)

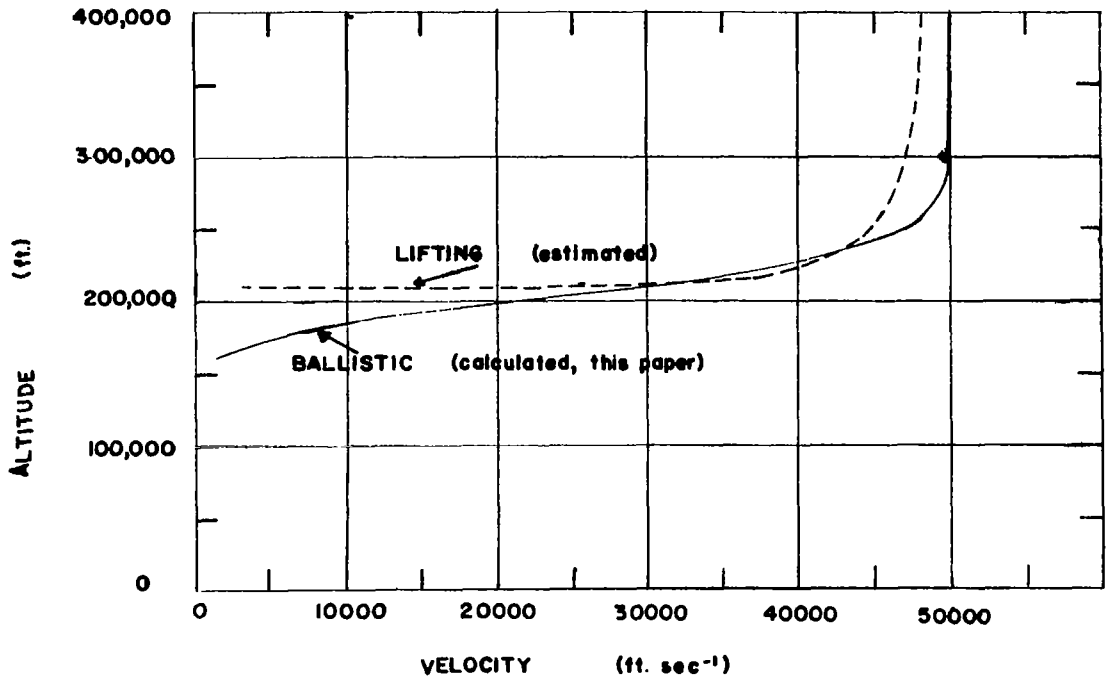

FIGURE 6. REENTRY TRAJECTORIES. THE LIFTING TRAJECTORY WAS DRAWN TO GIVE A FLAT REGION AT 210,000 ft.

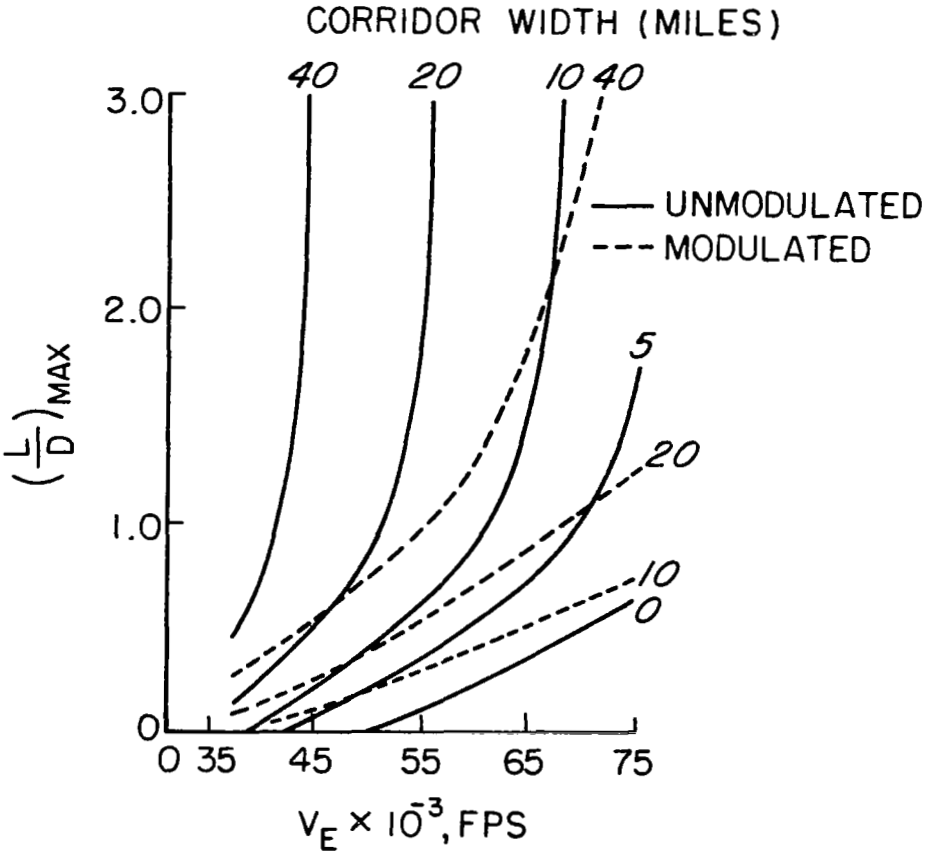

FIGURE 7. EARTH ENTRY CORRIDOR WIDTH CAPABILITIES[8]

Flow Field

During the entry phase the vehicle gas cap is bounded by the bow shock which compresses and heats the gas. Behind the shock wave (i.e., in the gas cap) the heated gas flows toward and around the nose of the vehicle. The flow, initially laminar, becomes turbulent at some point -- similarly for the boundary layer established on the surface of the vehicle. The initially hot gas relaxes to equilibrium during this flow process, resulting in dissociation, excitation, ionization, and the formation of new chemical species. Thus the state of the gas varies from the shock front along the stream lines. Since rate processes are strongly dependent on pressure and temperature, the uniformity of the gas will vary with vehicle altitude and speed.

Calculations for certain cases have been published [9,10,11], and summaries of progress in this field have been given by Seiff[12] and by Eggers and Cohen[13] which include more general modes of planetary entry than of concern here. The solutions provided by Lomax and Inouye[9] are for altitudes in the range 100,000 to 300,000 ft and velocities from 10,000 to 45,000 ft/sec -- steady inviscid flow is assumed, and heat conduction and radiation effects are neglected. Howe and Viegas[10] consider radiation effects and include results for velocities up to 50,000 ft/sec at 250,000 ft; however, their published results are presented in the form of a few graphical examples and are not extensive enough to follow a particular trajectory.

The problem of finding flow-field information to evaluate the state of equilibrium of the gas and its radiation emission has been avoided at this time.

Stress Conditions

The reentry vehicle is subject to stresses of various kinds generated by aerodynamic forces. The spectroscopic instrument package, in particular, is subject to the following stresses:

(a) Thermal stresses: due to heat transfer from the gas cap.

(b) g-stress: due to the deceleration experienced by the vehicle.

(c) Vibration: generated by the aerodynamic forces.

(d) Acoustic load: also generated by the aerodynamic forces. This may be considered a higher frequency variant of (c).

The study to date has been concerned primarily with thermal stresses although some coarse estimates of the g-loads have been made. In the following section, the gas cap radiative and convective properties are discussed in detail.

D. Shock Front Radiation

Active Processes and Kinetics

The various radiation regimes encountered during reentry have been discussed by Kivel[14] and are summarized in Figure 5, which is a modified version of a figure in Kivel's paper.

(a) Free molecule flow: air molecules have a mean free path which is of the order of or greater than a typical vehicle dimension (say, the nose radius). No shock wave is formed in the stagnation region.

(b) Collision limited radiation: as the air density increases from the conditions of (a), a shock wave is formed. At these low-air densities the population of excited states by collisions is slower than the depopulation by radiation. Hence, the intensity of the radiation is dictated by the collisional excitation rate. The altitude at which collision limiting is of importance depends on the radiative lifetime as well as on the density, and therefore varies with the wavelength -- the line shown in the figure is for a lifetime of 10^{-7} sec.

(c) Chemical Nonequilibrium: The shock-heated gas takes a finite time to relax to equilibrium. This process

is accompanied by excitation, dissociation, ionization, and the formation of new molecules. During this time the gas temperature falls and the density increases. Figure 8 shows the effect of pressure on the temperature profile: it is seen that at low densities the whole region in front of the stagnation point may be in chemical nonequilibrium. In fact, profiles such as those shown exist along each streamline. The radiation intensity profile is similar to the temperature profile due to an overshot of nitric oxide polulation during nonequilibrium. An experimental study of the nonequilibrium radiation in the bow shock layer has been reported by Canning and Page[15]. These authors observed the truncation effects shown in Figure 8.

(d) Equilibrium: In general, the solution of the radiative heat transfer problem must take into account radiation absorption and decay of shock layer energy. However, if the rate of energy loss is not too large the shock layer has a uniform temperature, after the nonequilibrium region, and the emitted radiation intensity is the same throughout. If the radiative flux is comparable with the energy flux of the flow entering the shock layer, then radiation cooling has to be considered. This cooling results in a decay of shock layer energy, and a decrease in radiation flux. In addition to these two cases there are two similar cases in which radiation absorption has to be included. Wick[16] identifies the following four categories:

i) no shock layer decay or radiation absorption
ii) decay only
iii) absorption only
iv) decay and absorption.

Wick shows, qualitatively, where these various effects have to be included: this depends on vehicle shape,

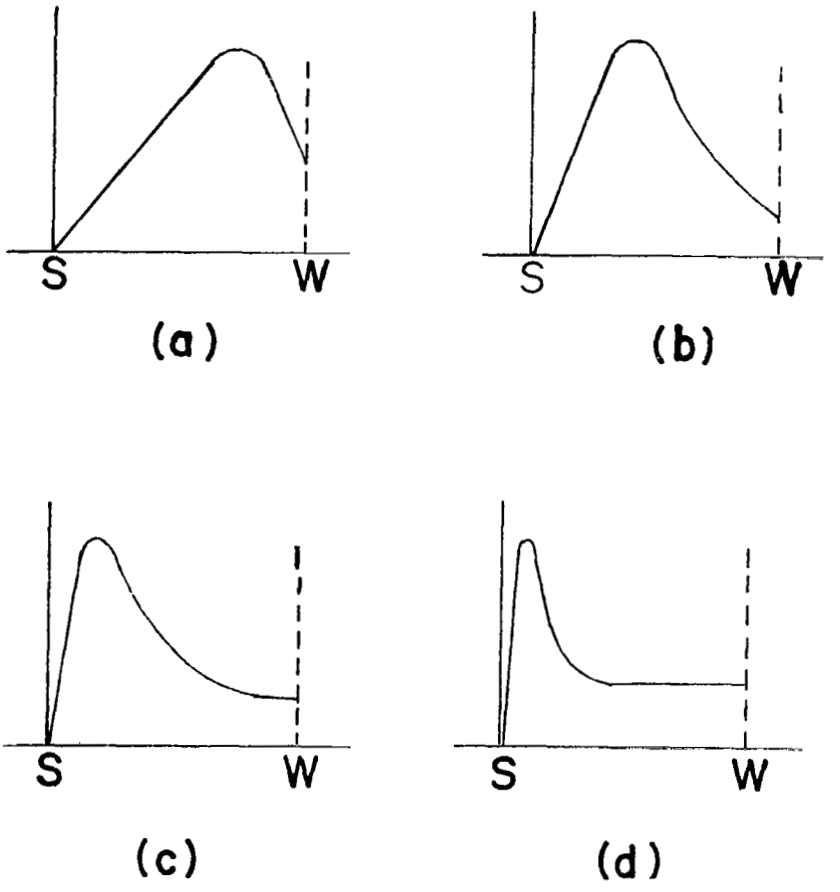

FIGURE 8. TEMPERATURE PROFILES SHOWING TRUNCATION DUE TO CHEMICAL NONEQUILIBRIUM. ALTITUDE DECREASING: (a) to (d) S: Shock Front W: Wall

size, and angle of attack. He also gives a discussion of the quantitative aspects. Figure 9 shows the important radiation regimes, as given by Wick. It is seen that for a Mars return vehicle, item (i) above (adiabatic case) should be excluded altogether, so that decay and absorption must be included in the calculations.

The numerical values for the radiation emission from hot air which have been used to the largest extent are those published by Allen[17]. The uncertainty in these figures is quite large; the authors consider a factor of two to be quite possible.

Heat Input to Cavity

In the projected experiment the spectroscope views the gas cap through a small hole (about 3/16-in. diameter) in the heat shield at the stagnation point. Ingress of air and ablation material is prevented by an outward flow of helium, which also maintains the optical path inside the capsule free from gases which absorb in the spectral range of the experiment. The thermal stresses set up in the instrument package are determined, among other things, by the entry history of the heat transfer from the gas cap through the viewing port in the vehicle heat shield. The relative magnitudes of convective and radiative heat transfer depend on the entry velocity, altitude, vehicle shape, and angle of attack. It has been shown by several authors [4,18,19,20] that, for initial velocities in the range 40,000 ft sec-1 and upwards, the radiative heat transfer dominates convective heat transfer during the peak heating period, thus, for entry velocities in this range, convective heat transfer may be neglected in many cases. Although convective heat transfer dominates during the early and late phases of the entry period, during the peak heating period it is the radiative component that matters most. Hence, convective heat transfer will be neglected here.

The complete solution of the radiative heat transfer problem is complex. A bow shock is established in front of the vehicle and this heats the air to a high temperature. The heated air follows streamlines which flow to either side of the stagnation region and establishes a boundary layer over the surface of the vehicle. The air, when it has just been shock heated, is at a kinetic temperature considerably in excess of the equilibrium value but does not radiate since the energy is in a kinetic mode. Relaxation to equilibrium occurs

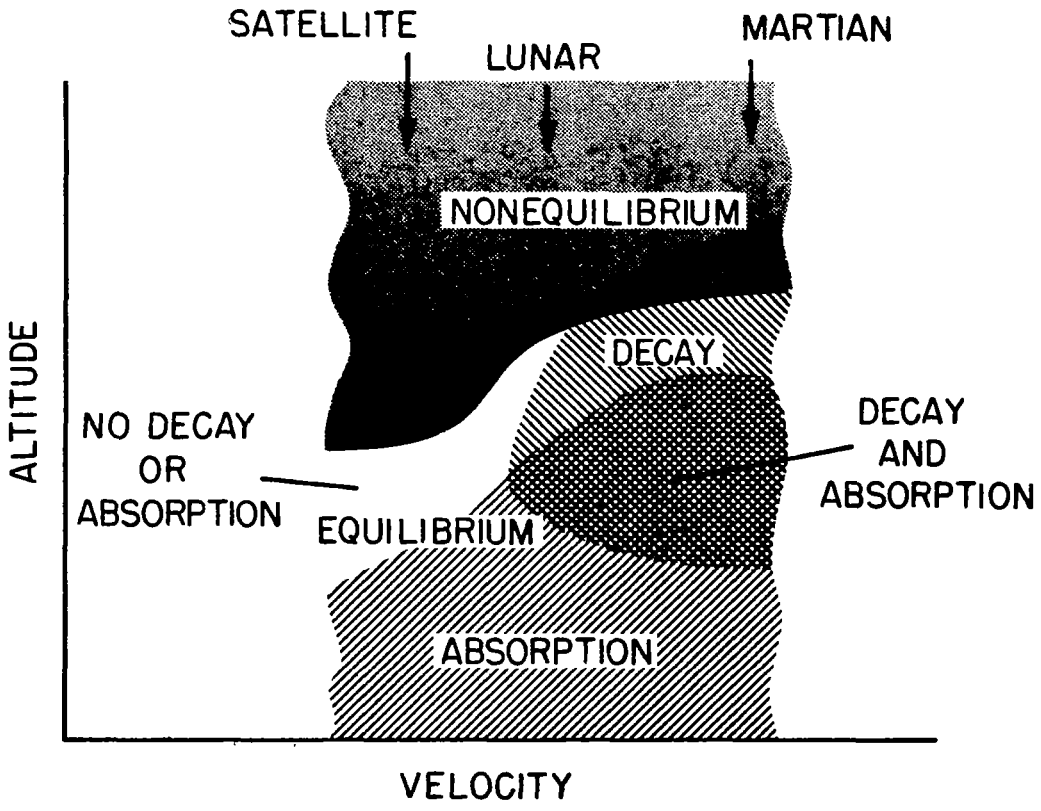

FIGURE 9. ALTITUDE-VELOCITY REGIME

with the generation of excited, dissociated, and ionized species which radiate strongly -- at the same time the kinetic temperature falls due to the redistribution of energy. This relaxation to equilibrium takes a finite time, during which the relaxing gas is traveling along streamlines towards and around the vehicle; furthermore, the rate at which this relaxation occurs depends on temperature and density, and hence on the speed and altitude of the vehicle. It is clear that in the early phase of atmospheric entry much of the radiation reaching the stagnation point of the vehicle will be from regions of chemical nonequilibrium -- this follows from the fact that gas densities are low so that relaxation to equilibrium proceeds at a slow rate.

The complete solution of the problem, solving the Navier-Stokes equations and including radiation transport, is outside the scope of the present report. Consequently, estimates from other sources are considered to find those which are most pertinent to the present problem.

Cauchon has made calculations for reentry at initial velocities of 40,000 to 60,000 ft/sec and angles of -12° and -15°, using the AVCO radiation graphs[17]. The trajectory results in Figure 4 are those of Cauchon's case with an entry angle of -15°. Figure 4 shows that the peak g-load exceeds 150 g, a value which is considerably in excess of the maximum a man can tolerate (10 to 12 g); hence, lower values are of more practical interest for returning-Mars missions, even allowing for a safety margin. Smaller peak deceleration means smaller heat loads since it implies lower velocities at the altitudes where peak decelerations were found for the ballistic trajectory.

It should be noted that the AVCO radiation calculations[17] are for equilibrium conditions, and that Kivel[14] shows that the radiation is collision limited for $(\rho/\rho_o) \lesssim 10^{-4}$ (see Figure 5). This density is achieved at an altitude of 220,000 ft. Therefore, radiation estimates for altitudes of around 200,000 ft and above are probably too large if they are based on equilibrium radiation -- the altitude for collision limiting does depend on spectral region. Thus, it is likely that Cauchon's results are high, even for the cases he considers.

As indicated earlier, we are basing the heat input conditions on a Cauchon-type mission. It is possible that, because of the high input levels and the necessity of examining a "clean" shock front, the spectroscopy system will need to be

closed down for brief intervals during the heat pulse. In Figure 10 we define three measurements regions: Σ_1, Σ_2, and Σ_3. The Σ_2 measurement region is centered around the peak of the heat pulse; Σ_1 and Σ_3 are defined as the start and final regions, respectively, where the heating rate is about 100 w/cm^2.

To calculate cavity temperature (i.e., operating temperature of the spectroscopy system), we must first obtain estimates of the total heat input during the specified measurement periods. In Figure 11 we have replotted Cauchon's calculations of the total heating rate with reentry time for different reentry velocities and at $\alpha = -15°$. Also shown is the curve for a 50,000-fps reentry at an angle of -12°. The convective component is omitted since the gas-window system maintains an efflux of helium through the orifice during the entire heating period.

Heating rates have then been integrated over the whole heat pulse and during the measurement periods. These results, in the form of heat emitted from the shock front, are tabulated in Table 1. It is apparent that the small reduction in reentry angle from -15° to -12° significantly reduces the amount of heat emitted.

As a check on overall consistency, we may compute the above values for Σ_{total} with values obtained by simple kinetic energy considerations. The entering capsule has very high kinetic energy and the potential term is negligible by comparison. The kinetic energy is dissipated in work done on forming and maintaining (i.e., translating) the gas cap. A large proportion of this energy is then lost in radiation from the gas cap. Page and Arnold[2] maintain that for blunt bodies only about ten percent of the total kinetic energy is actually transferred into the capsule in the form of heat. Seiff and Tauber[3] show that, in the case of conical bodies, the heat input may be reduced to about one percent.

The kinetic energy Σ_{ke} may be calculated using the parameters given above, i.e., a reentry velocity (V_∞) of 60×10^3 fps at 400×10^3 feet. We assume* that at 10×10^3 ft. altitude the capsule has a free fall velocity (V_f) of 2.7×10^2 fps and a mass (M) of 100 lb.

$$\Sigma_{ke} = 1/2\ M(V^2 - V_f^2)$$

* A trajectory analysis has been performed by Travis Slocumb (NASA) however, since the kinetic energy varies as the square of the velocity, the choice of the final velocity is not critical.

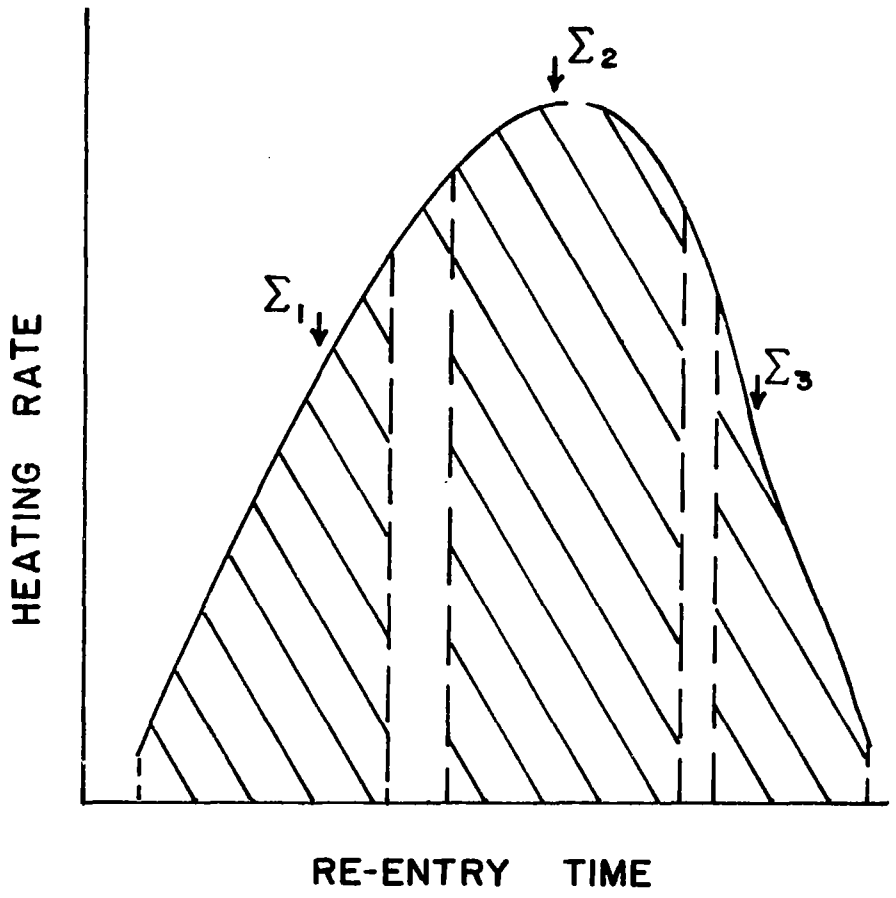

FIGURE 10. MEASUREMENT REGIONS

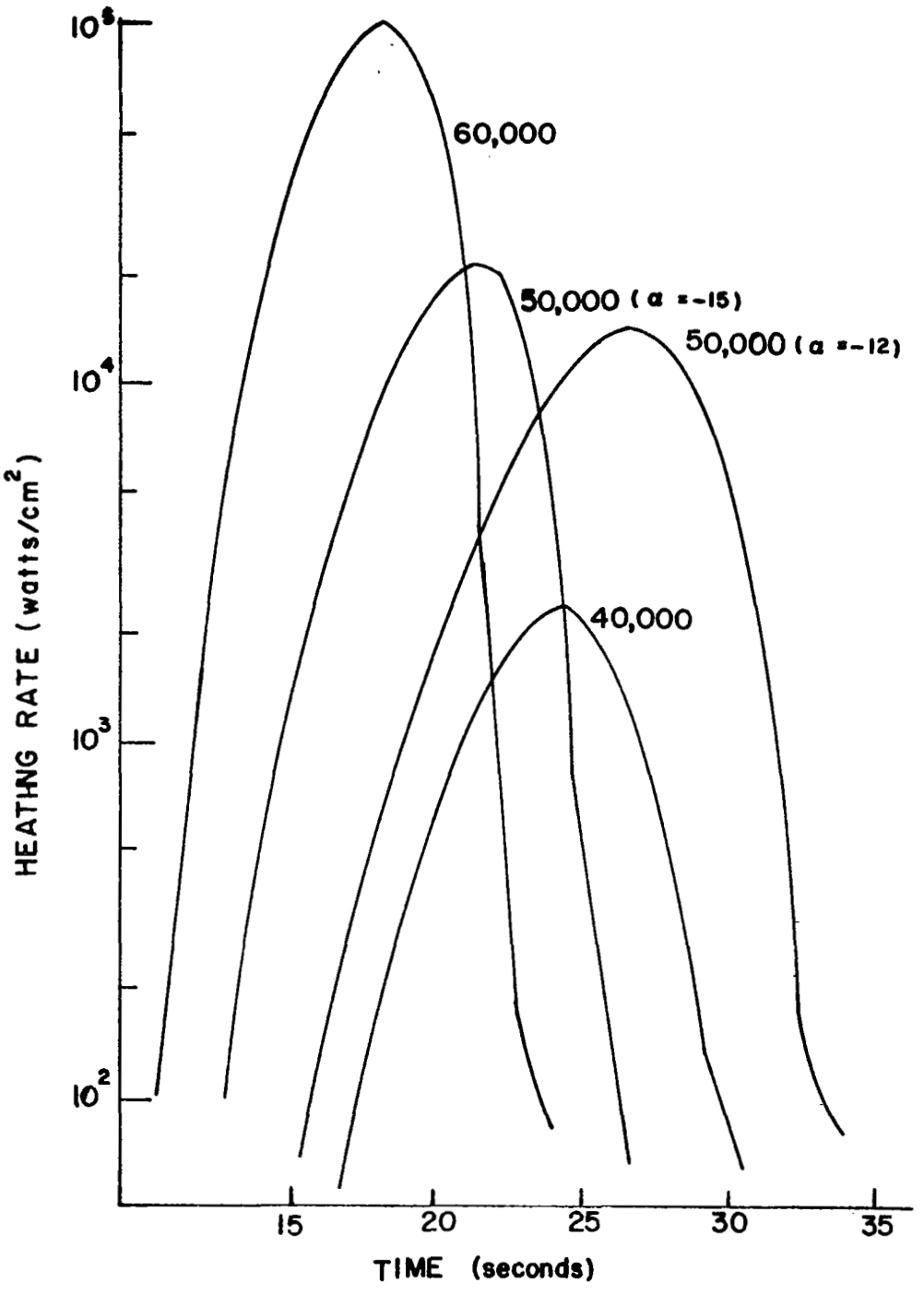

FIGURE 11. TOTAL HEATING RATE DURING REENTRY

Radiant Heat from shock front Joules/cm^2	REENTRY VELOCITY fps			
	Reentry Angle = -15°			= -12°
	60×10^3	50×10^3	40×10^3	50×10^3
Σ_{total}	45.33×10^4 (t = 10 - 24 secs)	10.85×10^4 (t = 12 - 27 secs)	1.31×10^4 (t = 17 - 31 secs)	9.38×10^4 (t = 15 - 34 secs)
Σ_1	2.06×10^4 (t = 10 - 16 secs)	5.02×10^3 (t = 12 - 16 secs)	1.73×10^3 (t = 17 - 21 secs)	1.5×10^3 (t = 15 - 19 secs)
Σ_2	32.9×10^4 (t = 16 - 20 secs)	6.84×10^4 (t = 19 - 23 secs)	8.04×10^3 (t = 22 - 26 secs)	4.99×10^4 (t = 25 - 29 secs)
Σ_3	2.97×10^3 (t = 21 - 25 secs)	1.15×10^3 (t = 23-27 secs)	0.88×10^3 (t = 27 - 31 secs)	1.30×10^3 (t = 30 - 34 secs)

TABLE 1. HEAT EMITTED FROM THE SHOCK FRONT

Using the values previously noted, we obtain 5.62×10^9 foot pounds. The bulk of this energy is dissipated in a period less than 20 sec and on converting ft-lb to joules, the energy dissipated is 4.12×10^8 joules, and therefore, the total input to the capsule is about 4×10^7 joules. The actual dissipation occurs over an area larger than the forebody area and is not constant, being considerably higher in the stagnation region than in flow regions. Stainback[21] for a similar set of conditions has shown that the radiation intensity falls a factor of 3 for θ', which is an angle measured from the body center line, changing from 0° (i.e., normal through the stagnation region) to 20°. We use a value of $\theta' = 40°$ in our considerations. We are concerned only with the stagnation region since we wish to obtain a comparative figure for Σ_{total} ($V_\infty = 60.10^3$ fps), as obtained from Cauchon's data. We may then define an effective area which accounts for the nonuniform dissipation. From Stainback's approach, a factor of 0.25A seems appropriate. Since A is about 2 ft^2 we obtain a heat dissipation per unit area in the stagnation region of

$$\Sigma_{total} = 87 \times 10^4 \text{ joules/cm}^2.$$

This seems reasonably consistent with the values obtained in Table 1; the difference being lost in translating the gas cap and in the energy conversion process.

In the next step we must consider the sensor-orifice geometry. As viewed from the sensor, the radiating shock front is simply a uniformly circular source of diameter d_j = 1/16 in., and is effectively a plane source radiating into a hemisphere (i.e., 2 π solid angle). The cavity depth assumed is 2-1/2 in., and we further assume that the back cavity wall is formed by the spectroscopy system. The solid angle ω subtended by a unit area of the sensing system is 0.025 steradians. Thus the energy incident on the sensing surface $\Sigma_s = \frac{\Sigma}{2\pi} \omega s$ where s is the effective source area. For parameters used here, the constant term $\frac{\omega s}{2\pi} = 8 \times 10^{-5} \text{cm}^2$. Thus the actual heat reaching the sensing surface under the various conditions can then be obtained by applying this factor to the values, as tabulated in Table 1.

We have also calculated the radiation entering through a 3/16-in. diameter orifice for the entire heat pulse period. These results, showing the radiant energy integrated over the whole spectral region, are given in Figure 12.

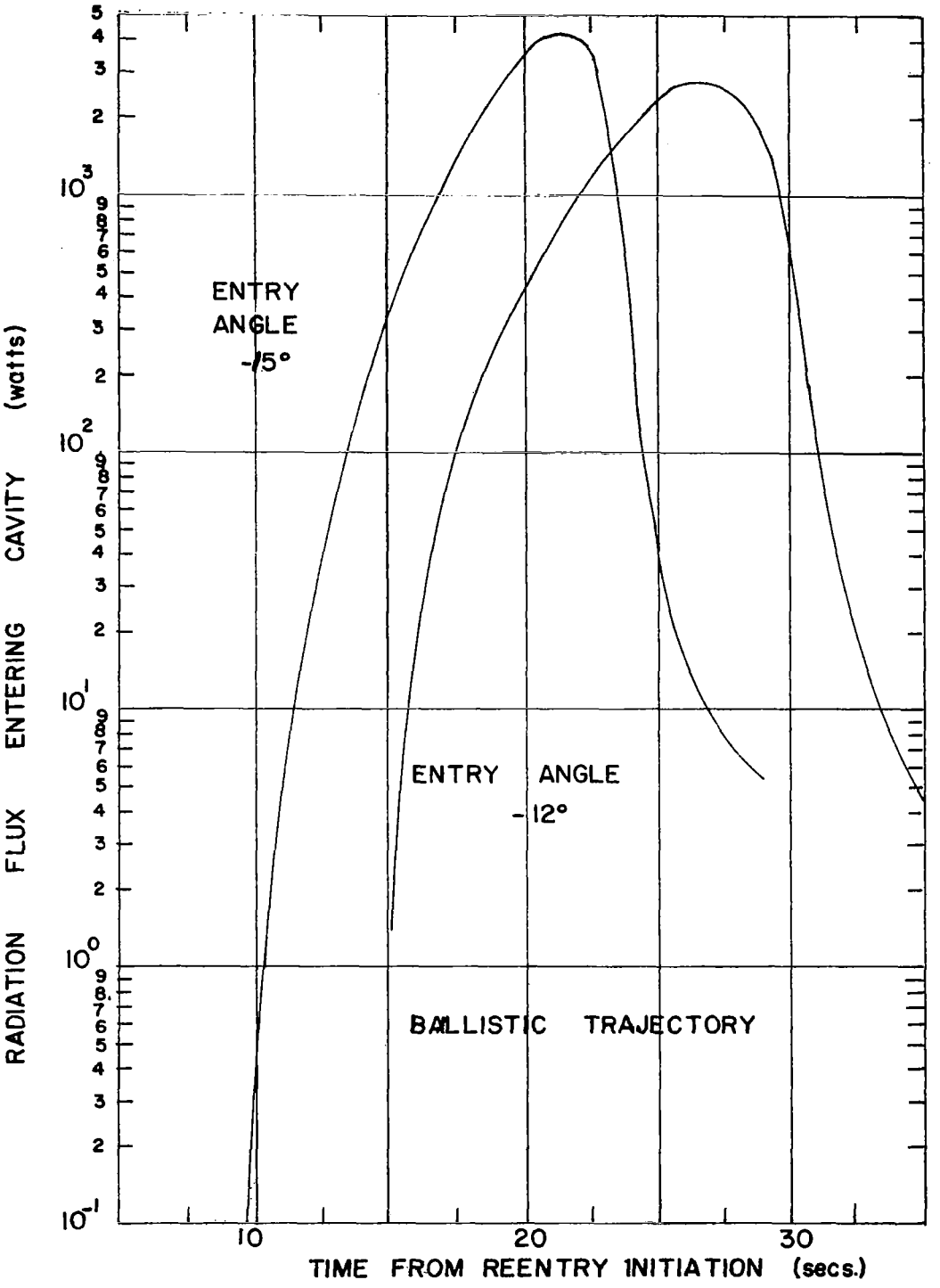

FIGURE 12. RADIATION FLUX INTO CAVITY (CAUCHON, REF. 1) V_E = 50,000 ft/sec. CAVITY APERTURE 0.192 cm^2.

Figure 13 shows the total amount of energy absorbed up to a given time; it was assumed that the absorptivity of the cavity was unity. Figures 12 and 13 were generated neglecting convection heating. Cauchon's work shows that stagnation-point heating by convection can only be neglected for approximately 7 sec around the peak. However, the situation is altered in the present circumstances by the helium issuing from the cavity, which will, to some measure, reduce the heat transfer. In view of the remarks made earlier about the reasons for using Cauchon's results, it is justifiable to neglect the convection heating, making the situation a little less severe (the effect is only about a factor of two at most, which is well within the uncertainties of the problem).

Figure 13 show the total amount of heat radiated into the cavity. It also shows the total amount of heat that would be radiated away by the cavity, held at a fixed temperature. The datum for these curves is 10 seconds after reentry initiation. It is clear that reradiation through the cavity aperture is of little significance and may be neglected. Thus, other means are necessary for accomodating the high heat input. (Note: no account has yet been taken of radiation reflected by the cavity, the absorptivity was taken as unity). Since we now have available the heat inputs to the cavity, we have turned out attention to specific material types. In Table 2 we have listed the properties of several possible materials and also have identified the type of sensor-spectroscopy system in which the material would be used. This table is probably not yet comprehensive; other materials are of possible interest and other properties of those materials shown must be considered. Of particular importance is the effective absorptance and reflectance over the spectral range ~2μ to 500Å of each material. With data of this type and the heat input information, it will be possible to define system operating temperatures as the various types are considered.

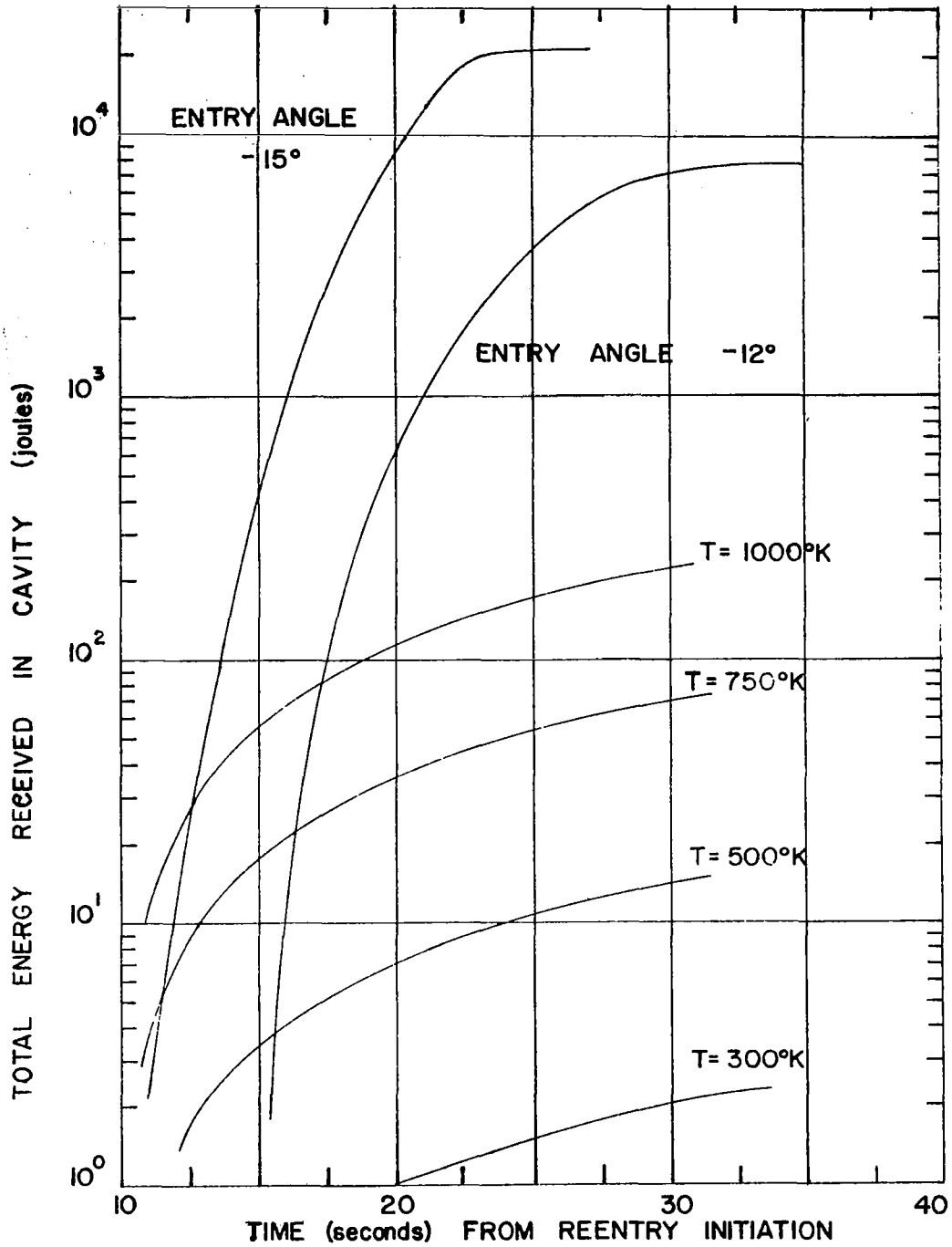

FIGURE 13. TOTAL RADIATION ENERGY ENTERING CAVITY. LOWER CURVES SHOW TOTAL HEAT LOSS RADIATED BY CAVITY HELD CONSTANT AT THE TEMPERATURE INDICATED (TIMES ARE FROM 10 SEC. ONWARD EXCEPT FOR THE -12° CASE). V_E = 50,000 ft/sec - BALLISTIC TRAJECTORY.

TABLE 2. PROPERTIES OF MATERIALS

Material	Critical Temperature (°C)	Thermal Conductivity 10^{-4}cal/(cmsec°C)	Linear Coefficient of Expansion 10^{-6}/°C	Specific Heat Cal 15°/g/°C *cal/gm	Transmission Range μ	Possible Component Type See Code
MgF_2	1255		15		0.11 - 75	A, H,
LiF	870	270	37	0.37	0.12 - 9μ	A, H, F
Al	659	5140	18	0.004*		I
$CaCO_3$	894	132	25	0.20	0.3 - 55	B
Cu	1083	10970	15	0.092*		I
CdS	900	380	4.2		0.52 - 16	C, D, E, G
Pt	1773	1664	8.8	0.0012		I
Ge	936	1400	6	0.074	1.8 - 23	C, E
Cr	1890		7	0.06*		I
CdTe	1040		4.5		0.9 - 15	C, D, E, G
GaAs	1238		5.7		1 - 11	C, E
BaF_2	1280	280			0.15 - 15	A, H
CaF_2	1360	232	24	0.20	0.13 - 12	A, H
Si	1420	3090	4.2	0.168	1.2 - 15	C, E
FusedSiO_2	1710	28.2	0.5	0.22	0.2 - 4.5	
TiO_2	1825	300	9.2	0.17	0.43 - 6.2	B, C
Al_2O_3	2030	600	6.7	0.18	0.17 - 6.5	A, B, C
MgO	2800	600	13.8	0.21	0.25 - 8.5	C, B

CODE FOR TABLE 2

A: Transmission - Reflection Filter

B: Phosphor for wavelength shifting

C: Strip photoconductor

D: Strip photovoltaic

E: Coincidence spectrometry detector

F: Photoelectric cathode material

G: Grating material

H: Solid window for oblique view system

I: Grating substrate

Spectral Distribution

The spectral distribution of radiant energy incident on the stagnation point, computed by Allen[17], is not sufficiently detailed for the present requirements, since all radiation below 2000Å (the wavelength region of interest) has been summed. Sullivan[4] has provided preliminary data on spectral breakdown in this region, calculated using the computational methods of Hoshizaki and Wilson[19]. In this case, the vehicle followed a lifting trajectory with a peak deceleration of 7.4 g for the following conditions:

V_∞ = 48,000 ft/sec (velocity of vehicle)

Altitude = 208,000 ft

δ_{stag} = 0.51 ft

T_{stag} = 14,000°K

P_{stag} = 0.48 atm.

The trajectory followed was of the kind shown in Figure 6 on which has been placed the ballistic trajectory of Figure 4. Sullivan's calculated heat fluxes are shown in Figures 14 and 15: the former is for assumed adiabatic conditions and the latter takes into account radiation absorption. Figure 15 was obtained from calculations based on a temperature profile of the kind shown in Figure 16, where allowance is made for radiation cooling and also for the boundary layer.

In Figure 17 the radiant energy flux distribution is given, for the nonadiabatic case (taken from Figure 15) for a 50 Å bandpass. No line-widths are indicated in Figure 14 and 15; hence, these were taken as equal and obtained by dividing the heat flux due to the lines by the sum of the line intensities indicated in the figures. We now have available the radiation energy per unit resolution element enabling us to compute the performance of postulated spectroscopy systems.

This establishes the most pertinent factors affecting spectroscopic measurements of the shock wave created ahead of a capsule experiencing hypervelocity reentry conditions. Since no specific mission has yet been defined, a generalized set of conditions have been applied. The data

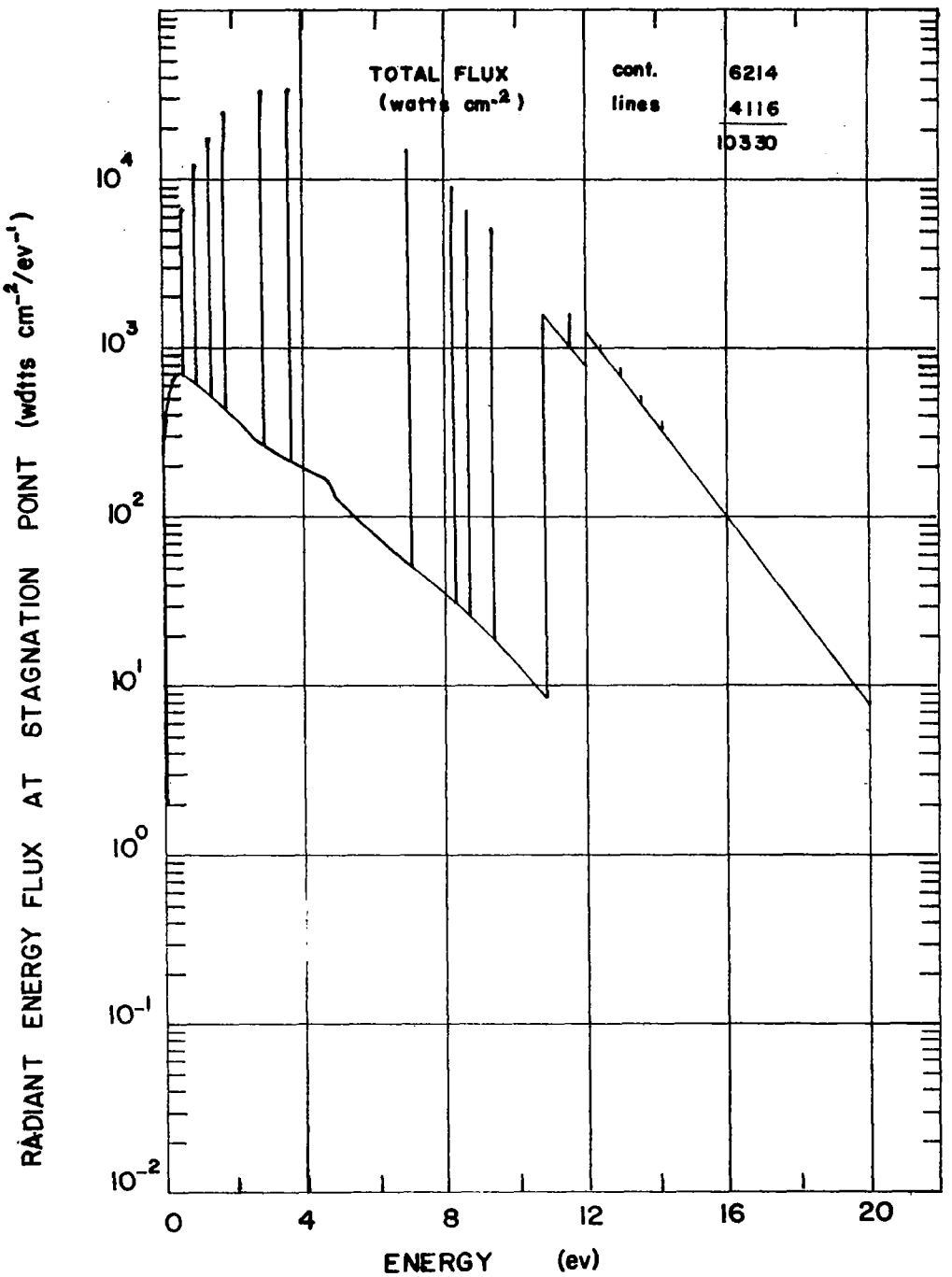

FIGURE 14. RADIATIVE HEAT FLUX TO STAGNATION POINT, ADIABATIC CASE. (PRELIMINARY RESULTS FROM REF. 4)

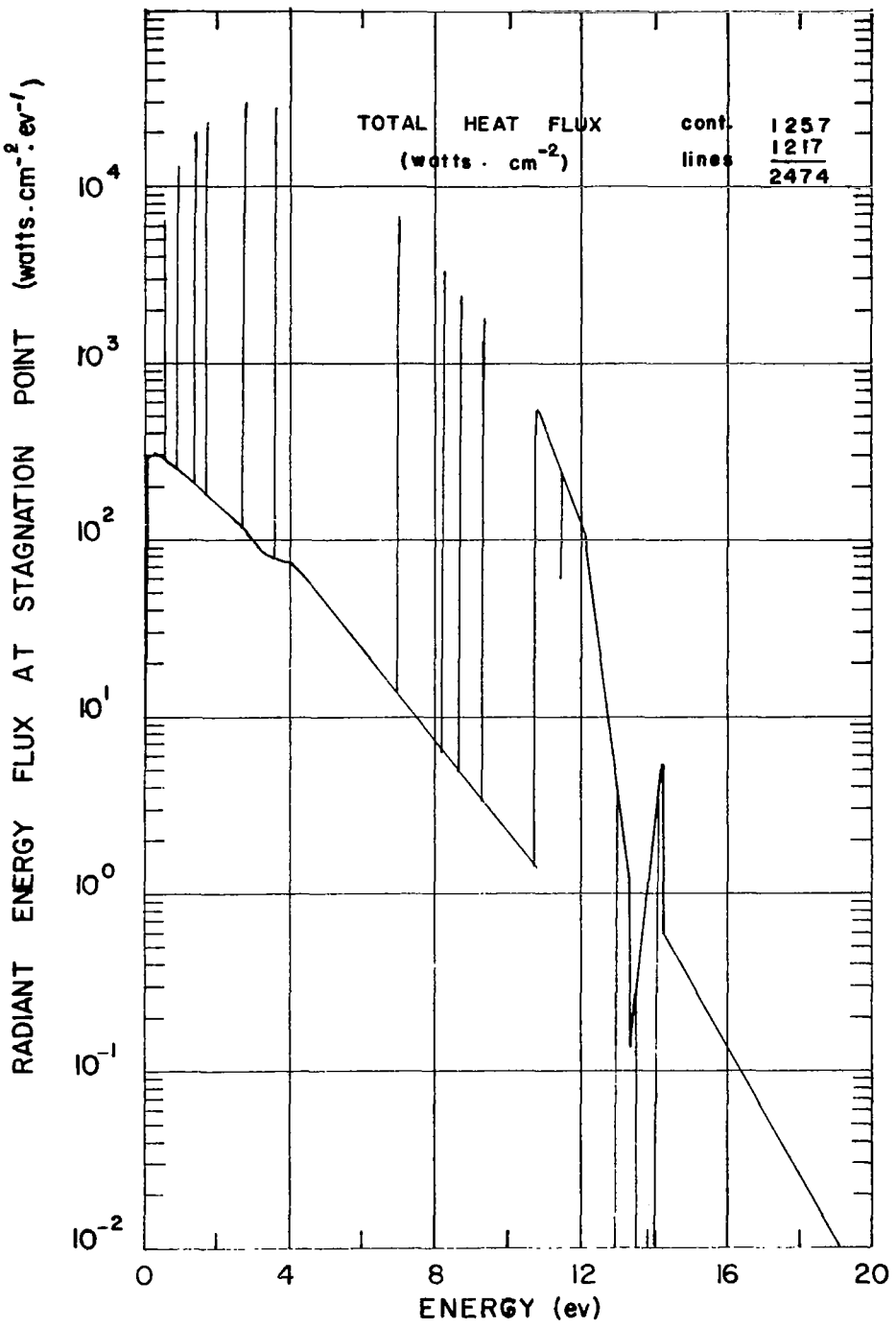

FIGURE 15. RADIATIVE HEAT FLUX TO STAGNATION POINT, NONADIABATIC CASE. (PRELIMINARY RESULTS FROM REF. 4)

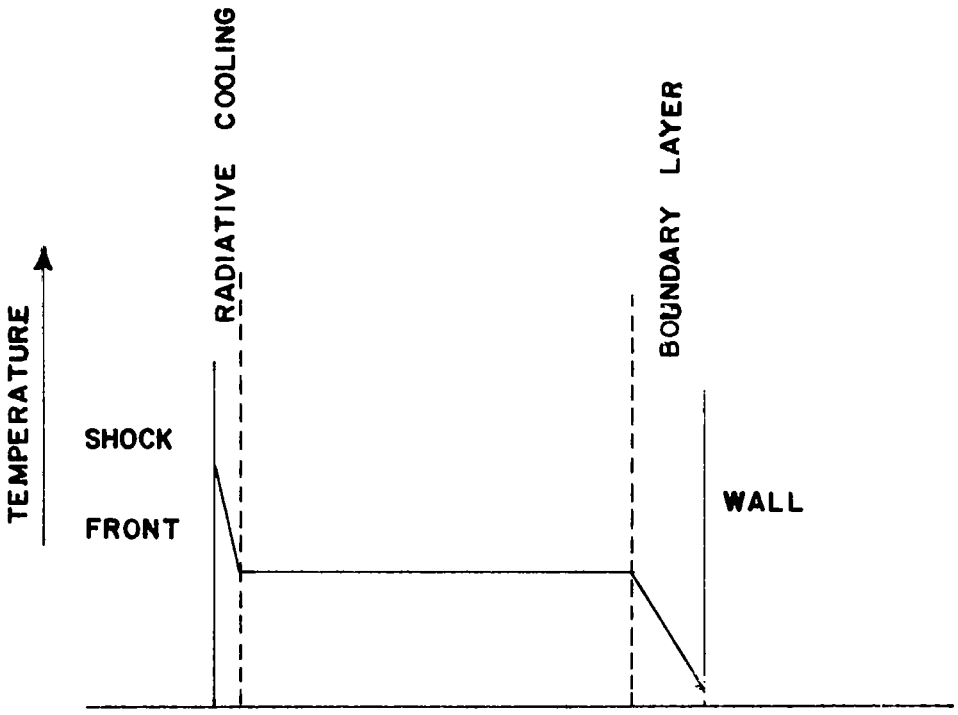

FIGURE 16. ASSUMED TEMPERATURE PROFILE FOR NONADIABATIC CALCULATIONS

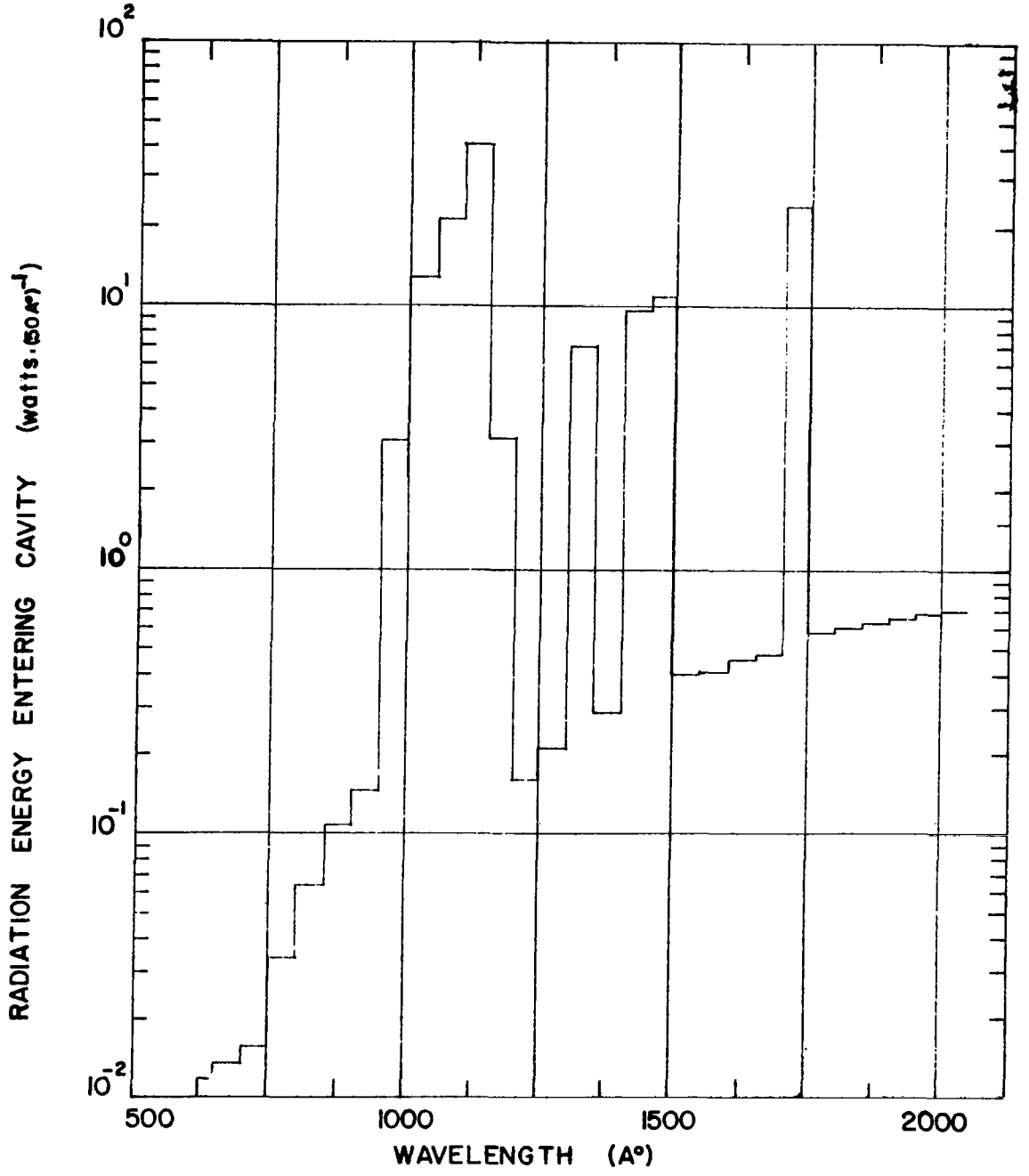

FIGURE 17. SPECTRAL DISTRIBUTION OF RADIANT ENERGY ENTERING CAVITY DURING PEAK HEATING PERIOD. LIFTING TRAJECTORY NONADIABATIC CASE. CAVITY APERTURE 0.192 cm^2.

includes capsule conditions and features of the shock front radiation such as total heat input and spectral distribution of the radiation.

III. EVALUATION OF DETECTOR SYSTEMS

In this part simple flux and energy discrimination detectors are evaluated to determine their potential use in the reentry vehicle described in Part II. The simple flux systems are ion chambers, proportional counters, Geiger-Mueller tubes, photoelectric tubes, wavelength shifters, photoconductive cells, photovoltaic cells, and reverse biased diodes. Flux detection with energy discrimination systems are scanned miniature diode arrays, a wavelength shifter-reverse biased diode system, and a photoelectric cathode with retardation grid analyzer. All these devices are considered for use in the 500-2000Å region. One problem in evaluating many detectors was the lack of investigations on operation in the vacuum UV region. By grouping ion chambers, proportional counters, and Geiger-Mueller tubes into the category of gas ionization detectors, their analysis is simplified.

A. Simple Flux Systems

1. Gas Ionization Detectors

Three types of detectors fall into this category, namely the ionization chamber, proportional counter and Geiger-Mueller counter. These three devices have various characteristics, but are similar in construction: different values of the applied potential give rise to their respective modes of action. The ionization cell conducts a current when a photon, entering the cell, causes ionization. If the photon is sufficiently energetic, the liberated electron has sufficient energy to ionize other gas molecules so that a current pulse arrives at the anode. The anode is often a wire or pin surrounded by a cylindrical cathode, but other configurations are also possible. As the potential between the electrodes is increased, a threshold value is reached above which an electron can obtain sufficient energy in one mean free path to ionize again. This is the breakdown condition and marks the start of the proportional region. In the proportional region secondary electrons are produced and amplification follows. The amplification factor is independent of the magnitude of the current pulse for gains up to about 10^7. Above a certain

voltage the amplification depends inversely in some way on the pulse size, this is the region of limited proportionality. As the voltage is further raised the Geiger region is reached. Here the amplitude of the pulse at the anode is independent of the ionizing event. Eventually, increasing the voltage causes a continuous discharge. Figure 18 shows the various discharge regions.

In practice the gas-filled devices operate partly from photoelectric emission from the cathode and partly from photoionization. The source of the electrons dictates the quantum efficiency of the primary process in all cases, but is otherwise unimportant with the Geiger-Mueller counter: in the other devices it also dictates the magnitude of the response and general utility of the detector concerned. Thus, the ionization counter will respond to photons having energies less than the gas ionization energy, due to photoelectric emission from the cathode.

Ionization Chambers

These devices are generally valuable for the selection of broad wavelength regions without the use of any dispersing element. This is accomplished by judicious selection of window and gas-fill combination. They are also useful as detectors to be used in conjunction with monochromators. These two functions, neither of which correspond to the present need, seem to be the extent of their usefulness as detectors. However, some properties of these devices are given. Typical gas fill pressures are

NO	-	20	torr	
CS_2	-	15	torr	
Xe	-	775	torr	soft x-ray
Ar	-	760	torr	soft x-ray

From these pressures it is clear that it is impossible to use them without a window; if some of the gas fill escaped it would absorb radiation in the spectrograph.

Some window materials are given in Table 3 and gas fills in Table 4.

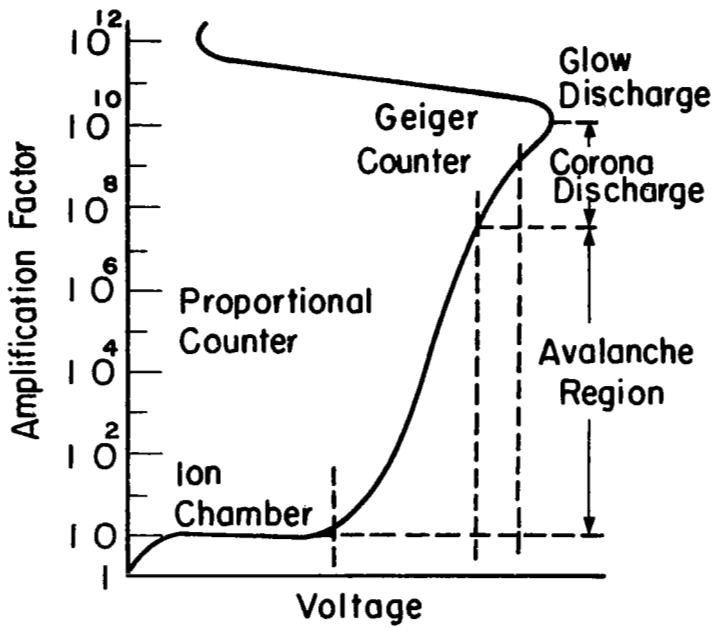

FIGURE 18. GAS AMPLIFICATION VERSUS VOLTAGE IN A COAXIAL-CYLINDER IONIZATION TUBE

TABLE 3. WINDOW MATERIALS FOR UV RADIATION

Crystal Window	Cutoff Wavelength
Lithium Fluoride	1050 Å
Calcium Fluoride	1225
Strontium Fluoride	1280
Barium Fluoride	1350
Sapphire	1425
Quartz-Ultra Pure	1450

TABLE 4. GAS FILLS FOR IONIZATION DETECTORS

Material	Ionization Potential	Cutoff Wavelength
Carbon Disulfide	10.08 eV	1230 Å
Methyl Chloride	11.29	1098
Methyl Bromide	10.52	1179
Methyl Iodide	9.54	1299
Ethyl Chloride	10.98	1129
Ethyl Bromide	10.30	1204
Ethyl Iodide	9.34	1327
Methyl Formate	10.82	1146
Ethyl Formate	10.61	1169
Benzene	9.25	1340
Benzenethiol	8.32	1490
Mesitylene	8.42	1473
Nitric Oxide	9.25	1349
p-Xylene $\sim$	8.37	1475
1, 1, Dimethylhydrazine $\sim$	7.76	1590

The spectral responses of several ion chambers are shown in Figure 19. The response curve for NO has considerable structure under high resolution. Shelf life of these detectors depends on the stability of the gas fill compound, it can be many months if care is exercised during fabrication.

Ionization chambers that have been made hitherto were not intended to be arrayed in the image plane of a spectrograph, so that they are relatively large. There seems to be no reason why such chambers can't be very small, since they operate on a single electron basis, i.e., no multiplication. However, the quantum efficiency of the ionization chamber will change as it gets smaller. Above about 1350 Å, for the nitric oxide gas fill, the electrons collected are only those due to photoemission from the cathode (the device is a gasfilled photodiode). At shorter wavelengths the gas ionizes. When ionization of the gas occurs, decreasing the size of the chamber reduces the number of electron-ion pairs formed. The decrease in size would result in a smaller light gathering power.

The time resolution of an ionization chamber should be very similar to figures given for the Geiger-Mueller counter, i.e., about 10^{-6} sec. This follows from the electron mobility, which is proportional to X/P, where X is the electric field and P the pressure. Thus by comparing these two detectors

$$\frac{(X/P)_{I.c.}}{(X/P)_{G.c.}} \approx \frac{50}{20} \quad \frac{700}{1000} = 1.75$$

Now taking into account the fact that the ionization chamber operates on a single electron basis, no trailing edge to the pulse, suggests that, for similar dimensions, the two devices have very similar response times, about 10^{-6} second, or better.

A NASA chamber is described by Dunkelman[22], Stober[23], and Scolnik and Hennes[24]. It consists of a ceramic shell, gold plated on the inside, fitted with a highly polished central wire electrode. A suitable transmitting window is required, hence this type of detector probably cannot be used below 1050 Å in the relatively high pressure helium environment envisaged here.

A similar photoionization detector has been made at NRL[25]. In this case the outer sleeve was made of Kovar and there were some minor differences in the construction.

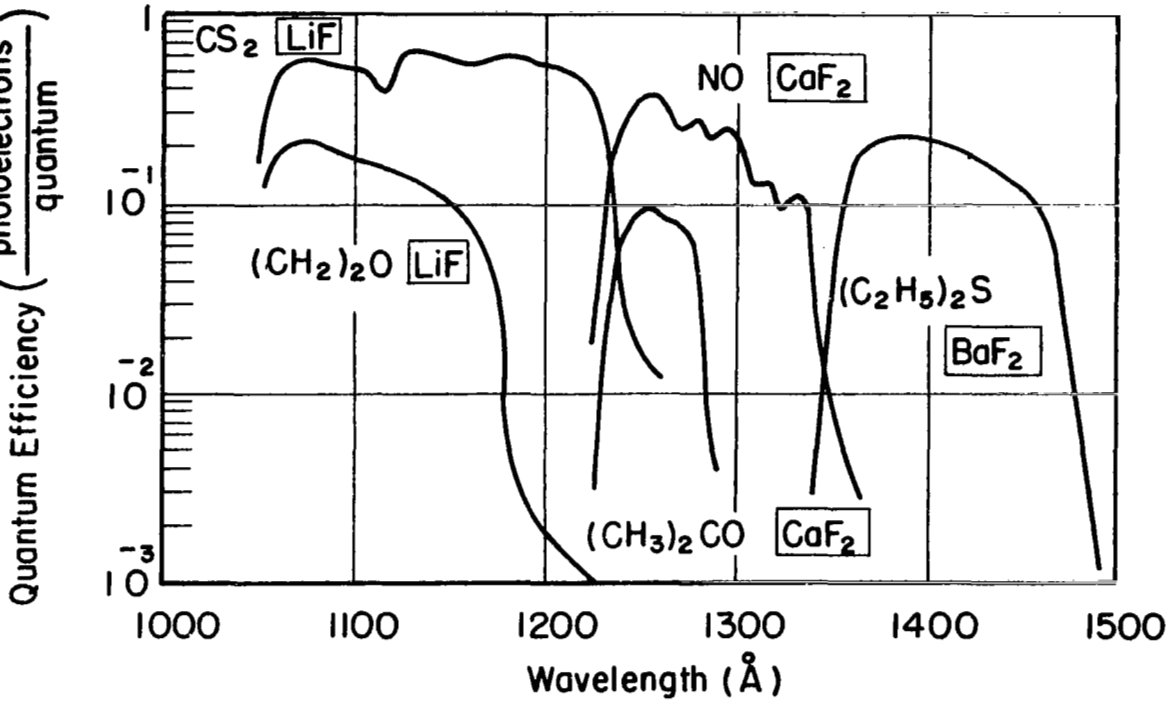

FIGURE 19. SPECTRAL RESPONSES OF SEVERAL ION CHAMBERS FOR THE REGION FROM 1000Å to 1500Å. BOXED SYMBOLS REFER TO THE PHOTOTUBE WINDOW MATERIALS.

The NASA chamber is normally operated with the wall at ground potential and the electrode at -45 to -90 volts depending on gas fill. When it is necessary to suppress photoelectric emission from the walls completely, the shell electrode is made positive. These cells are also operated in the proportional mode, gains of 10^3 have been obtained with 600-800 volts, the shell carries the negative high voltage in this case.

Proportional Counters

The ionization chamber operated at high voltages is essentially in the proportional region, where the current to the electrodes is proportional to the number of ion pairs initially created. Proportional counters are normally filled with a mixture of a monatomic and a polyatomic gas. This is because the positive ions of the monatomic (or diatomic) molecules cause secondary emission from the cathode, whereas positive ions of polyatomic molecules do not. Thus, by using such mixtures the proportional property is retained[26].

Since these devices are operated in the multiplicative voltage regime, the size of the pulse depends on the energy of the incident electron. This energy discrimination property may be utilized when pulses are recorded from single photons. The mechanism is similar in some respects to the retarding potential analyzer (RPA) but there is a difference. With the RPA a monochromatic photon flux generates electrons with a particular energy distribution and this is monitored to obtain the wavelength of the incident photon, and the intensity of the flux. The same is done in the case of the proportional counter by measuring the pulse-height distribution, which is related to the energy of the liberated electron. The measurement is not as precise as for the RPA, however, since the primary electron may be liberated at the cathode or somewhere in the gas and this electron is then accelerated to produce more electrons. These factors should result in a less precise measurement of the energy of the initial photon than found with the RPA. Also each photon must enter the chamber and be amplified individually.

Thus, one concludes that the proportional mode is of no interest in the present applications except in so far as it corresponds to the ordinary ionization chamber operated at gains exceeding unity.

Geiger-Mueller Counters

These devices have been described in considerable detail in the literature[27]. The same type of cell is used

as for the proportional counter, a cylindrical cavity with a wire anode down the center; radiation enters a window at the side. If the voltage applied to the electrodes is increased beyond that for the proportional region, or region of limited proportionality, it is found that the counter enters a voltage region in which the size of the pulse arriving on the wire is independent of the number of ions initially formed. The size of this pulse is still dependent on the applied voltage. Thus this behavior may be characterized by the gain being inversely proportional to the number of ion pairs formed initially, so that the current pulse is the same for all kinds of ionizing events; thus, in the present application it is merely necessary that the photon produces an electron. As the applied voltage is increased still further, the counter goes into continuous discharge.

For the Geiger region, unlike the proportional region, where each primary electron generates a single avalanche, each avalanche triggers others so that the discharge spreads rapidly throughout the whole counter. In practice the mechanism of a good counter is quite complex and has to take into account such factors as suppression of secondary emission at the cathodes and suppression of spurious pulses (ionization transfer from positive ions of the rare gas to polyatomic vapor molecules).

The output pulse is characteristically fast rising with a slow decay. The collection of electrons from the discharge is very fast compared with the collection of positive ions. Thus a positive ion sheath moves out from the wire anode. The time for this sheath to reach the critical distance from the wire corresponding to threshold is the "dead time". The counter is insensitive to any ionizing event during this time. The additional time required for the ion sheath to reach the cathode is called the "recovery time". During the recovery time the size of pulse obtained is determined by the time elapsed since the previous discharge. Thus counter design is directed towards minimizing the dead and recovery times, in order to increase the maximum counting rate. The arrival of the positive ion sheath at the cathode results in the full restoration of the electric field. There is now the possibility of secondary emission triggering the counter again. This is prevented by a mixture of polyatomic gas.

Geiger counter tubes can be made very small, see Figure 20. The use of these counters for ultraviolet detection has been described by Chubb and Friedman[28] for the wavelength

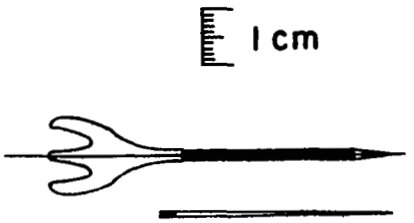

FIGURE 20. MINIATURE GEIGER COUNTER

range 1050 to 2500 Å. The spectral sensitivity of a broad band counter is shown in Figure 21, and much narrower band passes are quite feasible by appropriate selection of window and gas fill. At the long wavelengths the counter is triggered by photoelectric emission from the cathode, rather than by ionization in the gas ($\lambda > 1500$Å in Figure 21).

Dead times and recovery times are about equal to one another and can be reduced by making small bore counters. Friedman quotes times of about 5μ sec for counters of diameters 0.25 in. Thus his maximum achievable counting rate would appear to be 10^5 - 10^6 counts/sec. However, it is suggested that counting rates in excess of 10^6 counts/sec are possible. Since the counter is triggered by the production of photoelectrons at the cathode, for much of the wavelength range of interest, there are two additional factors to be taken into account. The first is the "gas counting efficiency", this is the ratio of the number of Geiger counts to the number of photoelectrons liberated at the cathode. The second is the "relative cathode efficiency" which is a measure of the effect of the organic quenching agent on the photosensitivity of the cathode surface (it tends to increase the work function). Some values are given in Table 5.

TABLE 5. RELATIVE CATHODE AND GAS COUNTING EFFICIENCY FOR ION COUNTERS

Filling	Light Filter	Relative Cathode Efficiency	Gas Counting Efficiency
7 mm ethyl formate 630 mm He	Fused quartz	1	4×10^{-1}
20 mm NO 615 mm Ne	Fused quartz	2.6×10^{-2}	4.0×10^{-2}
50 mm NO 585 mm Ne	Fused quartz	1.5×10^{-2}	3.0×10^{-4}
21 mm Cl_2 530 mm Ne	Fused quartz	4×10^{-3}	1.4×10^{-7}
21 mm Cl_2 530 mm Ne	LiF		4.7×10^{-4}

NOTE: These measurements were made with a hydrogen lamp through filters of fused quartz and lithium fluoride.

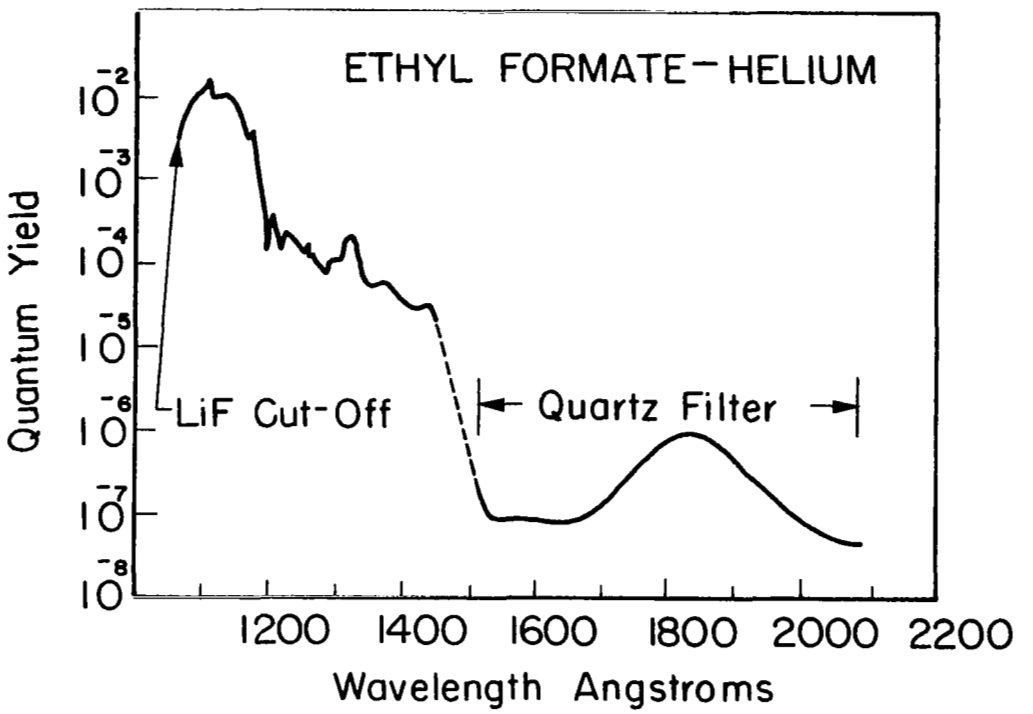

FIGURE 21. SPECTRAL SENSITIVITY OF AN ETHYL FORMATE QUENCHED COUNTER. THE RESPONSE BETWEEN 1450Å and 1520Å WAS MASKED BY AN EXCESSIVE BACKGROUND OF SCATTERED SHORTER WAVELENGTH LIGHT. A QUARTZ FILTER WAS USED TO REMOVE THIS BACKGROUND FOR MEASUREMENTS BETWEEN 1520Å AND 2100Å. THE QUANTUM YIELDS INDICATED ARE THOSE OF THE PHOTON COUNTER AND NOT OF THE COMBINATION OF PHOTON COUNTER PLUS QUARTZ FILTER.

Application to Reentry Spectrophotometry

The qualifications of these devices can be summarized briefly:

i) Diameters down to 0.2 in. or possibly less.

ii) Wavelength range down to 1050 Å. Ionization chambers below 1500 Å, Geiger-Mueller counters cover the range up to 2000 Å. The ionization chamber will also work at longer wavelengths if the cathode is illuminated, it is then, in effect, a gas filled photodiode.

iii) Amplification factor less than 10^3 for ionization chambers. Output from Geiger-Mueller counters may be around a volt.

iv) Quantum efficiences for ionization chambers (wavelengths less than 1450 Å) are greater or equal to 10^{-1}. With Geiger-Mueller counters the product of gas counting efficiency and relative cathode efficiency can be anywhere from 1 to 10^{-10}.

The window limitation seems to preclude the use of existing devices over the whole spectral range of interest (500-2000 Å), although they can be used in the region above 1050 Å. A monochromator system can now be assumed for the purpose of evaluating the performance of the various detectors, when exposed to the estimated spectral energy distribution of a reentry vehicle (described in Part II). This is not a finalized system but only used for the purpose of comparing the detectors. It has the following characteristics:

i) concave grating used in normal incidence.

ii) viewing is in the first order with the blaze at 600 Å.

iii) spectral band pass covered by each detector is 50 Å.

iv) grating surface is evaporated platinum.

In addition it is necessary to make assumptions about the dimensions and dispersion of the system. These are

v) entrance slit is 20 cm from aperture in heat shield

vi) spectrometer has a focal length of 20 cm, the grating ruled area is 5 x 2 cm and has 1200 lines/mm. Hence the instrument has a reciprocal dispersion of 42 Å/mm.

vii) entrance slit area is 0.5 cm x 100μ.

With this assumed instrument it is possible to obtain an indication of the performance requirements of the various detectors discussed earlier.

Figure 22 gives the reflectivity of platinum and an estimate of the grating effect (Figure 23) yields the fraction of radiation scattered into first order, Figure 24 (the curve in Figure 24 is the product of that in Figure 23 with the Pt reflectivity). The radiation entering the instrument cavity through the heat shield port (3/16" dia.) was given in Part II. The radiation flux in the exit plane of the spectrometer is presented in Table 6.

Comparison between Table 6 and the overall efficiencies show that Geiger-Mueller counters could be used. Thus ionization chambers and counters could also be used for detection in the reentry application. Below 1050 Å it is necessary to operate without a window and in a helium environment. It is possible that this can be achieved, using the photoelectric effect and a tungsten photocathode.

2. Photoelectric Devices

Currently available photocathodes are sensitive from the near infrared down into the XUV region. Only wavelengths below 2000 Å are of interest but a large amount of radiation is emitted by the gas cap at longer wavelengths. A dispersing system is to be used in the experiment, but these are never perfect and, in order to reduce the detection of scattered light of longer wavelengths, it is desirable to use a detecting system which is not sensitive to the near ultraviolet and visible regions of the spectrum.

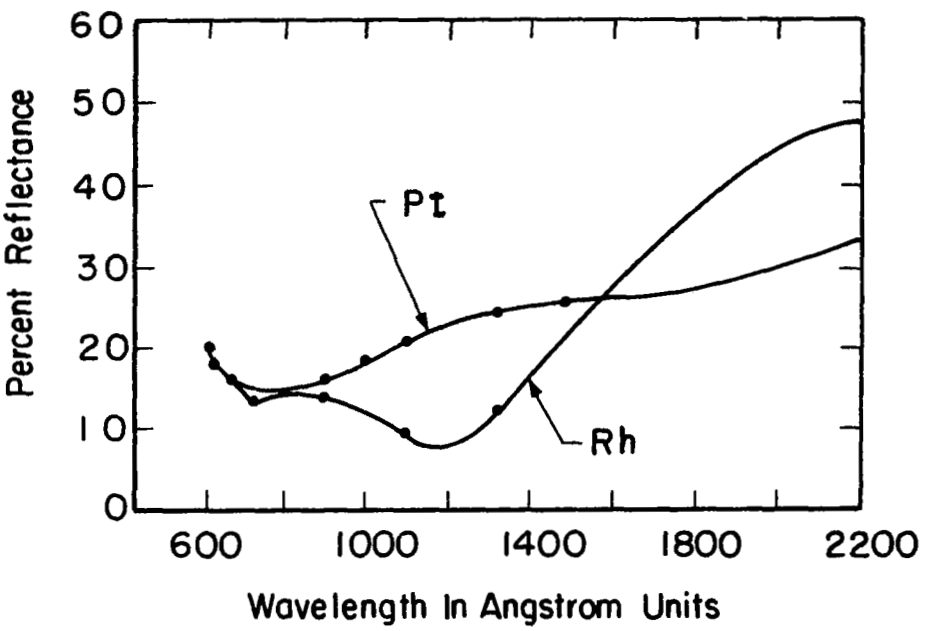

FIGURE 22. THE REFLECTANCE OF EVAPORATED PLATINUM AND RHODIUM IN THE EXTREME ULTRAVIOLET

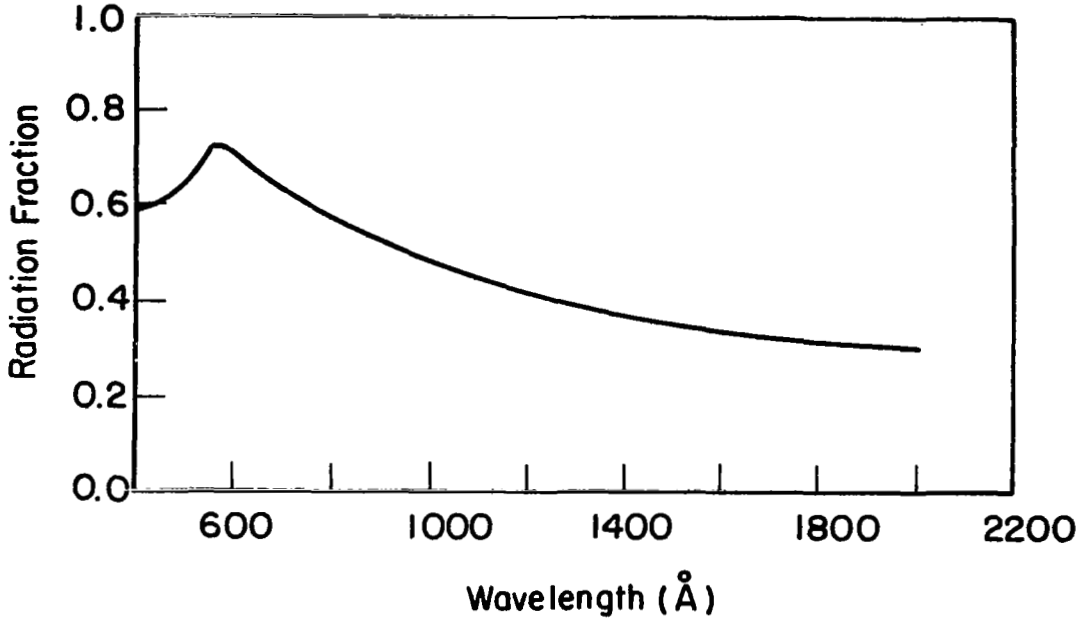

FIGURE 23. FRACTION OF RADIATION REFLECTED INTO THE FIRST ORDER - GRATING BLAZED AT 600Å - ASSUMING A REFLECTIVITY OF UNITY.

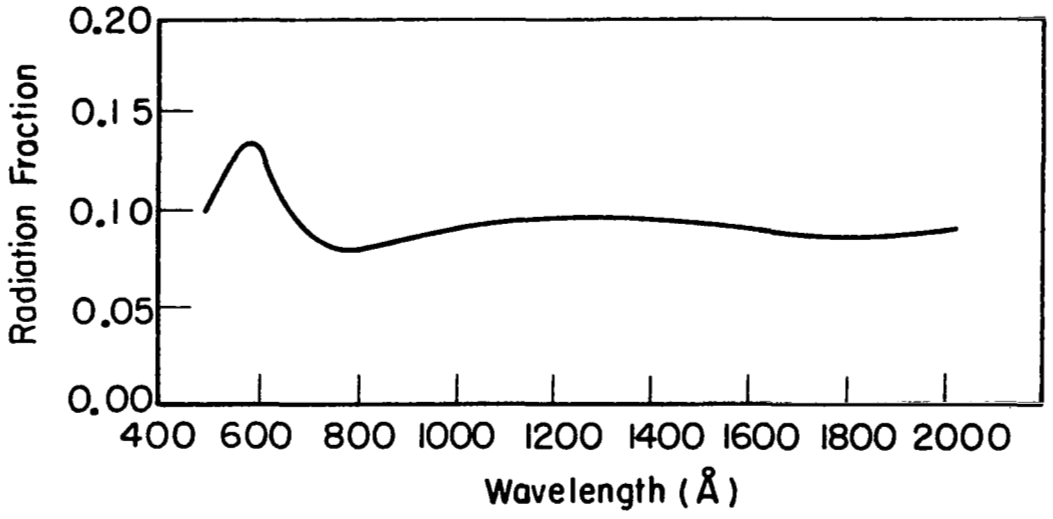

FIGURE 24. FRACTION OF RADIATION REFLECTED INTO FIRST ORDER FOR A GRATING BLAZED FOR 600Å AND HAVING AN EVAPORATED PLATINUM SURFACE.

TABLE 6. RADIATION FLUX IN EXIT PLANE OF SPECTROGRAPH

Wavelength Å	Flux in 1st Order (quanta. sec^{-1})	Wavelength Å	Flux in 1st Order (quanta. sec^{-1})
525		1325	1.84 + 11
575		1375	7.70 + 9
625		1425	2.63 + 11
675	1.81 + 8 (a)	1475	2.83 + 11
725	1.86 + 8	1525	1.14 + 10
775	4.28 + 8	1575	1.20 + 10
825	8.60 + 8	1625	1.33 + 10
875	1.58 + 9	1675	1.42 + 10
925	2.34 + 9	1725	7.40 + 11
975	5.35 + 10	1775	1.79 + 10
1025	2.40 + 11	1825	1.89 + 10
1075	4.31 + 11	1875	2.02 + 10
1125	8.80 + 11	1925	2.46 + 10
1175	7.11 + 10	1975	2.39 + 10
1225	1.60 + 10	2025	2.61 + 10
1275	5.45 + 9	2075	

(a) The digits on the right of the (+) indicate the power of ten. e.g., 1.81 + 8 = 1.81 x 10^8

Window materials are of considerable importance. LiF transmits down to about 1050 Å, below which it is necessary to operate without a window. The vacuum UV cut-off wavelengths for some common window materials have been presented in Table 3. At very short wavelengths, in the soft x-ray region, it is again possible to use certain materials as very thin windows.

Detection in the vacuum UV is most easily achieved by means of a phosphor which fluoresces in the visible, so that ordinary photomultipliers (e.g. 1P21, 1P28) can be used to detect radiation in the "windowless" region below 1050 Å. However, a very wide range of spectral sensitivity is undesirable for the previously mentioned reasons.

These devices all rely on the surface and volume photoelectric effect over the spectral range. The occurrence of a volume photoelectric effect is fortunate. It means that the quantum efficiency of the photocathode is unaffected, within limits, by surface contamination. This, in turn, simplifies handling and assembly of the devices into an instrument package. Onset of the volume photoelectric region is marked by a large increase in the quantum efficiency. A good example is tungsten, for which the threshold lies at about 1440 Å. The threshold for other metals lie in the general region 1200-1600 Å. Since window materials are available down to 1050 Å, it is possible to use sealed detectors in the spectral range covered by the surface photoelectric effect, and to rely on the volume effect where no such windows are available[29].

In recent years, rocket spectro-photometry in the upper atmosphere has lead to the development of the "solar blind" photocathode, which is not sensitive to visible radiation. In addition there have been considerable advances in the development of windowless photomultipliers. These topics are discussed in the following sections in relation to the present needs.

Photocathodes - Quantum Efficiency

One of the most widely used photocathode materials is Cs-Sb which responds strongly in the visible, UV and vacuum UV. For purposes restricted to the vacuum UV it is not too suitable and one of the solar blind type of photocathodes is more desirable. The spectral responses of Rb-Te and Cs-Te, which are very similar, rise sharply at around 3000 Å, reaching

a peak near 2500 Å. These detectors have the advantage of a relatively flat response, but again, also respond to radiation of wavelengths longer than of interest here. If a non-flat response can be tolerated, photocathodes of Cu-I or Cs-I are better. For responses which rise sharply at 2000 Å, there appear to be appreciable differences in the reported sensitivities of these curves - see Figure 25. Photomultipliers have also been made with photocathodes of Mg, Cd and Au. No detailed search has been made for data on the quantum efficiency of these metals but the EMI literature gives responses down to 1900 Å and Weissler[30] presents the response of Cd. The magnesium photocathode has a response which rises steeply from about 3700 Å to a value at 2000 Å pf 0.4×10^{-2}. The cadmium and gold photocathodes begin to respond appreciably at around 2500 Å and are shown to have quantum efficiences of 0.6×10^{-3} and 10^{-4} respectively, also at 2000 Å. It is clear that the EMI data is limited by a quartz window since Weissler shows the cadmium curve rising continuously to 1000 Å. Although photomultipliers using these photocathodes are available there seems little point at present in trying to find out more about them. Ultraviolet detectors for space research have been reviewed in several places, as cited in the references, and these photocathodes were not mentioned; this fact, coupled with the information given above suggests that there is no need to consider them further.

The quantum efficiencies of other materials have been reviewed by Weissler and Dunkelman[31,32] and shown in Figure 26. It is seen that these offer some advantages especially tungsten, since its low sensitivity is in the region of high radiative flux but increases where the flux is falling off, at low wavelengths. Figure 27 shows the response of tungsten at shorter wavelengths.

Photomultipliers

There are several different kinds available and these are considered separately.

Conventional

Conventional photomultipliers are glass tubes with an end window. The window material is open to choice, LiF takes the response to the lowest wavelength, 1050 Å. The tubes vary in size: the smallest appears to be about 0.5 in. dia. and 2 in. long. This EMI tube has a Sb-CsO photocathode with a Corning 9741 type glass and, as such is intended for the visible and near UV. However, it is probable that the same

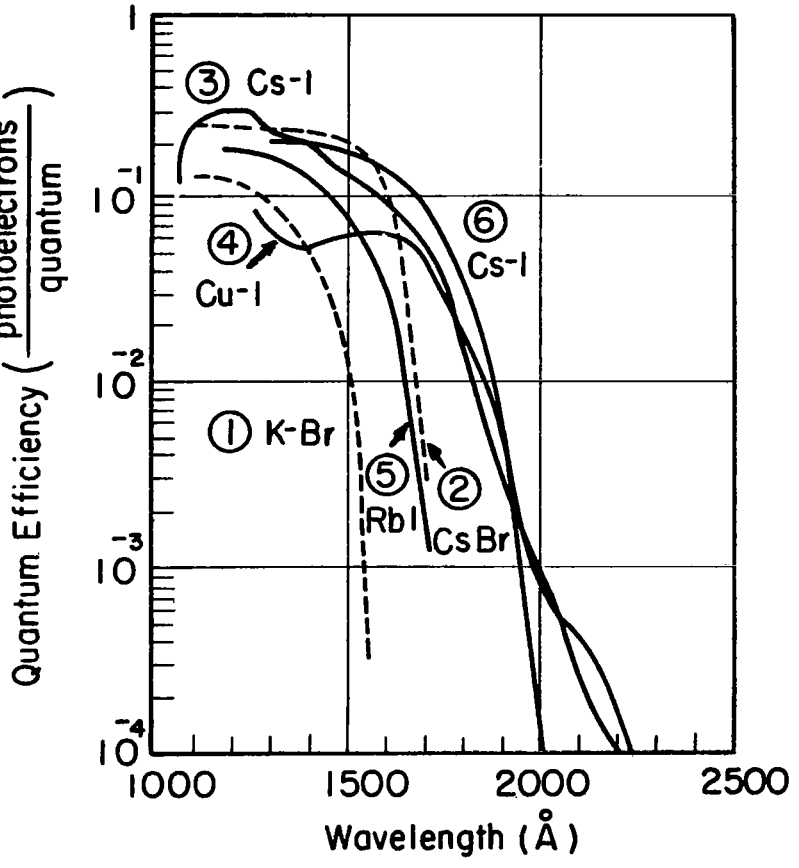

FIGURE 25. SPECTRAL RESPONSE CURVES OF SEVERAL HIGH WORK-FUNCTION PHOTOCATHODES.

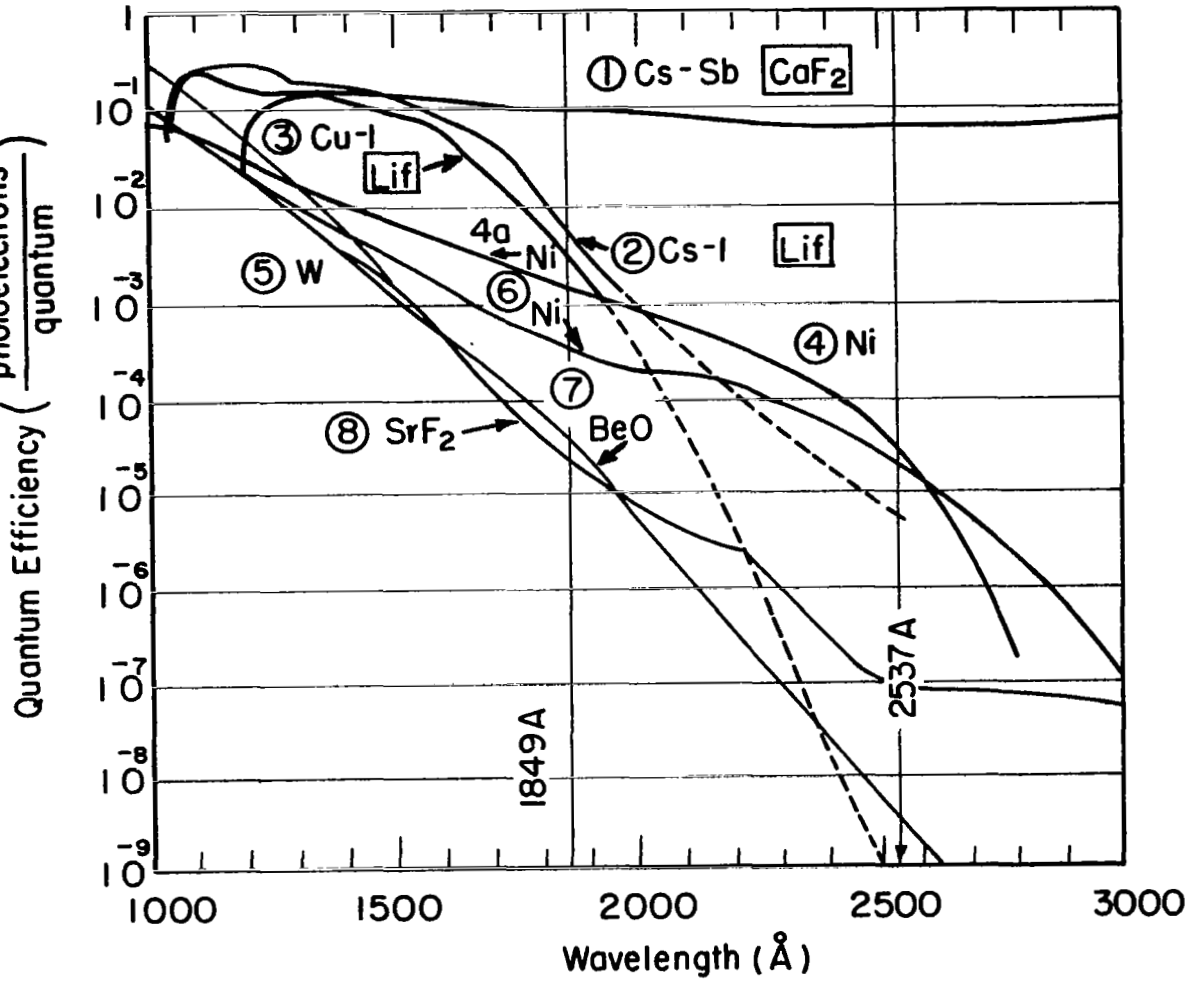

FIGURE 26. SPECTRAL RESPONSE OF VARIOUS PHOTOCATHODES.

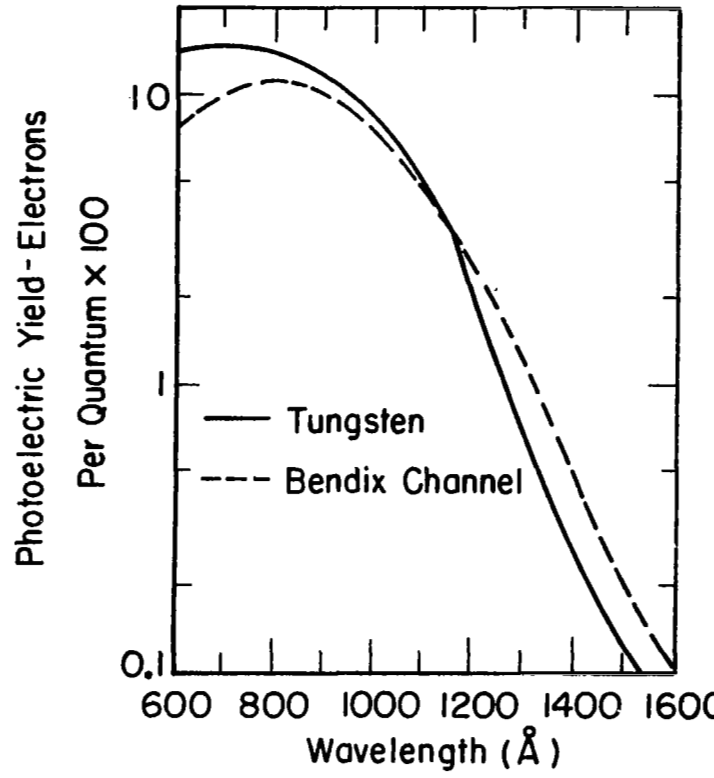

FIGURE 27. THE SPECTRAL RESPONSE FOR TUNGSTEN AND FOR A BENDIX CHANNEL MULTIPLIER. THE YIELD DATA FOR THE CHANNEL WERE ONLY RELATIVE AND WERE MATCHED TO THE TUNGSTEN CURVE AT 1000 to 1100Å.

tube could be made with more suitable photocathode and dynode materials and fitted with a crystal window should the need arise. Such tubes are usually 14-stage with a maximum gain of 10^8. The tube mentioned above has 11-stages with a probable gain of 10^5 - 10^6 (other tubes also have up to 18 stages). No comparison has been made between the products of different companies. The differences are likely to be minor and, at present, the main concern is to compare the different types of detectors; however, Dunkelman shows that there can be more than a factor ten variations in Cs-Te photocathodes with different tubes.

Conventional photomultipliers are made with various dynode geometries: focused structure, venetian-blind structure and box-and-grid structure. In the last two structures the interdynode fields are comparatively weak. The focused structure provides strong fields and reduces the spread in transit time of the electrons; the higher fields also allow larger currents to be drawn before space-charge effects arise. The stage gain is a function of the dynode geometry as well as the nature of the emitting surface and it is found that the box and grid structure is the most efficient.[33]

Windowless photomultipliers of this type are available from some manufacturers, (e.g. EMI and RCA). EMI markets tubes with dynode materials for both AgMgO and Be-CuO, for which the thresholds are in the region 2900-3000 Å with a quantum efficiency of about 20% at 700 Å. Several variations, as different dynode geometries, number of stages, and bakeable internal resistor chain are available.

Resistance Strip Multiplier

In a resistance strip multiplier the dynode chain of the conventional multiplier is replaced by a continuous strip dynode, along which there is a potential gradient. A magnetic field (supplied by permanent magnets) is used to bend secondary electrons so that they strike the strip at a point near the anode. Gains of up to 10^9 are reported by Heroux and Hinteregger[34].

This type of multiplier is marketed by Bendix Corp.[35] Models 306, 308 and 310 have a tungsten cathode. The photoelectrically measured work function of tungsten is approximately 4.5 eV corresponding to a photon wavelength of

3500 Å. The quantun efficiency rises to a peak (of 15% for the Bendix units) at 600 Å. The Bendix models 308 and 310 are very compact (2.4 x 3.7 x 6.4 and 2.4 x 2.9 x 6.4 cm respectively), end and side viewing units respectively. They have gains which are variable between 0 and 10^8. Since with this type of multiplier the gain depends on the magnetic as well as the electric field, the presence of external magnetic fields will alter the gain.

An extensive study has been reported by Timothy, Timothy and Willmore[36]. Ion feedback can occur under certain conditions resulting in overloading and reversible fatigue; the response is destroyed for periods up to 24 hours and there is also evidence of a non-reversible fatigue and increase in the strip conductivity. Temperature characteristics were studied by the same authors, for the range 0 to 50°C. Above 30°C the efficiency fell by about 4%. Also, the resistance of the semiconducting strips fell by 40% between 0° and 50°C. These results suggest that it would be worthwhile to experimentally investigate temperature effects in any devices to be used in a reentry experiment.

Channel Multipliers

There are devices which stem from an idea of Farnsworth (US Patent 1 969 399) in 1930, although it appears that the first ones were made by Goodrich and Wiley of Bendix Corp.[37] The channel multiplier consists of a glass capillary with an internal coating of a high resistance material, typically 10^8 ohms. (A similar, ceramic device was reported by Oschepkov et al. in 1960[38]). The optimum length to bore ratio is 50. Ultraviolet radiation enters at one end and the response depends on the angle of entry. The optimum angle varies with the capillary bore and Hunter[39] found that, relative to the tube axis, this was usually 15-20° but could be as large as 35° for some configurations.

In his investigations Hunter employed a vacuum of 10^{-6} torr in order to avoid photoionization effects. The quantum efficiency of the resistance layer was found to be very similar to that of tungsten, Figure 27, but it was composed of some other material. It was found that the sensitivity initially increased by nearly a factor of two and then became steady, with further use. Fatigue was noticed, when overloaded, but recovery was nearly complete after a rest period. A current value of 10^{-9} ampere appeared to be the safe upper limit. Some subsequent channels did not show the same increase in sensitivity, for unknown reasons.

Adams and Manley have also investigated the properties of channel multipliers, at Mullard Research Laboratories [40,41]. Measurements made over the wavelength range 300 to 1050 Å on the Mullard Type B410AV showed quantum efficiencies which were greater than those for the Bendix Resistance Strip Multiplier, by a factor four in some regions. Saturation effects were observed when the output current was around half the standing current in the semiconducting resistance layer. They noticed that the gain was pressure dependent: at 10^{-5} torr, a change in pressure by a factor two produced a similar change in the gain. It is not clear whether this was due to photoionization. Tests under ultra-high vacuum have shown that the gain of the multiplier decreases with time. That is to say, with a constant counting rate the mean output current falls. Decreases of 10-100 have been found over a period of 150 days. These tests were performed on relatively large Mullard devices, not the tiny Bendix multipliers. Thus the surface treatment by environmental conditions (vacuum, pressure, etc.) between calibration and experiment may have effects.

Adams and Manley also found that the output was usually a series of pulses lasting for about 1 sec. The reason for this was positive ion feed-back. It was prevented by introducing curvature in the channel so that the positive ions struck the wall before they had gained sufficient energy to cause secondary electron emission.

Measured dark currents of the order of 10^{-12} ampere have been reported but these are largely due to leakage currents, and reductions to 10^{-13} ampere can be achieved with special insulation. Dunkelman reports dark currents of as low as one electron per minute (presumably photoelectron), a photo current of 3×10^{-21} ampere or dark current of 3×10^{-16} ampere for a gain of 10^5. Michels and Hunter[42] report gains of 10^3 - 10^4. Adams and Manley report gains in the region 10^8 - 10^9 with applied voltages up to 4 kV. It is evident that this type of photomultiplier can be made in a variety of shapes and sizes with properties selected for special applications, thereby causing variations in the gains. Adams and Manley also describe a two-dimensional array of multipliers used for image intensification, here a large number of small channels are fused together.

Noise

Noise in photomultipliers is essentially of two kinds:

i) shot noise, due to the random nature of photoemissions, and

ii) Johnson noise, due to thermal agitation in the resistive components.

In addition there are other spurious signals, especially those due to the positive ions, which may be accelerated sufficiently to cause secondary emission or fluorescence. These are not strictly noise but contribute to the general background.

Shot noise is usually the most important in a photomultiplier. The chief source is the random emission from the cathode, since emission from the dynodes has reduced amplification after the initial stage. The expression for the mean square noise current is

$$\overline{i^2} = 2e\ i\ \Delta f$$

where i is the current leaving the photocathode and Δf is the bandwidth. This must be multiplied by the gain to give the root-mean-square noise current in the output. Johnson noise is given by the mean square voltage generated across a resistance R,

$$\overline{V^2} = 4\ kT\ R\Delta f$$

where R is the resistance at the input of the amplifier, or output of the photomultiplier. The dynode amplification chain in a photomultiplier introduces only a little additional noise. Shockley and Pierce[43] found that if the noise in the cathode current is shot noise, if at each dynode the number of secondary electrons for each primary electron has a Poisson distribution, and if the gain of each stage is the same, then the amplification process increases the mean square noise by a factor

$$G\ \frac{Gg-1}{(g-1)} \approx \frac{g}{g-1} \approx \frac{4}{3}$$

where G is the total gain and g is the stage gain. This does not include channel multipliers.

The ratio between the shot noise and Johnson noise is seen to be

$$r=G\left(\frac{2e\ iR}{4\ kT}\right)^{1/2} = 76\ G\left(\frac{iR}{T}\right)^{1/2}$$

where iR is expressed in volts and T in °K. At T equals 300°K, r is approximately 4 G(iR) $^{1/2}$. At a gain of 10^5 and resistance 10^5 ohms, for example, r = 1 for i equals 10^{-15} A, so that there is little doubt that Johnson noise can be neglected. In a high flux situation one might use a gain of only 10^2 and a resistance of 10^2 ohms (providing the anode current is not too great) in which case equality is achieved for i = 6 x 10^{-8} A. This is an unreasonable photocurrent so that it is evident that Johnson noise must predominate. The resistance R has been treated here as the multiplier anode load; in fact this resistance is intimately related to the data handling and telemetry system. It is worth considering one more case, with a resistance of 10^{10} ohms, such as may be used in conjunction with an electrometer amplifier. For a gain of unity, equality between the two kinds of noise is achieved for i = 6 x 10^{-12} A, while for smaller currents the Johnson noise predominates. There is, of course, the additional shot noise introduced by the electrometer amplifier. For an electrometer tube this is due to the grid current and may be as low as 2 x 10^{-15} A (negligible).

Application to Reentry Spectrophotometry

With the data from the monochromator system of the previous section the performances of photomultipliers with tungsten (no window) and Cs-I (with LiF window) cathodes were computed and plotted in Figure 28. The main feature of this figure is the very wide range in gain required in different spectral regions. With an upper limit of 10^{-9} A for channel multipliers it appears that these can be used. For an instrument bandwidth Δf = 1 MHZ, the signal-to-noise ratio (s) is, for Gi = 10^{-9} A,

a) shot noise

$$s = \sqrt{\frac{i}{2\, e\, \Delta f}} = \sqrt{\frac{I}{G}}$$

b) Johnson noise R = 10^{10} ohms. T = 300°K

$$s = Gi \sqrt{\frac{R}{4\, kT\, \Delta f}} = 776$$

so that, for all cases in which G $>$ 1, shot noise predominates; the signal-to-noise ratios at the various wavelengths in Figure 28 can be obtained from the relation above. Since 10^{-9}A appears to be the maximum current for a channel multiplier it suggests that these devices may not be suitable for the whole

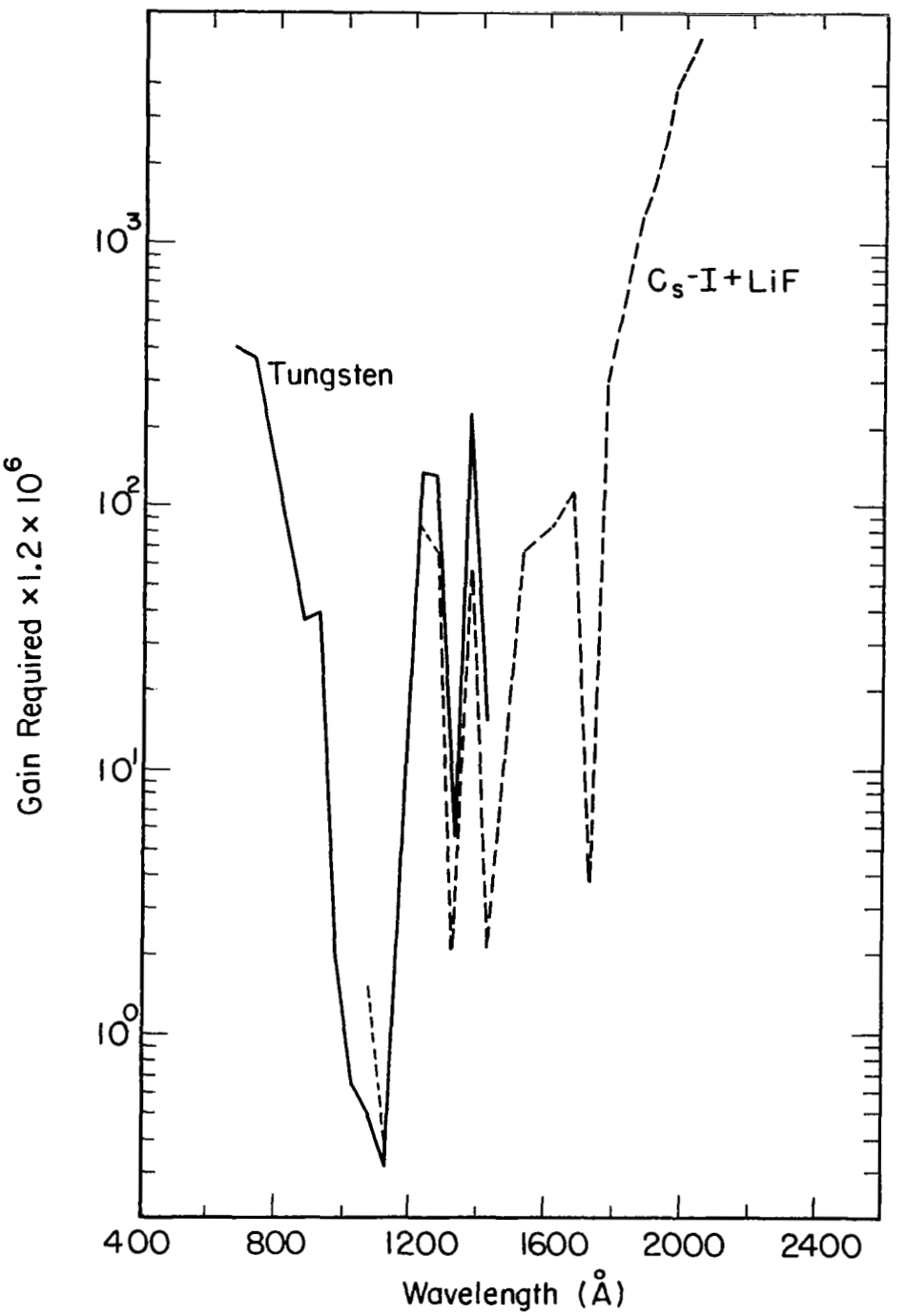

FIGURE 28. GAIN REQUIRED TO GIVE OUTPUT OF 10^{-9} AMPERE. (i.e. A GAIN OF 1.2 x 10^6 INDICATES THAT THE CURRENT LEAVING THE PHOTOCATHODE IS 10^{-9} AMPERE)

spectral range. This limitation probably applies generally to small multipliers and is most severe for the smallest, the channel multiplier.

Conventional multipliers, or resistance strip multipliers are bulky and should be avoided if possible. The tungsten photocathode is convenient but it may be preferable to use a different material for the long wavelengths, alternately other instrument design parameters (e.g. grating blaze and reflectivity profile for a spectrometer) could be modified.

In conclusion, the small size of the channel multiplier makes it a convenient and suitable detector. However, the instrument as a whole should be designed so that the gain required is small and the channel operates near maximum current in order to reduce the noise. More than one photocathode material may be desirable to cover the whole spectral region.

3. Photoconductive Detectors

When radiation is incident on a material it can be both reflected and absorbed. If absorbed, the photons, depending on their energy, can (1) eject electrons from the material's surface, photoemission, (2) move electrons from the valence band to the conduction band in semiconductors and insulators where they may then move freely, photoconduction, (3) form electron-hole pairs which remain bound, excitons, or (4) generate phonons. For conductive metals, where there is a continuation of energy states below the Fermi level, the photon must possess sufficient energy in excess of the work function Φ (Figure 29) to cause photoemission. The excess photon energy is transformed into the kinetic energy of the escaping electron.

Semiconductors and insulators are materials that have an energy gap E_g between their valence and conduction bands. A material is considered to be an insulator when the band gap exceeds approximately two ev. To obtain photoemission in these materials the photon energy must lift the electron through the band gap plus the surface barrier E_a. Figure 30 shows the energy levels for semiconductors, e.g. cesium-antimony has an E_g of 1.55 ev and an E_a of 0.45 ev. Table 7 lists the work functions for various elements and Table 8 lists the band gaps for various materials. The values of Table 8 are taken from Buba who gives no indication of how they were determined.

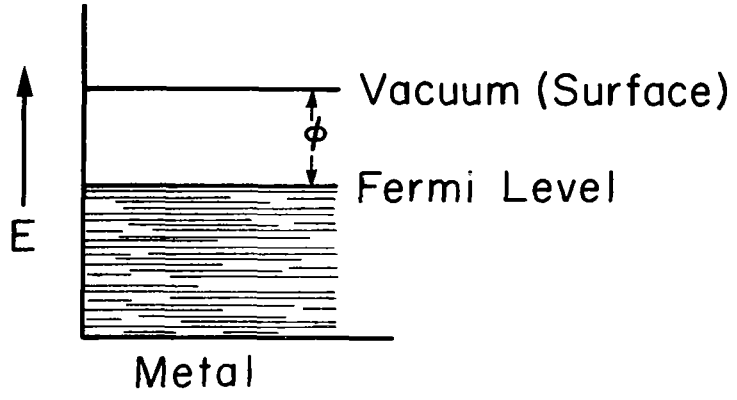

FIGURE 29. STATES IN A METAL (CONDUCTOR).

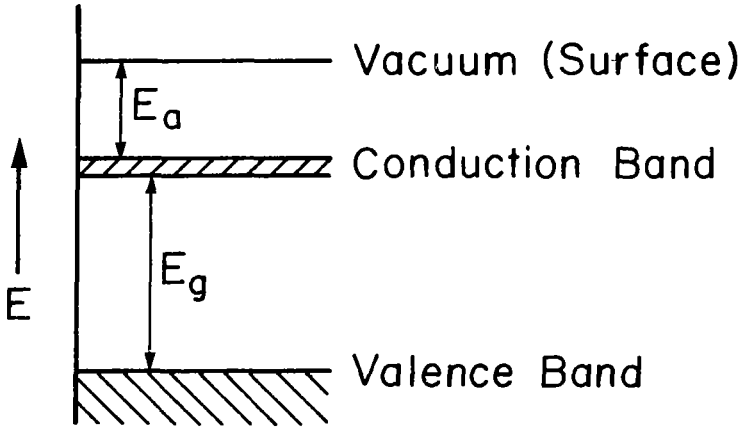

FIGURE 30. STATES IN A SEMICONDUCTOR.

Table 7

WORK FUNCTION OF ELEMENTS

Material		Photoelectric Work Function, Ø ev	Material		Photoelectric Work Function, Ø ev
Silver	Ag	3.7-4.7	Lead	Pb	4.0
Aluminum	Al	3.0-4.4	Palladium	Pd	5.0
Arsenic	As	4.7	Platinum	Pt	4.1-6.3
Gold	Au	4.7	Rubidium	Rb	2.1
Boron	B	4.4-4.6	Rhenium	Re	5.0
Barium	Ba	2.5	Rhodium	Rh	4.6
Beryllium	Be	3.3	Antimony	Sb	4.1-4.6
Bismuth	Bi	4.1-4.6	Selenium	Se	4.6-5.1
Carbon	C	4.8	Silicon	Si	4.4-4.7
Calcium	Cd	3.7-4.0	Tin	Sn	3.6-3.8
Cerium	Ce	2.8	Strontium	Sr	2.1-2.2
Cobalt	Co	3.9-4.2	Tantalum	Ta	4.1
Chromium	Cr	4.4	Tellurium	Te	4.0-4.7
Cesium	Cs	1.9	Thorium	Th	3.4-3.6
Copper	Cu	4.1-5.6	Titanium	Ti	4.0-4.4
Iron	Fe	3.9-4.7	Thallium	Tl	3.7
Germanium	Ge	4.3-4.8	Uranium	U	3.6
Gallium	Ga	4.0	Vanadium	V	3.8
Mercury	Hg	4.5	Tungsten	W	4.4-4.6
Iodine	I	2.8-6.8	Zinc	Zn	3.1-4.3
Iridium	Ir	4.5	Zirconium	Zr	3.7-4.3
Lithium	Li	2.3			
Magnesium	Mg	2.7-3.7			
Manganese	Mn	3.8			
Molybdenum	Mo	4.2			
Sodium	Na	2.1-2.5			
Nickel	Ni	3.7-5.0			

Note: Work functions from Handbook of Chemistry and Physics, 1958.

Table 8

BAND GAPS OF MATERIALS
(in electron volts)

Material	Band Gap	Material	Band Gap
Si	1.10	ZnSb	0.56
Ge	0.68	Cd_3P_2	0.55
Se	2.1	Cd_3As_2	0.55
Te	0.34	CdSb	0.50
Ga	2.25	CaS	5.4
Na_eSb	1.1	CaSe	5.0
KSb	0.9	CaTe	4.3
K_3Sb	1.1	MgSe	5.6
Rb_3Sb	1.0	MgTe	4.7
CsSb	0.8	ZnO	3.2
Cs_3Sb	1.6	ZnS	3.7
Cs_3Bi	0.5	ZnSe	2.6
BN	0.3	ZnTe	2.1
Cu_2O	2.0	SrO	5.8
Ag_2S	0.9	SrS	4.8
Ag_2Te	Low T: 0.67	SrSe	4.6
	High T: 0.98	SrTe	4.0
CuBr	2.9	CdS	2.4
AgI	2.8	CdSe	1.7
Mg_2Si	0.7	CdTe	1.5
Mg_2Ge	0.6	BaO	4.2
Mg_2Sn	0.3	BaS	4.0
Ca_2Si	1.9	BaSe	3.7
Ca_2Sn	0.9	BaTe	3.4
Ca_2Pb	0.46	HgS ("red")	2.0
Mg_3Sb_2	0.82	HgSe	0.6
Zn_3P_2	1.15	HgTe	0.02
Zn_3As_2	1.0	HgI_2	Low T: 2.13
			High T: 2.55

Table 8 (Cont'd)

Material	Band Gap	Material	Band Gap
AlAs	2.4	PbS	0.40
AlSb	1.5	PbSe	0.25
GaN	3.4	PbTe	1.31
GaP	2.24	As_2O_3	4.0
GaAs	1.4	As_2S_3	2.5
GaSb	0.67	As_2Se_3	1.7
InP	1.25	As_2Te_3	1.1
InAs	0.33	Sb_2O_3	4.2
InSb	0.18	Sb_2S_3	1.7
Al_2O_3	>5	Sb_2Se_3	1.2
Al_2S_3	4.1	Sb_2Te_3	0.3
Al_2Se_3	3.1	Bi_2O_3	3.2
Al_2Te_3	2.5	Bi_2S_3	1.3
Ga_2O_3	4.4	Bi_2Se_3	0.35
GaS	2.5	Bi_2Te_3	0.15
Ga_2S_3	2.5	TeO_2	1.5
GaSe	2.0	MoS_2	1.2
Ga_2Se_3	1.9	$PbCO_3$	4.4
GaTe	1.5	$PbCrO_4$	2.3
Ga_2Te_3	1.2	H_3BO_3	5.1
In_2O_3	3.5	(Group Ia) VO_3	3
In_2S_3	2.0	LiMgSb	0.7
InSe	1.2	LiMgBi	0.4
In_2Se_3	1.2	$ZnSiAs_2$	2.1
In_2Te_3	1.0	$ZnGeP_2$	2.2
Tl_2S	1.2	$ZnSnP_2$	2.1
SiC	cub: 2.3	$CdGeP_2$	1.8
	hex: 2.9	$CdSnP_2$	1.5
TiO_2	3.0	$ZnIn_2Se$	2.6
SnO_2	4.3	$ZnIn_2Te_4$	1.4
SnS	1.3	$CdIn_2Te_4$	0.9
PbO	2.3	$HgIn_2Se_4$	0.6

Table 8 (Cont'd)

Material	Band Gap	Material	Band Gap
$CuIn_2Se_4$	0.6	$CuFeTe_2$	0.1
$CuInS_2$	1.2	$CuHgI_4$	2.1
$CuInSe_2$	0.9	$AgInS_2$	1.2
$CuInTe_2$	0.9	$AgInSe_2$	1.0
$CuFeS_2$	0.5	$AgFeSe_2$	0.23
$CuFeSe_2$	0.2	$AgFeTe_2$	Low T: 0.28
			High T: 0.58

Note: From R. Buba, Photoconductivity of Solids (John Wiley & Sons, New York) p. 230, 1960.

Photoconductivity results when the incident photons excite electrons from the valence to the conduction band or to a state where they may be further excited by another photon or phonon. These charges or charge centers are then moved by the application of an electric field. Conductivity results from the motion of either electrons or holes. Other processes such as electron-hole mobility and carrier lifetime, also govern the photoconduction.

Photoconductive materials fall into two general classes called intrinsic (idiochromatic) and extrinsic (allochromatic). Intrinsic materials show photoconductivity when in a pure form while extrinsic materials have impurities which establish localized energy levels inside of the band gap. These levels permit excitation by lower energy photons and, consequently, the extrinsic material is sensitive to longer wavelength radiation. Extrinsic materials may also be excited by photons which lift an electron across the entire band gap. The absorption and photoconductivity dependence on wavelength (photon energy) can be seen in Figure 31.

For photon energies slightly less than the band gap, absorption by the formation of an exciton may be quite probable. Excitons can move through a lattice since they are electrically neutral, however, they may easily be excited to a free carrier state[44]. Another way of determining the approximate value of the energy gap is to measure the absorption of these materials. Table 9 lists the long wavelength edge of the strong absorption region.

Extrinsic materials usually result from other materials occupying positions in a crystal lattice normally filled by the bulk material. Figure 32 shows some of the possible impurity levels in germanium. Due to these levels, not only excitation but also recombination or trapping can occur. The various mechanisms are shown in Figure 33. Since extrinsic conductivity can rely on relatively small energy gaps, these materials are usually quite temperature dependent.

A photoconductive detector incorporates a material which has an energy band gap slightly lower than the incident photon energy thereby permitting the excitation of charge carriers. With ohmic contacts (no contact potential is generated where materials meet), the device can be treated as a variable resistance with a voltage, E_B, applied across it. A typical detector circuit is shown in Figure 34. The charge pairs created by incident photons results in a variable current flowing through the external resistor R_L.

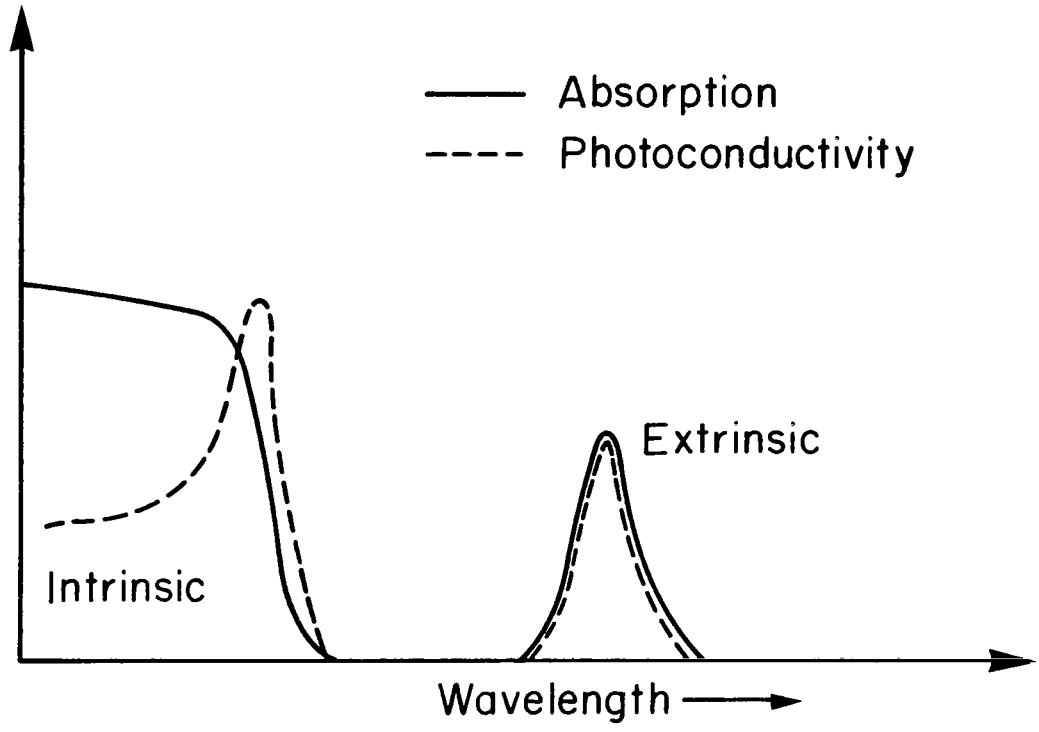

FIGURE 31. TYPICAL DEPENDANCE OF ABSORPTION AND PHOTOCONDUCTIVITY ON WAVELENGTH FOR INTRINSIC AND EXTRINSIC REGIONS.

Table 9

LONG WAVELENGTH EDGE OF STRONG ABSORPTION REGION

Material	Strong Absorption After, ev	Material	Strong Absorption After, ev
MgSe	4.7	Ga_2O_3	4.4
MgTe	3.3	InCl	2.8
MgO	6.9,7.3	SnO_2	4.0
CaS	5.0	SnO	4.0
CaSe	4.3	As_2O_3	3.9,3.7
CaTe	3.8	$PbCl_2$	4.3
SrS	4.6	$PbBr_2$	3.3
SrSe	4.2	Sb_2O_3	4.1,4.4
SrTe	3.5	TlCl	3.9
SrO	5.7	$CdCl_2$	5.6
BaO	3.8,4.0	$CdBr_2$	4.3
BaS	3.8	CdI_2	3.7
BaSe	3.5	$NiCl_2$	4.0
BaTe	2.8	$NiBr_2$	3.0
ZnO	3.2,3.3	$CoCl_2$	4.2
ZnS	3.7	$CoBr_2$	3
$ZnCl_2$	6.2	Bi_2O_3	3.5,2.8
ZnI_2	4.1	Ta_2O_5	4.3
		ZrO_2	5.1

Note: From M. L. Schultz and W. E. Hartz, "Solid State Ultraviolet Photodetectors," AFAL-TR-66-328, p. 12,13, December 1966.

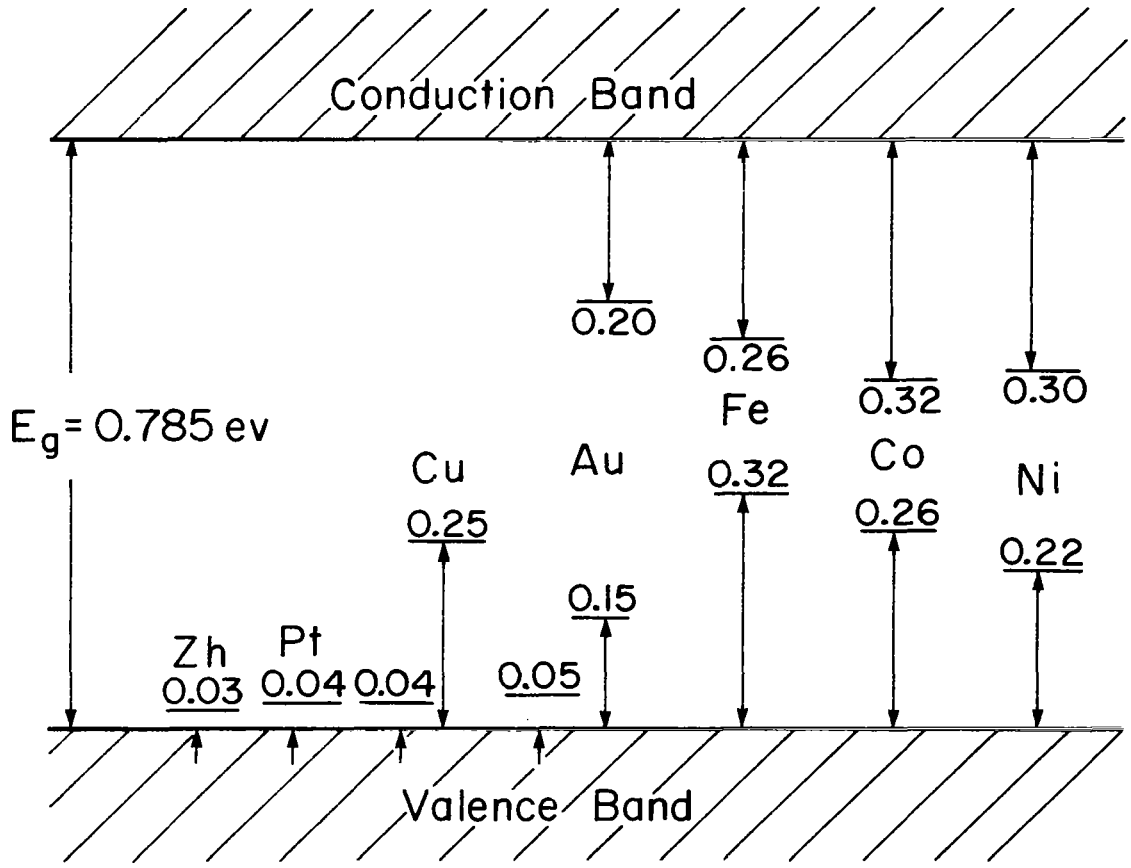

FIGURE 32. IMPURITY ENERGY LEVELS IN GERMANIUM.

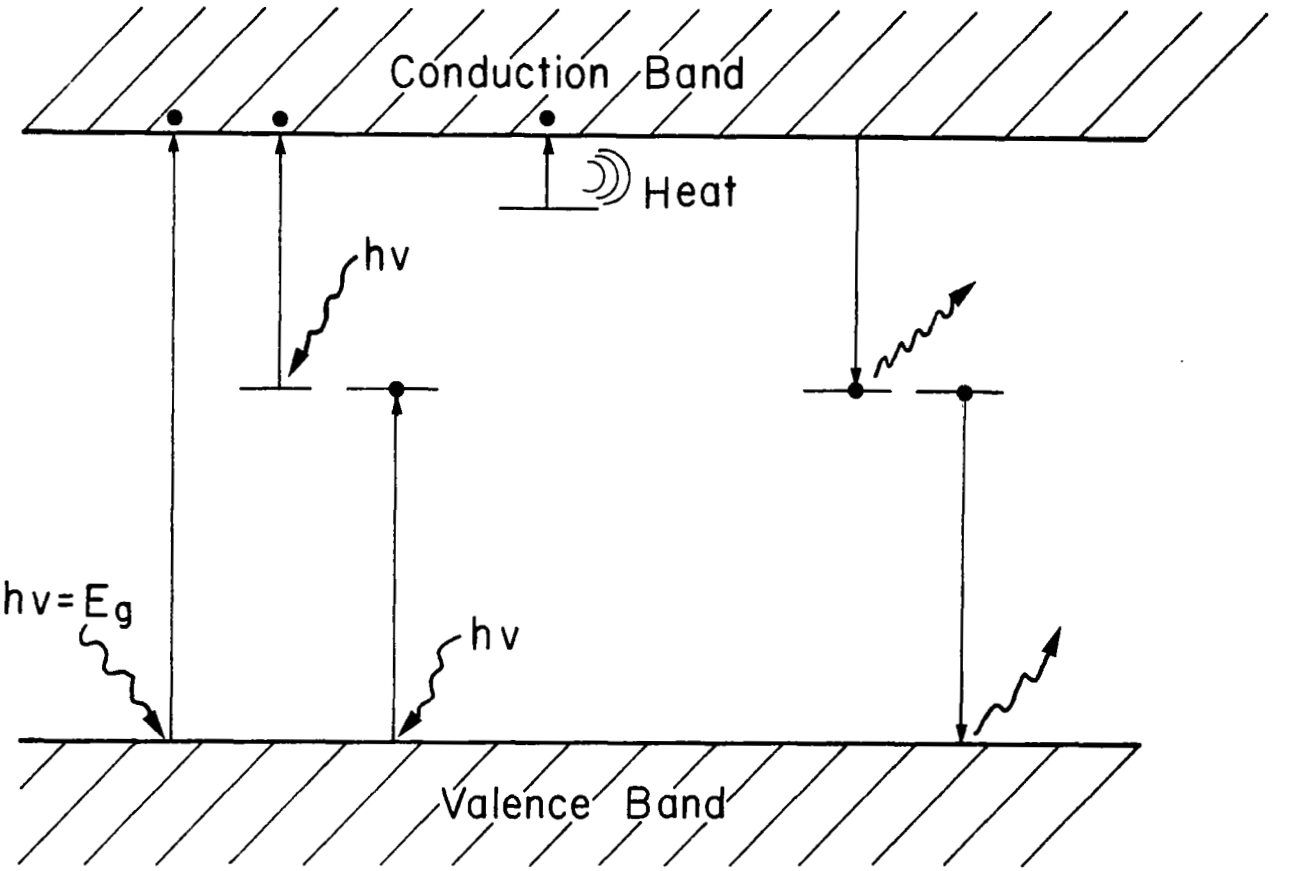

FIGURE 33. EXCITATION AND TRAPPING PROCESSES IN SEMICONDUCTORS.

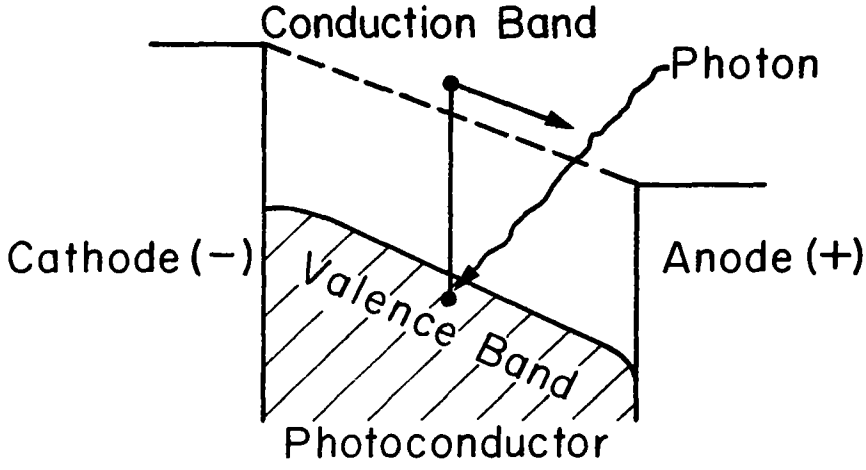

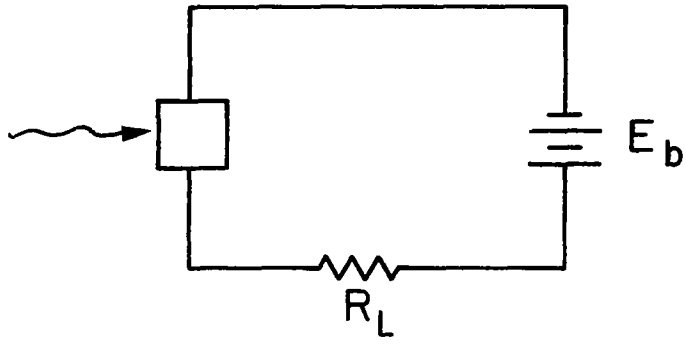

FIGURE 34. PHOTOCONDUCTIVE DETECTOR CIRCUIT.

Detailed discussions of detector operation have been presented in many papers and books [45,46]. However, very little work has been done with vacuum UV photoconductive devices. Some investigations which have been made with stannic oxide and solutions of magnesium sulfide in zinc sulfide show promising results[54]. Also, it has been shown that certain lead sulfide photocells are sensitive in the UV.

Detectivity

In order to analyze the relative performance of detectors certain concepts such as detectivity have evolved. The signal from a detector in volts, S, is given by

$$S = \frac{E_b \, \Delta R_D \, R_L}{(R_D + R_L)^2} \quad \text{volts}$$

where R_D and R_L are the detector and load resistance, respectively, ΔR_D is the change in detector resistance when exposed to radiation, and E_b is the emf bias of the battery.

The ability to detect radiation depends not only on the output signal but also on the noise level which is expressed in the signal-to-noise ratio, S/N. The three types of noise which generally limit the performance of photoconductive detectors are Johnson noise, 1/f noise, and charge carrier fluctuation noise. The 1/f noise is significant only at low frequencies and usually requires that the radiation be chopped or modulated at some frequency f. Johnson noise is present in all resistances and is important at high frequencies. The charge carrier fluxation or generation-recombination noise occurs in all semiconductors and depends on f, Δf, the bandwidth of the amplifier, and the material temperature [47].

The specific detectivity D* compares all photon detectors by normalizing the S/N ratio per watt to a one cm^2 detector area and a certain bandwidth Δf. It is defined by the expression

$$D^* = \frac{S/N}{H} \, (A \, \Delta f)^{1/2}$$

where H is rms radiation incident on the detector and A is its area[48]. For optimum operation the detector bias voltage, E_b, and load resistance, R_L, must also be properly chosen.

Temperature Dependence and Memory

The temperature of semiconductors effects the energy band gap, recombination time, carrier density, and carrier mobility. For most materials the band gap decreases with increasing temperature and, in most cases the detector noise increases. Some of the temperature dependent parameters are interrelated and can be adjusted by variations in the specific detector fabrication.

Another phenomenon present in certain detectors is a long-term memory to previous light exposure. After exposure to high light levels the cell may become less sensitive and somewhat faster in response. Such changes are reversible and for measurements the cell is "light-preconditioned" to assure consistent readings.

Pressure Dependence

The energy band gap is also pressure dependent and usually increases with increasing pressure in the low pressure region. For pressure changes of the order of 2 to 3 atmospheres the band gap increases about 3×10^{-5} ev for most semiconductors. Such a small change will have a negligible effect on any detector system. Consequently, the expected reentry vehicle pressure changes should have no effect on a solid state detector.

Photoconductive Properties

The photoconductivity response of semiconductor materials peaks at a wavelength slightly longer than that at which the absorption rises steeply. For shorter wavelengths the radiation is strongly absorbed and produces excitation only near the surface. The surface characteristics are such that rapid non-radiative-recombination trapping takes place along with the possible photoemission of carriers. Longer wavelength radiation cannot produce the excitation required to remove the electron to the conduction band. Figure 35 shows the response curves for a variety of materials. These photoconductivity response peaks can be related directly to the absorption curves of Figure 36. From the previous figures it is evident that for the effective detection of vacuum UV radiation, a high energy gap material must be used.

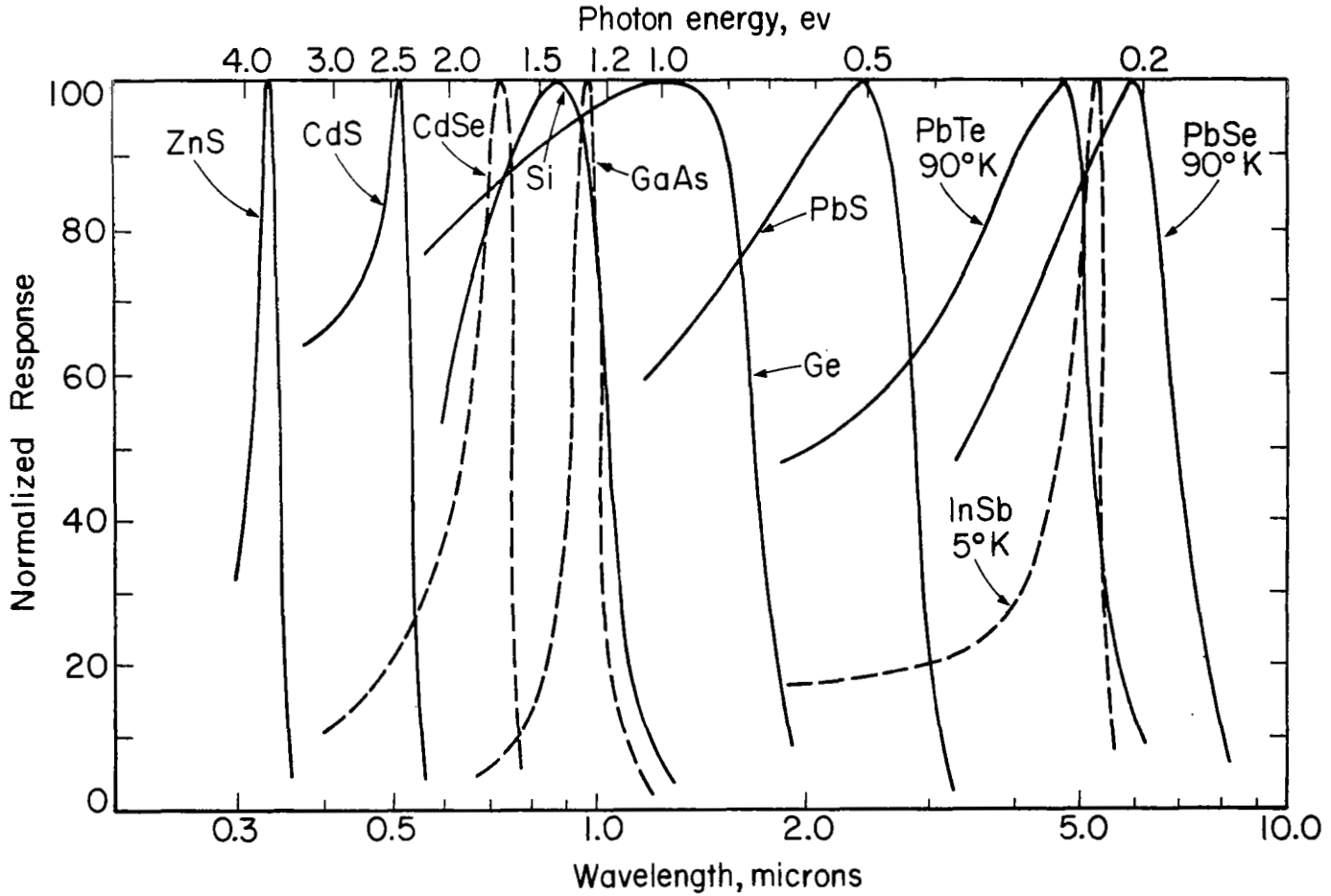

FIGURE 35. PHOTOCONDUCTIVITY RESPONSE CURVES FOR TYPICAL PHOTOCONDUCTORS. (FROM BUBA)

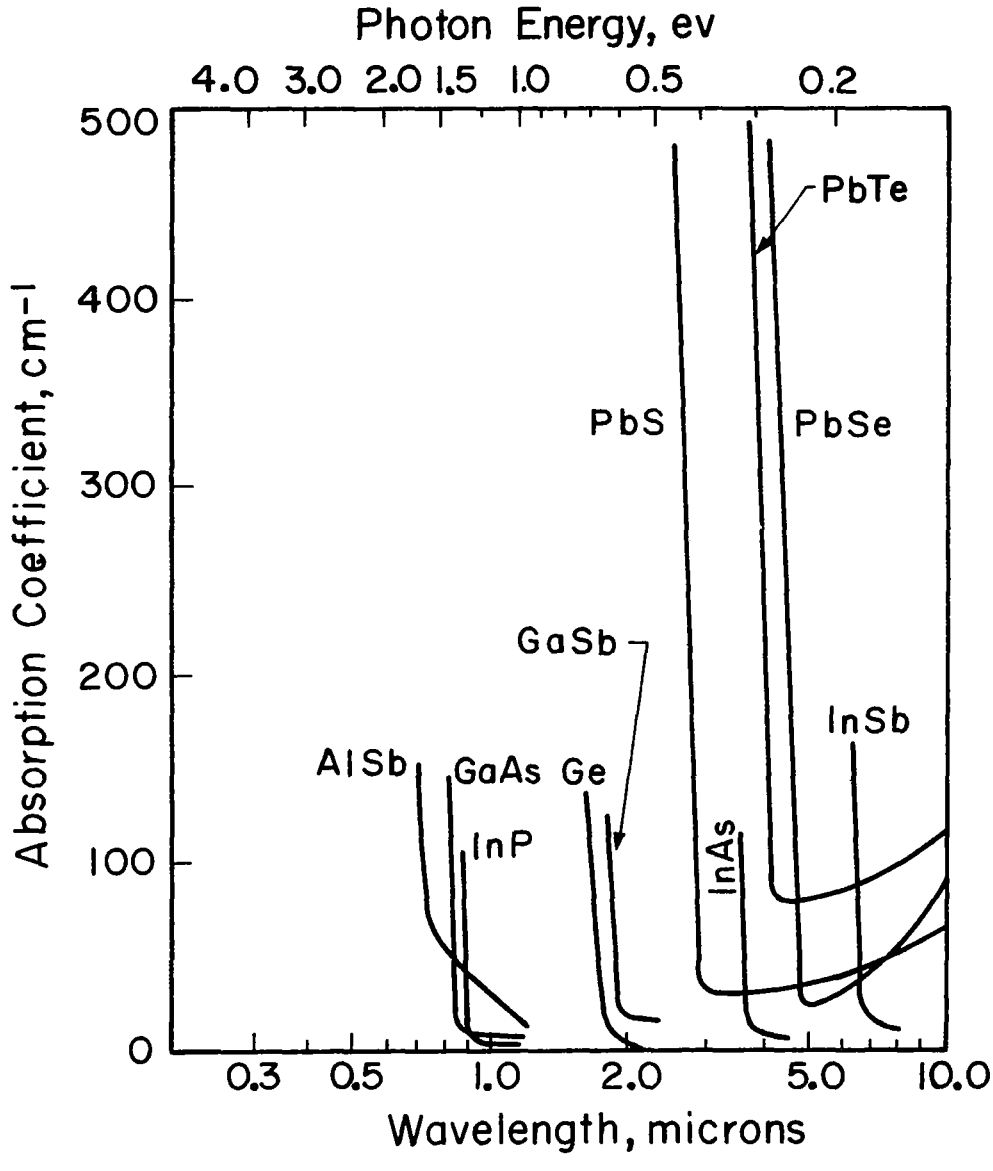

FIGURE 36. ABSORPTION COEFFICIENT FOR VARIOUS MATERIALS. (FROM BUBA)

Operational Detectors

Since only limited knowledge exists concerning detector performance in the vacuum UV, the performance of detectors in the visible and near UV must be extrapolated to the region of interest. Table 10 lists the characteristics of various detectors.

Cadmium sulfide photocells (CdS)

These cells which have two metal electrodes located on top of the photoconductive material, have been commercially available for many years. Figure 37 is the spectral response curve for a typical RCA cell with a glass window. An RCA type SQ2535 cell with a face about 1/8 in. in diameter has the response of Figure 38. These cells also have long term memory and the temperature dependence shown in Figure 39.

Lead sulfide (PbS)

The response of lead sulfide cells have been measured down to 2000 Å with the quantum sensitivity remaining roughly constant for wavelengths greater than 6000 Å and rising for shorter wavelength radiation. This increase in quantum yield is attributed to secondary internal photoemission. For a PbS layer of 1/4 by 1/4 mm in area with evaporated gold electrodes the following characteristics were obtained:

Resistance (megohms)	0.47
Load resistance (megohms)	2.2
Polarizing voltage (volts)	6
Chopping frequency (cps)	90
Flux density ($\mu w/cm^2$)	0.71
Radiation, peak (angstroms)	2600
bandwidth (angstroms)	120
Signal (a.c., wideband amp., μv)	297
Photocurrent (peak, x 10^{-9} amp)	0.36
Voltage drop across cell terminals	2.62

Table 10

PROPERTIES OF DETECTORS

Material		Energy Gap E_g ev	Application	Response Time microsec	Detectivity D* cm $cps^{1/2}$/watt
Silicon	Si	1.08	Visible, IR		
Germanium					
300°K	Ge	0.66	IR		
77°K	Ge	0.75	IR	5	
Gallium antimonide	GaSb	0.67	IR		
Gallium phosphite	Ga	2.25			
Gallium arsenide	GaAs	1.39			
Indium antimonide	InSb	0.18	IR	1	
Indium phosphide	InP	1.29			
Indium arsenide	InAs	0.36			
Aluminum antimonide	AlSb	1.65			
Lead sulfide	PbS	0.37	IR	100	
Lead selenide	PbSe	0.26	IR	10	
Lead telluride	PbTe	0.31	IR		
Lead oxide	PbO	2.3			
Selenium	Se	1.75			
Zinc oxide	ZnO	3.2	UV		
Zinc sulfide	ZnS	3.7	UV	100	1.9×10^7 (2850 Å)
Zinc selenide	ZnSe	2.6			
Titanium oxide	TiO	3.0	UV		
Titanium dioxide	TiO_2	3.0	UV	100	
Aluminum oxide	Al_2O_3	>5.0			
Boron nitride	BN	0.33			
Silver sulfide	Ag_2S	0.9		400	
Cadmium sulfide	CdS	2.4	Visible	10,000	
Cadmium selenide	CdSe	1.7	Visible	1,000	
Stannic oxide	SnO_2	4.3	UV		4.4×10^{12} (2850 Å)
Lead carbonate	$PbCO_3$	4.4	UV		2×10^7 (2850 Å)
Lead chloride	$PbCl_2$	4.3	UV		2.5×10^7 (3040 Å)
Lead bromide	PbBr	3.3	UV		1.4×10^8 (4500 Å)
Lead iodide	PbI_2		UV		
Antimony oxide	Sb_2O_3	4.2	UV		
Crystals	(Zn,Mg)S		UV		2.1×10^{10} (2850 Å)

Note: For D*: f = 25 cps, Δf = 8 cps, λ given in angstroms.

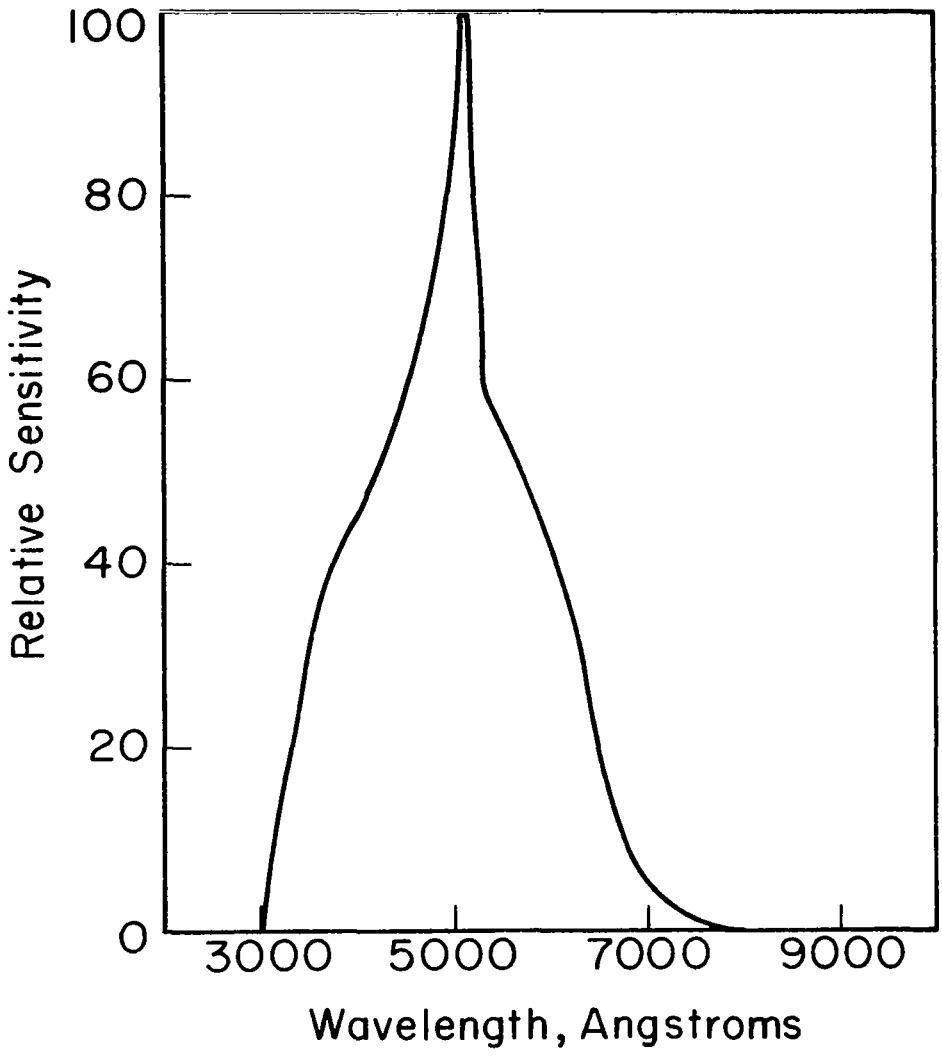

FIGURE 37. SPECTRAL RESPONSE OF RCA CdS PHOTOCELLS

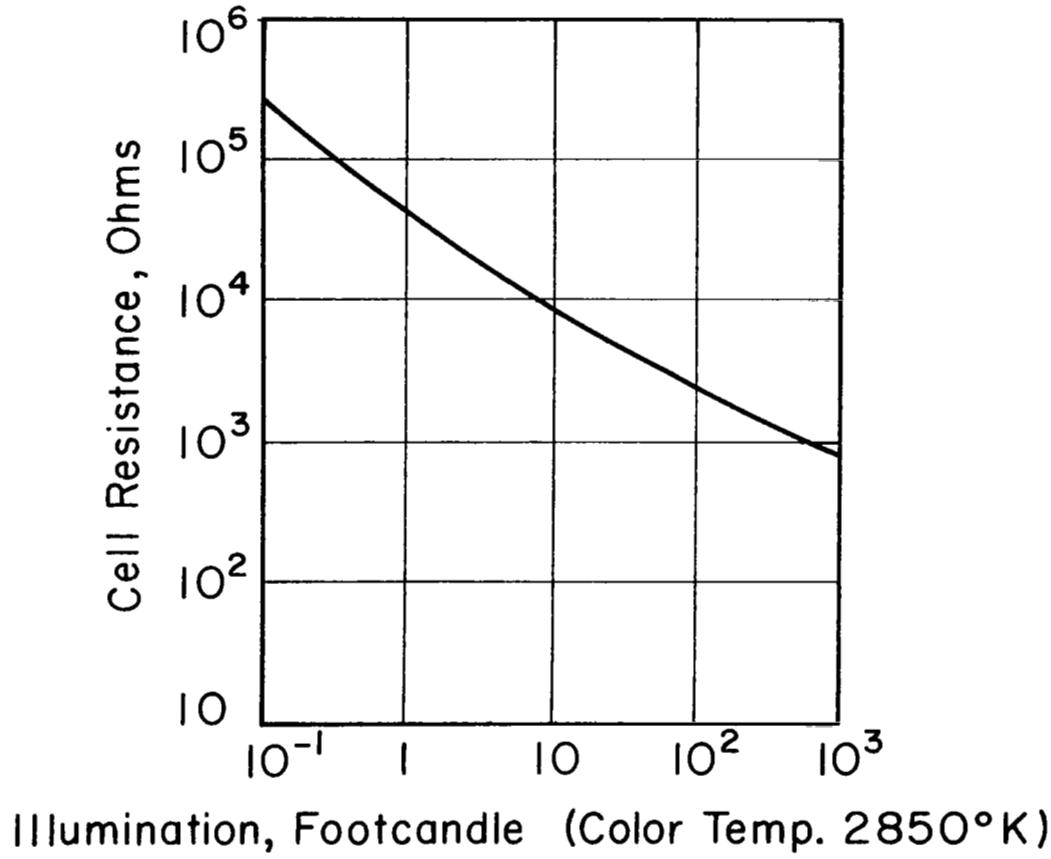

FIGURE 38. RESPONSE OF AN RCA SQ 2535 PHOTOCONDUCTIVE CELL. (RCA BULLITEN 312)

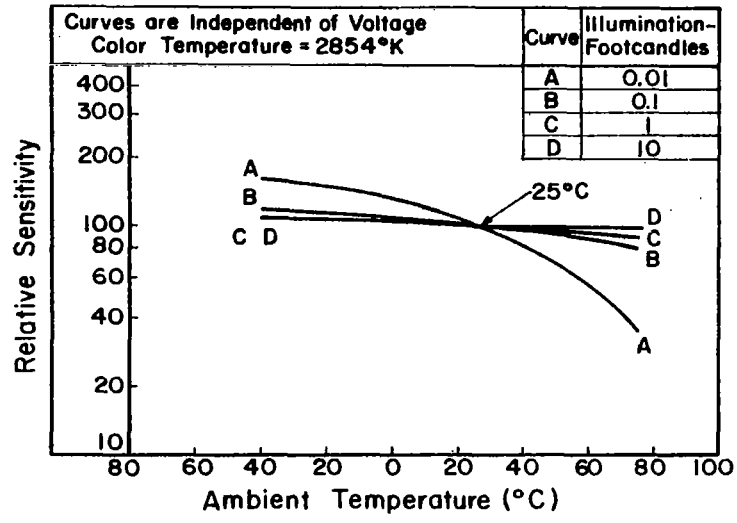

(A)

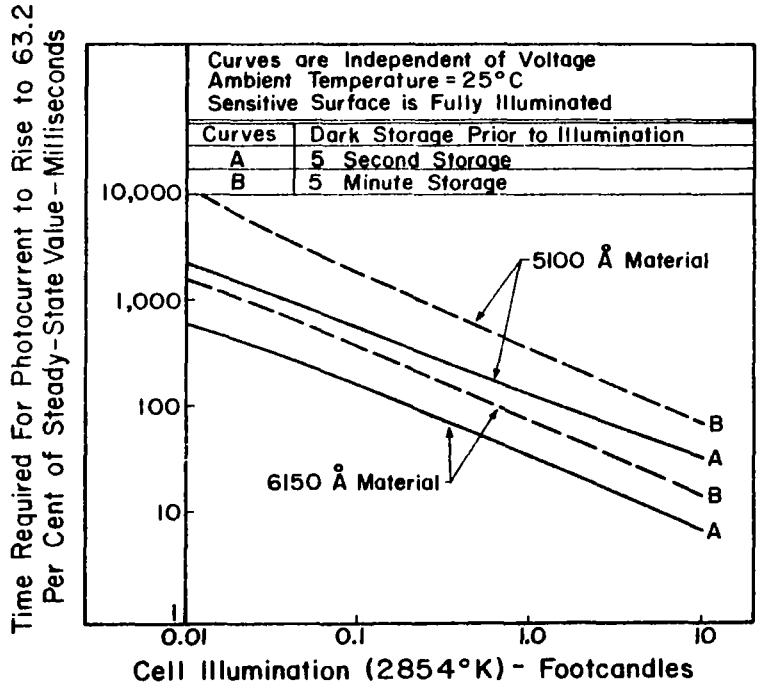

(B)

FIGURE 39. PHOTOCURRENT RISE AND TEMPERATURE CHARACTERISTICS FOR Cd S CELLS. (MANUFACTURES DATA)

Net yield, electrons/incident photon	0.037
Noise in 5 cps bandwidth (μv)	4.4
Temperature (°C)	26°

The spectral response of a 1 mm^2 cell is shown in Figure 40. The relative energy sensitivity is the ratio of the PbS cell signal to the emf of a comparison thermopile. Relative quantum sensitivity is this quantity divided by the wavelength. Figure 41 is the relative quantum sensitivity (per incident quantum) as a function of photon energy[49].

The spectral response of PbS is presented for the long wavelength regions at various temperatures in Figure 42. The detectivities of these detectors have also been measured at 2.5 microns as shown in Figure 43[50]. Various other detectors are compared to PbS at 298°K in Figure 44[51].

Titanium dioxide (TiO_2, rutile)

These detectors were investigated at the University of Michigan, Willow Run Laboratories, for use in the far ultraviolet. Detectivities D*, of 10^{10} to 10^{11} for 3400 Å radiation were measured with the cell voltage biased. The response curve had a very sharp peak with the sensitivity at 2000 Å estimated to be at least 1000 times lower. This is due to the usual high absorption at wavelengths shorter than the peak response. It is felt that surface etching and processing may yield a slightly broader response. The shortest response time for these detectors was on the order of 100 μsec. It was felt that improvements in system impedance matching could moderately improve the detector performance[52].

Zinc oxide (ZnO)

Zinc oxide detectors show peak photoconductivity and a steep rise in absorption at the band gap energy of 3.2 ev (3800 Å) as shown in Figure 45. The response of these cells to shorter wavelength radiation is unmeasured but a decrease in response can be expected. Certainly, absorption very close to the surface is expected and the associated trapping-recombination problems will arise[53].

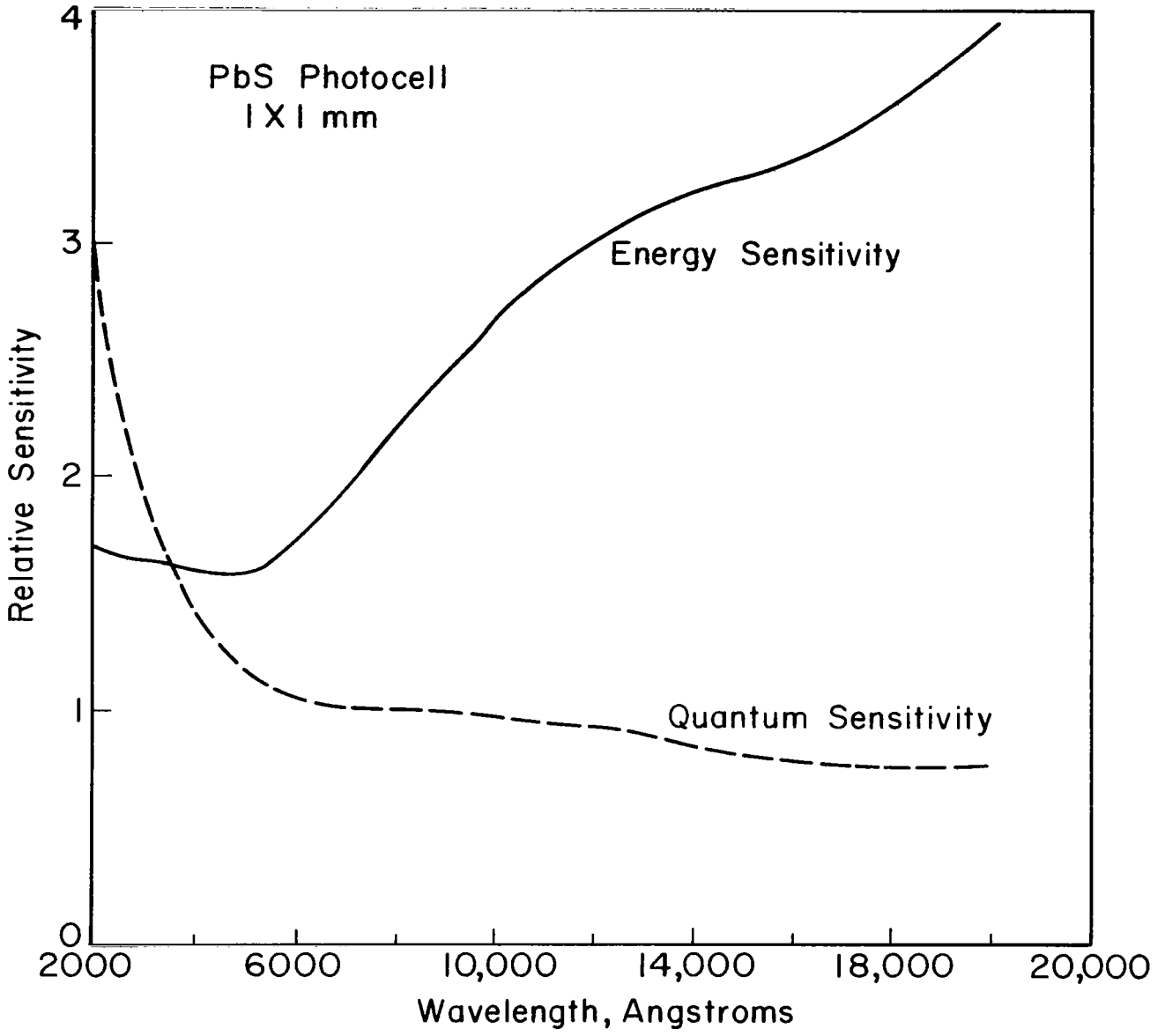

FIGURE 40. SPECTRAL RESPONSE OF A Pb S PHOTOCELL.

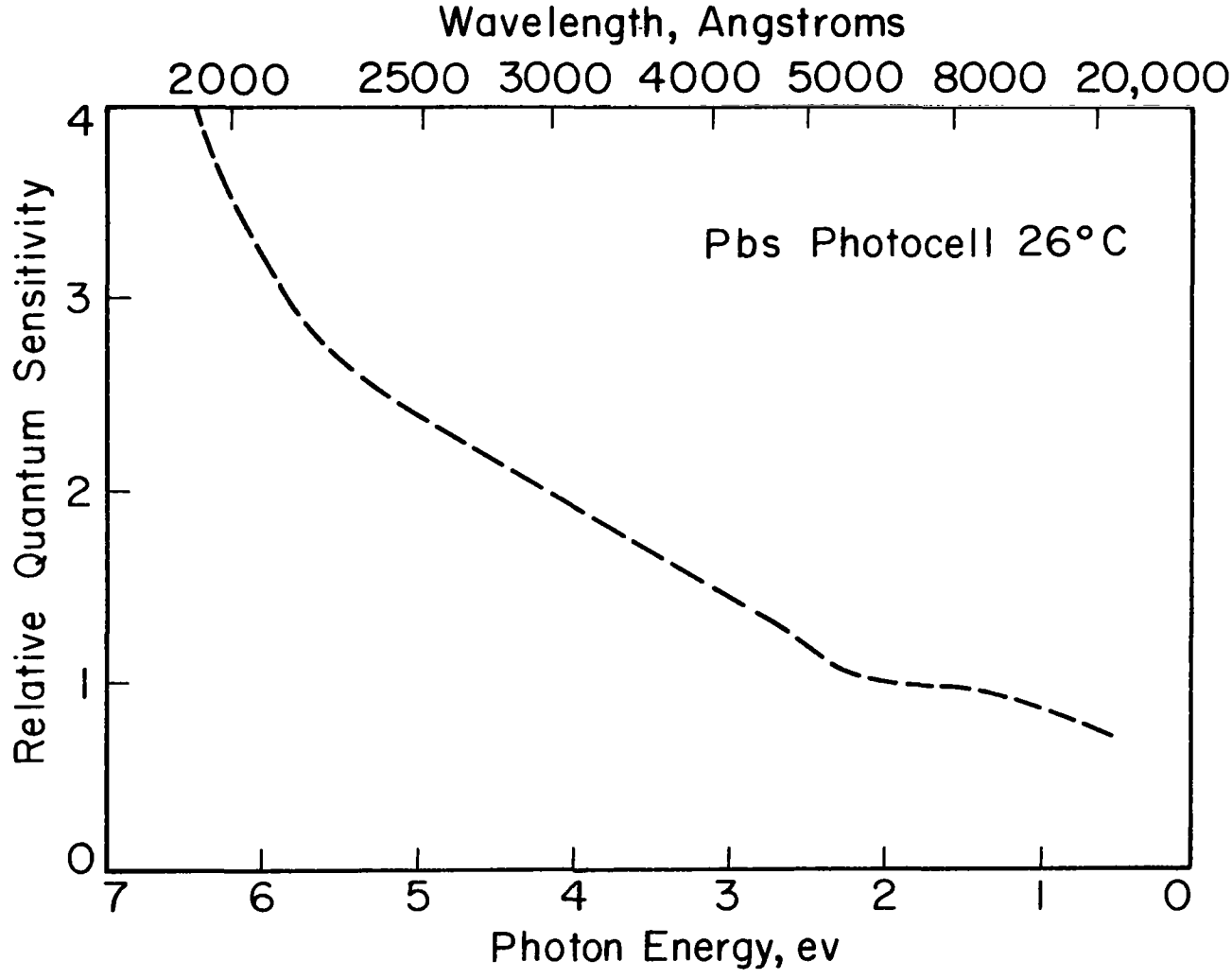

FIGURE 41. RELATIVE QUANTUM SENSITIVITY OF A Pb S PHOTOCELL.

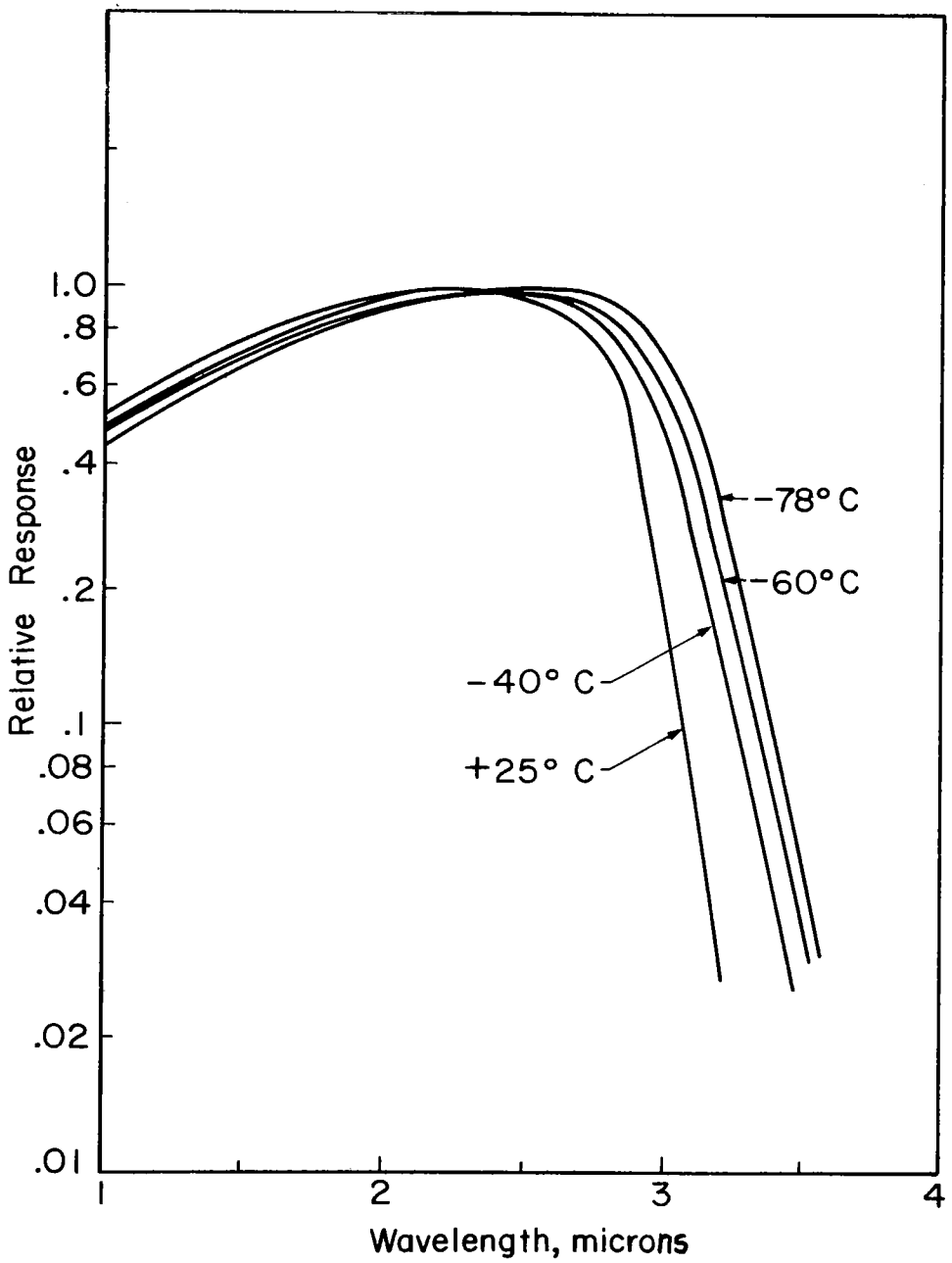

FIGURE 42. SPECTRAL RESPONSE OF Pb S AT VARIOUS TEMPERATURES. NORMALIZED TO UNITY AT 2.25μ. (FROM HUMPHREY)

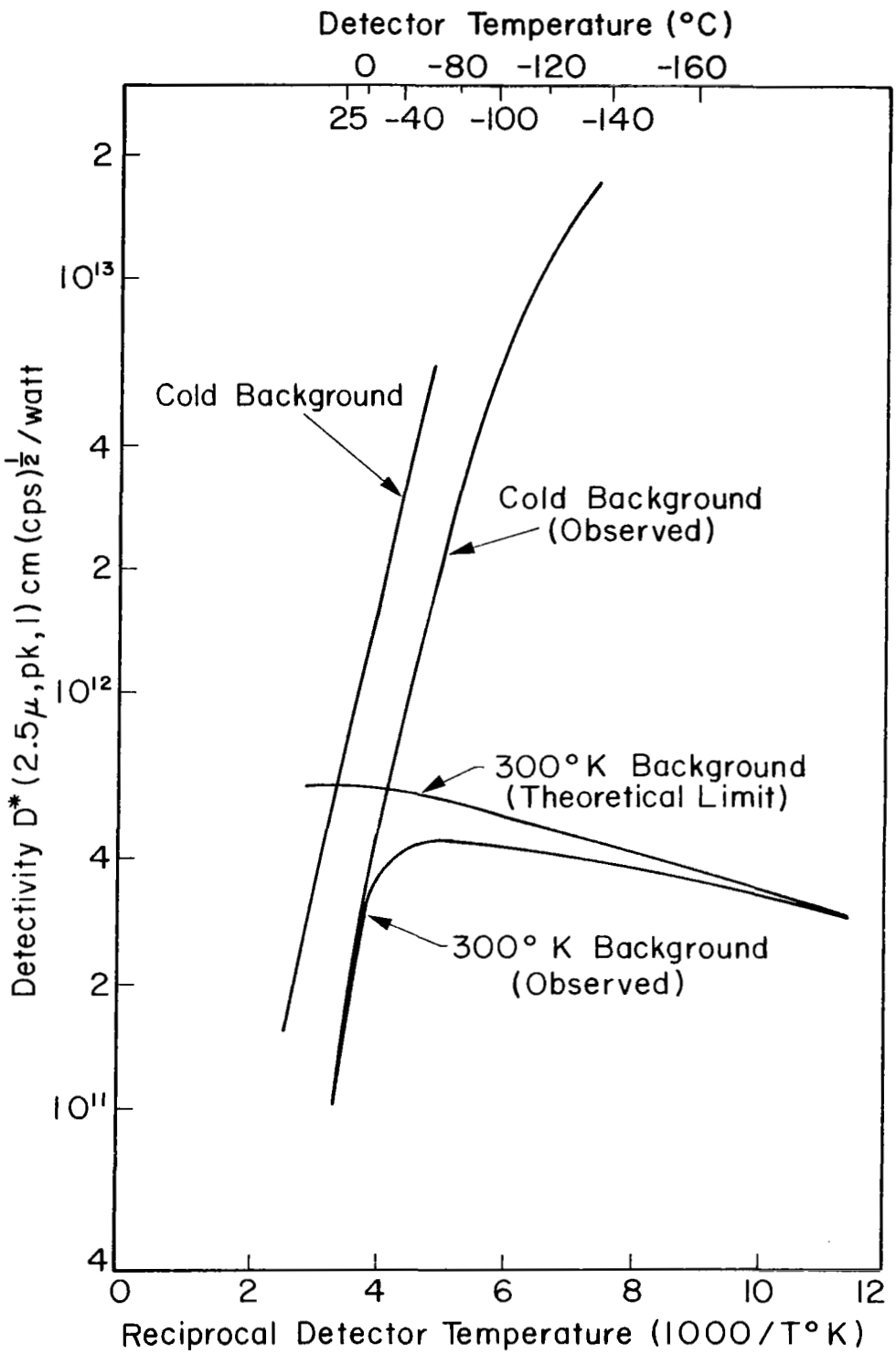

FIGURE 43. DETECTIVITIES OF Pb S DETECTORS. (FROM HUMPHREY)

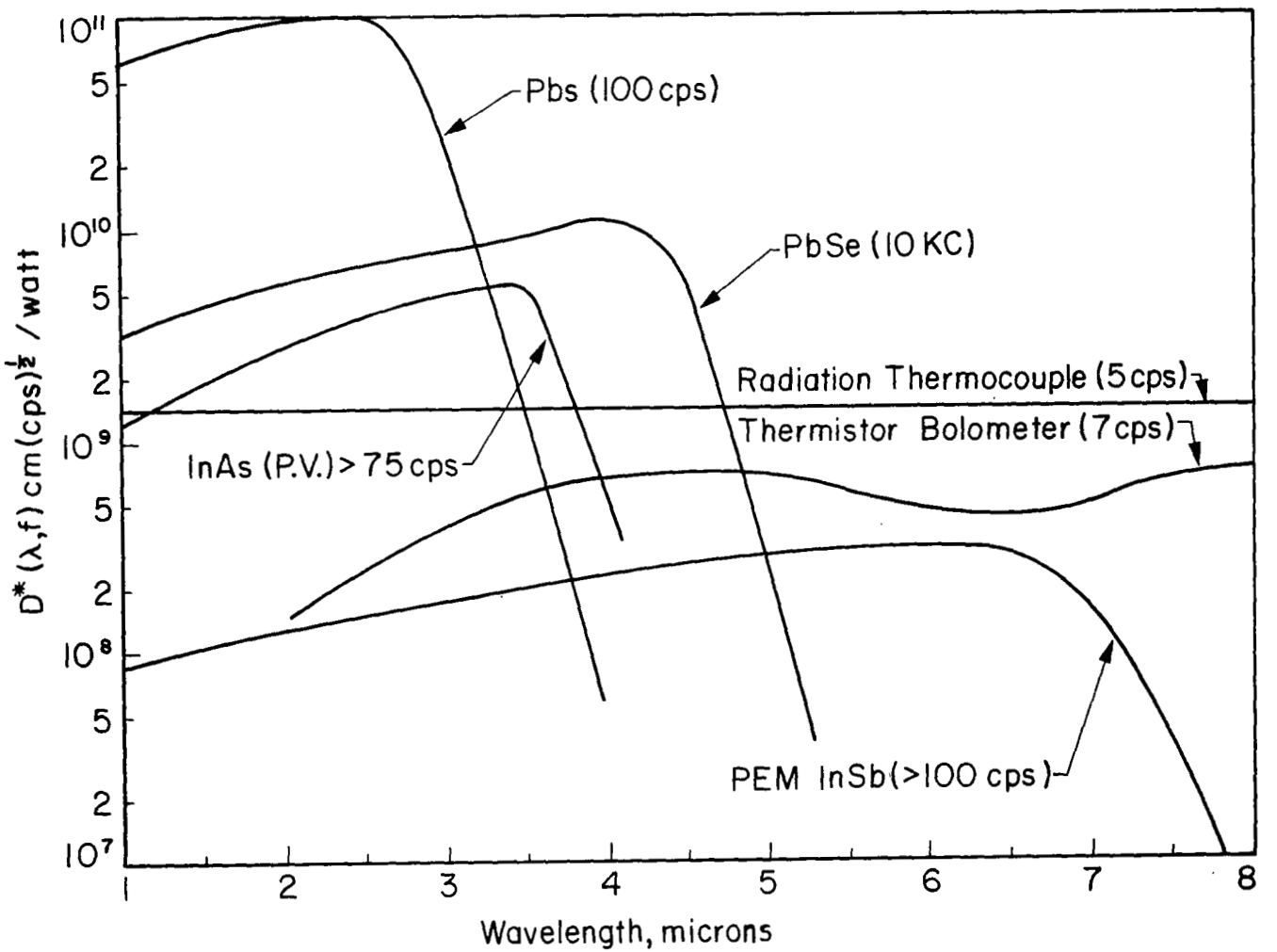

FIGURE 44. SPECTRAL DETECTIVITY COMPARISON FOR VARIOUS DETECTORS AT 298° K. (FROM JOHNSON)

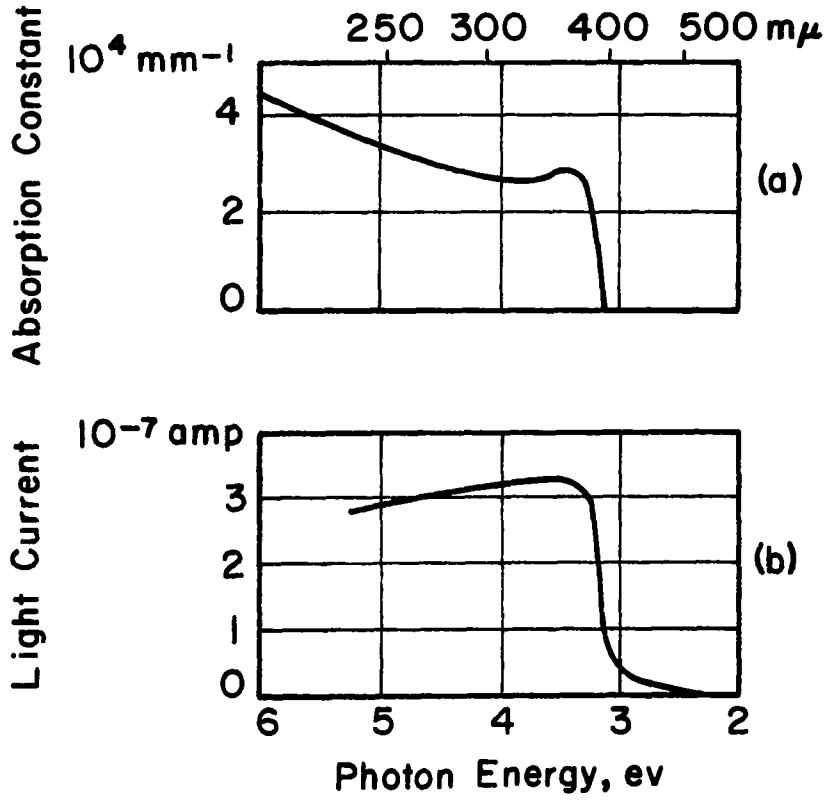

FIGURE 45. ABSORPTION AND PHOTOCONDUCTIVITY OF Zn O.

Stannic oxide (SnO_2) and (Zn, Mg) S Detectors

Very promising photoconductors have been made with pure crystals of stannic oxide, SnO_2, and solid solutions of magnesium sulfide in zinc sulfide[54]. Recent work has centered around the development of these materials for small-area (approximately 1 mm^2) devices sensitive in the 2000 to 3000 Å region. Single crystal SnO_2 has yielded a D* of 4.4×10^{12} cm cps $^{1/2}$/watt at room temperature for radiation at 2850 Å. The crystal was about 1 mm^2 and held in room atmosphere. Other measurement parameters are as follows: incident flux 1.9×10^{-9} watts, bias voltage 225V, signal 9.27×10^4 μV, noise 2.6 μV, NEP (1 cps) 1.8×10^{-14} watts, responsivity 5.0×10^7, modulation (chopping) frequency 25 cps, bandwidth 8 cps, load resistor 20 meg. Time constants on the order of 10^{-3} sec have been observed and found to depend on the crystal trapping effects. The relative response curve for the described detector is given in Figure 46. Slightly lower response devices have been made with thin films of SnO_2. The frequency response of the crystal detectors decreases as the chopping frequency increases. Samples that were exposed to chopped radiation in the intrinsic range along with unchopped longer wavelength radiation had the signal from the chopped radiation considerably increased. This enhancement effect supposedly results from the optical release of trapped carriers.

Simple zinc sulfide and zinc sulfide-magnesium sulfide (Zn-Mg)S detectors have also been tested. These devices show much the same properties as the SnO_2 detectors with only slightly lower values of D*. By using a binary mix as (Zn-Mg)S, the spectral response region may be shifted slightly by varying the concentration of MgS. A measurement similar to that on the SnO_2 resulted in the following data for ZnS: incident flux 3.1×10^{-7} watts, bias voltage 9V, signal 14.7 μV, noise 0.93 μV, NEP (1 cps) 7.0×10^{-9} watts, detectivity D* 1.9×10^7 cm cps $^{1/2}$/watt, responsivity 47 V/watt, and wavelength 2850 Å. For a (Zn,Mg)S crystal with 29.0 mole percent MgS the following was measured: incident flux 4.9×10^{-9} watts, bias voltage 150 V, signal 886 μV, noise 2.6 μV, NEP (1 cps) 5.0×10^{-12} watts, detectivity D* 1.8×10^{10} cm cps $^{1/2}$/watt, responsivity 1.8×10^5 V/watt.

Other materials

Another possible detector material is Al_2O_3 which has a band gap larger than 5 ev. However, no information

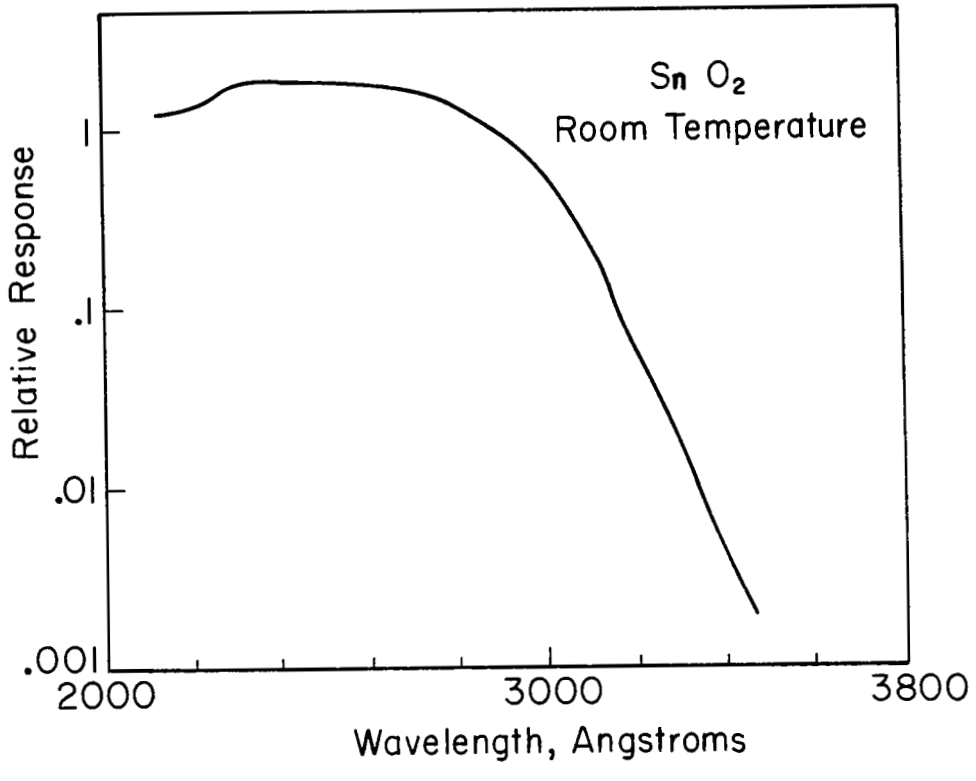

FIGURE 46. RELATIVE PHOTOCONDUCTIVE SPECTRAL RESPONSE CURVE FOR SnO_2. (FROM SCHULTZ AND HARTY)

has been found on the use of this material as a detector. It is expected that this material will show the same sharp photoconductivity peak as TiO_2.

Crystals of various materials having large band gaps are also possible UV photoconductors. Nakai and Teegarden showed the photoconductivity in RbI and KI crystals occurs in the 6 ev region[55]. Other work found the onset for direct photoionization at room temperature for KBr and KCl crystals to be 6.8 and 7.5 ev, respectively[56]. The photoconductive response curves for these crystals have a triple peak presumed due to (1) excitation by imperfections in the material at the longer wavelength (2) formation of excitons at middle wavelengths, and (3) direct photoionization in the undisturbed crystal by the shorter wavelength.

Application to Reentry Spectrophotometry

Although there has been some work done on photoconductors in the middle ultraviolet, no measurements have been made in the vacuum UV region. By extending the response curves of PbS it would appear that the quantum sensitivity should increase rapidly; however, the photon is absorbed nearer the surface and surface trapping may negate any conductive properties. SnO_2 and (Zn, Mg)S detectors also show potential as small-area devices which may be incorporated into an array. All of these devices appear to be only slightly effected by longer wavelength radiation.

To overcome the 1/f noise or drift, a chopper or light modulation device is usually required in the system. This means the introduction of a mechanical device into the instrument. There may also be some long term memory effect associated with particular photoconductors. Another parameter which may effect the detector performance is the helium environment that may be used to establish a radiation window. Helium surface absorption may vary the surface layer states which are important in high absorption coefficient materials. Also the high absorption may cause surface heating resulting in temperature drift.

The detectivity of photoconductive detectors is equal to that of ordinary photodiode types; however, measurements in the vacuum UV are required before any operating system can be contemplated. At present it does not seem feasible to use a photoconductive detector without a wavelength dispersion device such as a grating. From the work done on SnO_2, construction of a photoconductive thin film array seems possible.

Photoconductors have the advantage of a wide frequency bandwidth and rugged construction. A bias voltage must be applied to these detectors and readout can be accomplished with each detector element separately or in a combination state as with a scanistor. It is expected that photoconductive detectors can be used in the vacuum UV region, however, measurements must be made to determine their response. Due to the rapid change of photon energies in this region the response will probably not be uniform.

4. Photovoltaic Detectors

The photovoltaic effect is the generation of a potential difference between two portions of a device due to the absorption of radiation. Basically, the radiation excites electrons and holes in a photoconductor; however, due to the presence of a potential barrier and the subsequent movement of the minority carries a voltage is created. The barrier can be created by (1) an n to p junction in a semiconductor, (2) the junction of a metal and semiconductor, (3) contact of two semiconductors with different band gaps, and (4) the junction between the surface and volume conductivity of various materials. The generation of an electromotive force from the conversion of light energy was reported by E. Becquerel in 1839[57]. Since then complete descriptions of photocurrent processes have been given for materials as germanium and silicon[58].

When a pn junction is formed the conduction and valence bands come into contact and electrons from the n-type region, which has a larger concentration of electrons in the conduction band, flow into the p-type material. The n-material then acquires a positive charge because it now contains a number of ionized sites which are not balanced by an equal number of free electrons. The negative and positive sides of the junction are illustrated in Figure 47. The potential established is such that the net flow of carriers across the junction due to diffusion is almost zero since it is counterbalanced by the flow in the reverse direction due to the electric field at the junction. This barrier voltage V is given by

$$V = \frac{kT}{e} \ln \left(\frac{n_p}{n_n}\right)$$

where n_p and n_n are the densities of free electrons in the n and p materials.

Upon illumination of the detector, charge pairs are created and the minority carriers are drawn across the barrier to constitute a current flow in the reverse direction

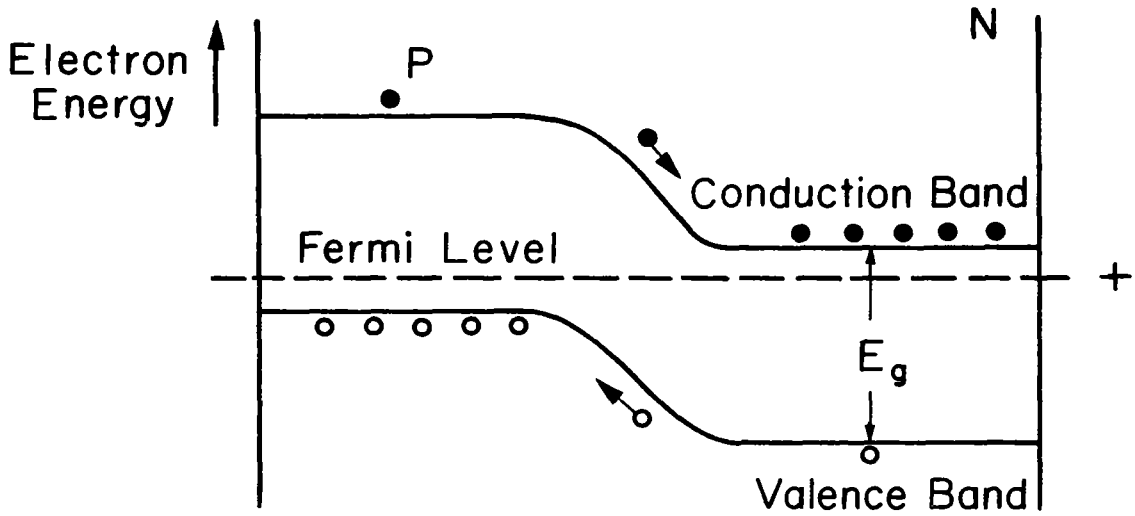

FIGURE 47. ENERGY LEVELS OF A pn JUNCTION.

of the barrier. When the junction is short circuited the current flow is observed. If the junction remains, open a voltage is built up to counterbalance the current flow. The maximum theortical voltage can equal the energy difference in the Fermi levels of the two regions before contact. For a junction device the photovoltage V_o is given by

$$V_o = \frac{kT}{e}\left[\ln\left(\frac{n'_p}{n'_n}\right) - \ln\left(\frac{n_p}{n_n}\right)\right]$$

where n_p and n_n are the dark concentrations of minority carriers and n'_p, n'_n the respective concentrations under illumination.

Since photovoltaic cells depend on the same charge generation mechanism and use the same materials as photoconductors, they have essentially the same spectral response and problem of temperature and fatigue drift. Also, the majority of cells have the junction deep under the surface and thereby are insensitive to short wavelength radiation because of the high absorptivity. The advantage of these devices is that they create their own output voltage or currents without the use of auxiliary circuitry.

Experimental Cells

It was found that certain cells produced photovoltages in excess of the band gap. For PbS (band gap 0.35 ev) cells, photovoltages of about 2 volts were measured. Other cells such as CdTe also generated photovoltages which were 100 to 1000 times that of the junction. This unexpected voltage was attributed to material stacking faults which created a large number of successive junctions[59].

Rutile (TiO_2), operating in a photovoltaic mode, was also investigated at the University of Michigan. However, the preferred operation was as a photoconductor with an external bias. Most photoconductors can be operated so that they generate photovoltages through selection of proper materials which will form a junction barrier.

Solar Cells

Solar cells are silicon pn junction devices used to convert the radiant energy from the sun into electric power. The cell usually consists of a thin slice of single crystal p-type silicon on which a layer of n-type material is formed by diffusion. The silicon cells have a response which

peaks at 8800 Å as shown in Figure 48. These cells are usually made as large as possible, a typical RCA type SL2205 cell has 0.4 x 0.8 in.^{2} area and a minimum efficiency of 10%. Unsuccessful attempts have been made to improve the energy conversion in the ultraviolet by employing phosphors[60].

Commercial Cells

Commercial cells were initially constructed with a cuprous oxide barrier layer. Later, a selenium layer cell, which has improved temperature stability over the initial cuprous oxide, was developed. The spectral response of Se cells (Figure 49) peaks at approximately 5600 Å. The high UV sensitive selenium cell has a much higher response than commercial silicon photocells in the 2000 to 5000 Å wavelength region; however, below 2000 Å the sensitivity decreases rapidly[61]. These cells also exhibit temporary fatigue depending on the intensity of the illumination. Temperature changes also cause output variations depending on the load resistance as shown in Figure 50[62].

VUV Detection

For use in the vacuum UV these photovoltaic detectors have the advantage of generating their own output or power. The output of a cell is approximately proportional to its area so miniature cells will yield lower outputs. Even for the most sensitive spectral region a 0.05 sq. in. cell can yield only 12 microamps. Once past the long wavelength edge of the vacuum UV, this output will fall off by at least a factor of 100 to 1000. Due to high absorption constants in the vacuum UV, a cell will become insensitive unless the junction region is almost at the surface. Commercial solar and selenium cells usually have the junction rather deep inside. Silicon surface barrier devices, which are discussed elsewhere, may have their junctions within hundreds of Angstroms from the surface. Photovoltaic detectors provide their own junction bias and consequently do not have the large junction potential which produces high efficiency and fast response.

Basically, the photovoltaic cell relies on the potential barrier to move the photon formed electron and hole thereby generating a potential or external current. Photoconductive cells or reversed bias detectors require an external emf to move the photo-created charge pairs. The advantage of the latter devices is that a much larger potential can be applied across the material. For basic reliability and

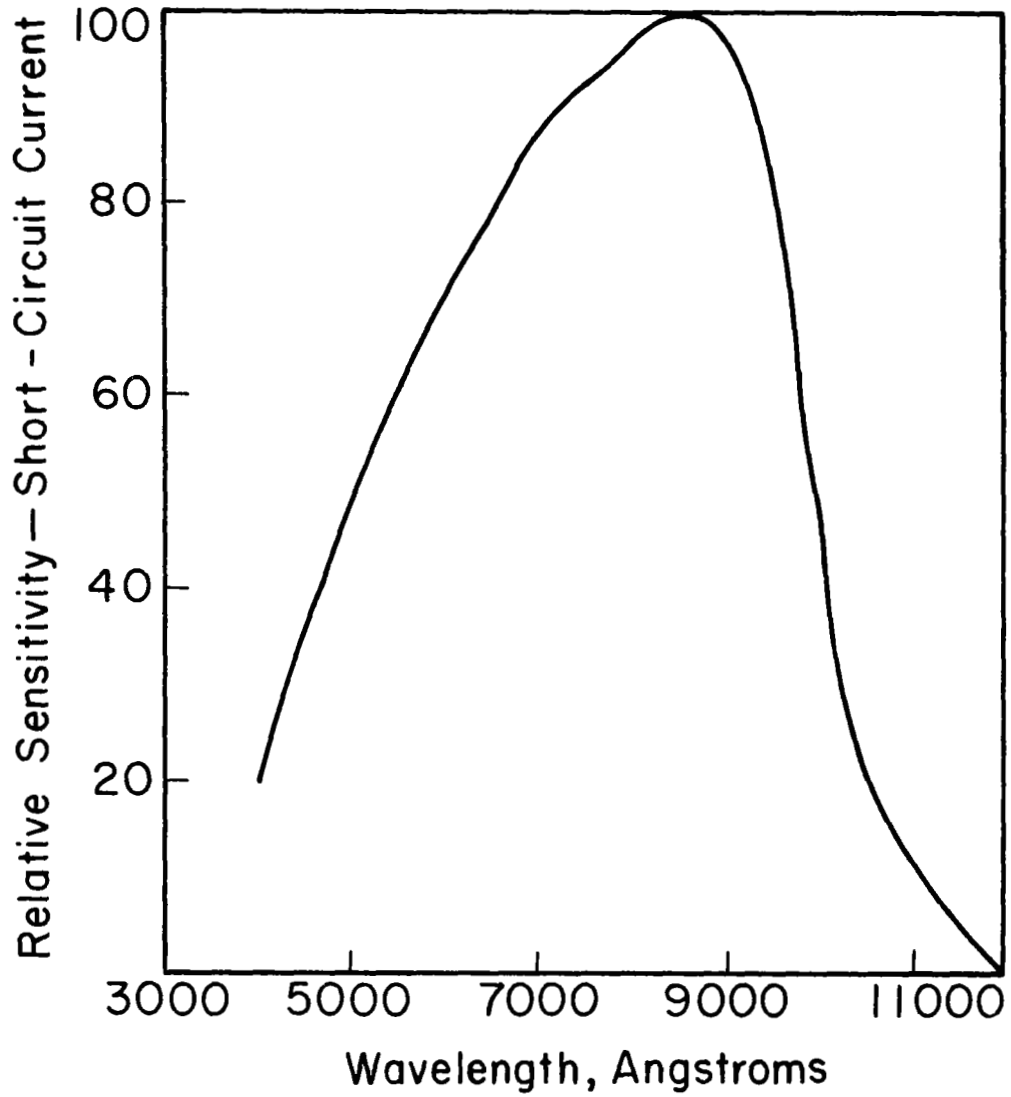

FIGURE 48. SPECTRAL RESPONSE OF A SILICON SOLAR CELL. (RCA MANUAL)

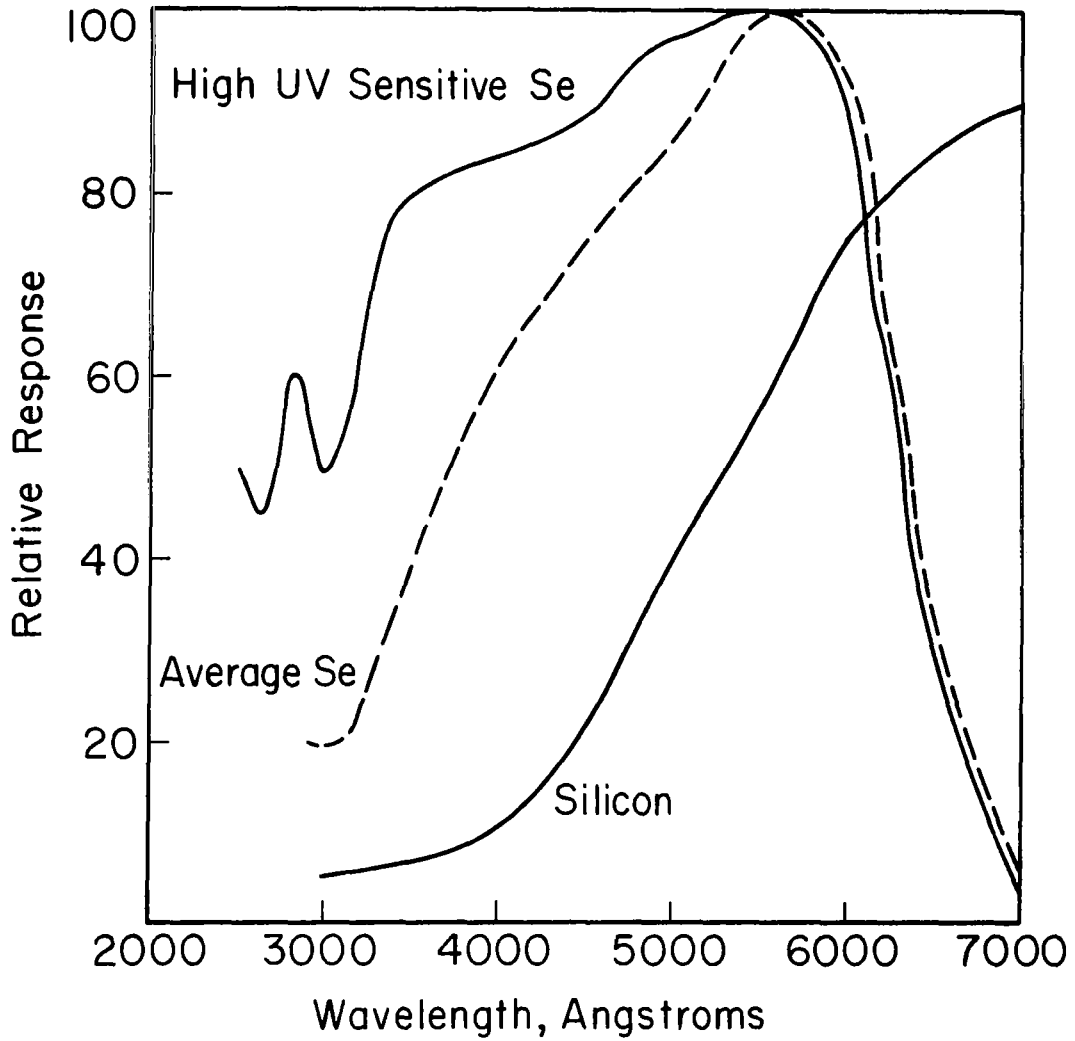

FIGURE 49. SPECTRAL RESPONSE OF SELENIUM PHOTOVOLTAIC CELLS. (FROM KOLLER)

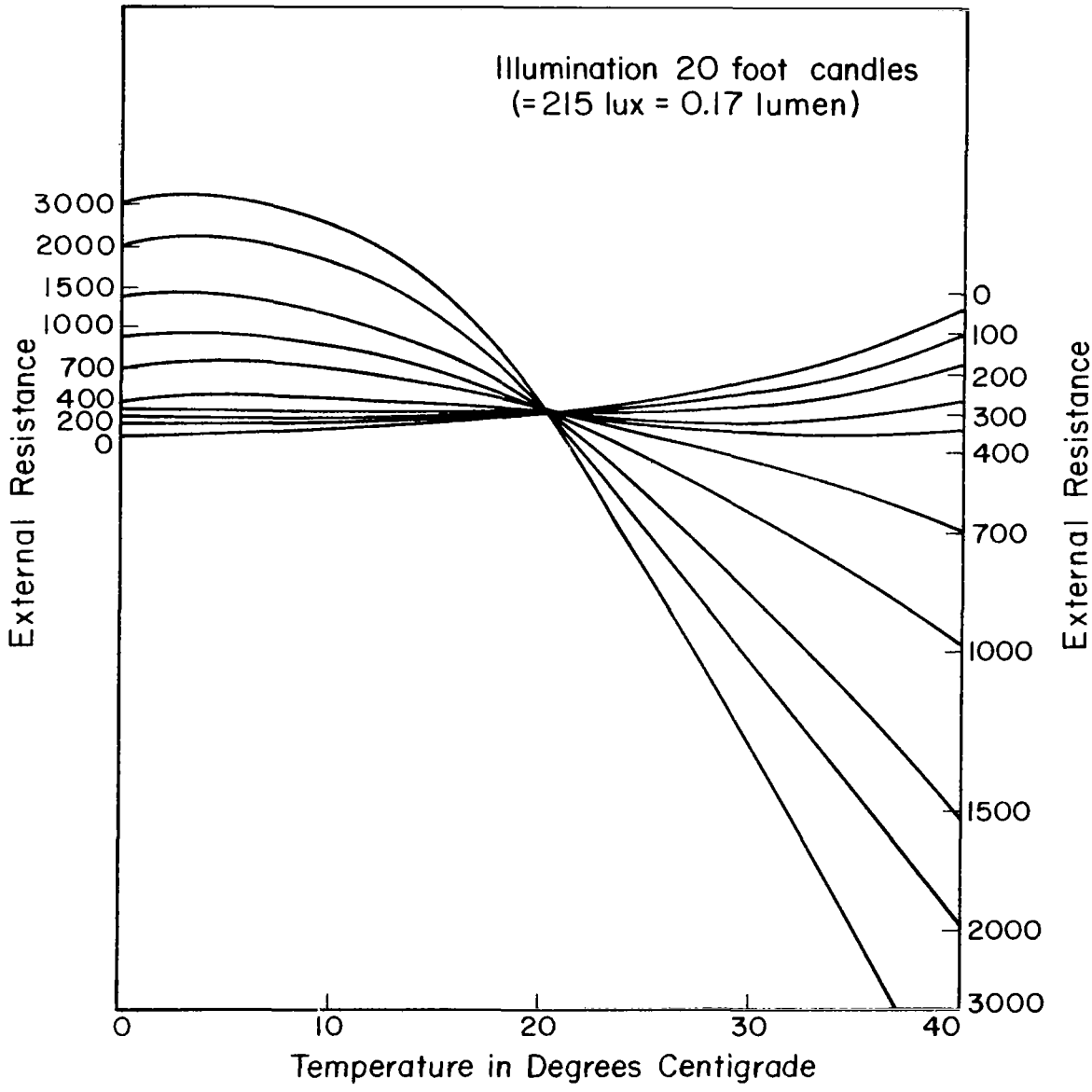

FIGURE 50. TEMPERATURE EFFECTS ON SELENIUM CELLS. (FROM ZWARYKIN)

stability a photoconductor should surpass a junction type device.

Photovoltaic cells have almost all of the problems associated with photoconductive devices except that the junction can be positioned normal to the entire surface. Photovoltaic cells also require additional processing to establish the pn junction. It appears that photovoltaic devices will always be second to photoconductive detectors in the realm of sensitivity and general use.

5. Reverse Biased Photodiodes

Two types of solid state semiconductor detectors have been studied as reverse-biased photodiodes. These are the diffused junction detectors and the surface barrier detectors. The diffused junction device is made by diffusing a shallow layer of a donor (or acceptor) material into high resistivity p-type (or n-type) semiconductor. The basic principle of operation of the surface barrier device is the same as for the p-n junction, but the rectifying junction in this case is between an evaporated metal layer (usually gold) and a high resistivity n-type semiconductor. Usually the semiconductor materials used are silicon or germanium for the better "state-of-the-art" detectors. Silicon by virtue of its higher band gap is a better choice between these two materials for use at higher temperatures. Other semiconductor materials which have been studied for use at higher temperature are silicon carbide and cadmium telluride. In the following section we will be primarily concerned with the silicon reverse-biased detector.

In these devices (see Figure 51) the sensitive volume is the depletion or space charge region formed about the junction or barrier by the application of a reverse voltage bias to the detector, i.e. positive voltage applied to the n-type region and negative to the p-type surface. The barrier depth, W(V), is given approximately by

$$W(V) = \left(\frac{\epsilon V}{2\pi q N}\right)^{1/2}$$

where

V = applied voltage

ϵ = dielectric constant (= 12 for silicon)

q = electronic charge

N = uncompensated impurity concentration in the bulk n-type silicon

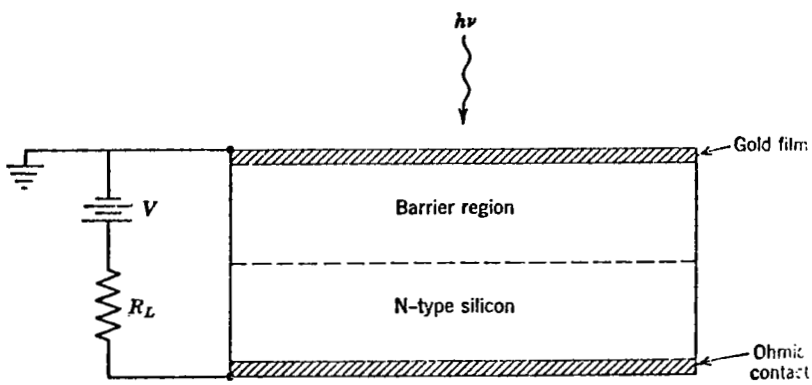

Silicon surface-barrier photodiode.

Figure 51. Reverse biased solid state photodiode.

The effective barrier capacitance of the photodiode is

$$C(v) = \frac{\epsilon A}{4\pi W(V)}$$

where A is the diode area. Typical detector capacitance is between 10 to 100 picofarads.

These devices have fast response times since they are limited only by the transit times of the photoproduced charge carriers across the barrier, and not by carrier recombination times across the gap. Thus, the long time constants generally associated with wide energy gap materials are avoided. The intrinsic collection time (T_c) of a reverse biased semiconductor junction is approximately given by

$$T_c = \frac{\epsilon \rho}{8} \times 10^{-11} \text{sec}$$

where ρ is the bulk conductivity in ohm cm. In practical applications this time is of the order of 10^{-9} to 10^{-8} sec. In connection with the response time considerations, it is important that the minority carrier lifetime be one to two orders of magnitude larger than the collection time in order to fully utilize the total charge produced by the absorbed radiation and obtain maximum output signals.

The p-n junction is a diode whose voltage-current characteristic depends on the bias direction and the magnitude of the bias. The modern theory of the p-n junction derives from Shockley[63]. The evolution of the theory is described by Moll[64]. According to Shockley, the current-voltage relationship in the simplest case of a low applied field, with steep concentration gradients in going from the n- to the p-type regions, is given by:

$$I = I_s \left[\exp (eV/kT) - 1\right]$$

where

$$I_s = \left[\frac{p_n D_h}{L_p} + \frac{n_p D_e}{L_n}\right] e$$

where L_n and L_p are the diffusion lengths of minority carrier electrons and holes in p- and n-type materials respectively, and D_e and D_h are the corresponding diffusion constants. The diffusion constants and length are related by the Einstein equation:

$$L = \sqrt{D\tau} \quad = \sqrt{(kT/e)\mu\tau}$$

where τ is the minority carrier lifetime and D is the diffusion coefficient for either electrons or holes as indicated by a subscript. In this treatment, the current of holes flowing in one side of the junction is the same as that flowing out the other, while the current of electrons is also equal at both surfaces of the junction, but moving, of course, in the opposite direction. The net current flow is then simply the sum of the hole and electron currents. One assumes further that charge carrier flow of electrons into the p region and holes into the n region (after passing through the junction) is essentially a diffusion process. That is, the n- and p-type regions are more highly conductive than the junction, and therefore, that practically all of the voltage drop is across the junction.

It is clear in the case of an applied voltage sufficiently large, that I is exponentially dependent on a positive voltage. When applied voltage is back biased or negative, as in the case of a detector, then the current flow approaches the saturation value I_s. The current flow is due entirely to the number of minority carriers able to cross the junction. It is now the electrons originating in the p material, within a diffusion length of the barrier L_n, and the holes in the n material within a diffusion length of the barrier L_p, which constitute the carriers for current flow. These carriers are created by the G-R (generation-recombination) process whereby electron-hole pairs are created in the lattice from phonon (thermal) interaction between atoms that make up the lattice. The saturation arises when all possible minority carriers from either side of the junction region are contributing to the current flow.

The treatment of the p-n junction as used for photodetection requires the inclusion of additional considerations, to the extent that the previous equation becomes:

$$I = I_s \left[\exp \quad (eV/BkT) - 1\right] + I_{sc} + G_{sh} V$$

where B is a constant, I_{sc} is the current induced by the background radiation and G_{sh} is the conductance in shunt with the diode[65,66]. Pruett describes in particular the case of the InSb photovoltaic detector, and shows the way in which the back biased diode current varies with infrared illumination. It is interesting to note that the development of such a detector (sensitive in the 3-5 micron region) was partly the result of

the need to increase the resistivity of the detector, to the point where its electrical noise exceeded the best preamplifier noise levels. This procedure insured that the limiting noise was with the detector, not with electronic components, and that maximum detectivity would be obtained.

Silicon Photodiode Detector

The present state of development of photodiode detectors is exemplified by the silicon photodiode[67]. This device is sensitive in the ultraviolet, visible and near infrared regions of the spectrum. The technical data for a silicon photodiode are given rather completely by Tuzzolino[68].

Spectral Response

Tuzzolino has measured the quantum efficiency, η, defined as the number of electron-hole pairs produced per absorbed photon, of a silicon photodiode for the vacuum ultraviolet wavelengths. These data are shown in Figure 52. The quantum efficiency is relatively flat, with values of η between 3 and 4, from about 1000 Å to 2000 Å. For photons below 1000 Å the quantum efficiency increases rapidly to a value of 15 at 580 Å (the lowest wavelength measured).

The sensitivity of a reverse biased silicon-gold surface barrier device is shown in Figure 53. Sensitivity, S, is defined as the number of electrons flowing in an external load resistor per photon incident on the photodiode. The reason for the lower values and the lower slope of this curve as compared to the quantum efficiency curve is the photon absorption in the gold film of nominal thickness of 100 Å. Those photons transmitted through the gold film are readily absorbed within the barrier region of the silicon which in this case was about 50 microns (a 6 volt bias was used).

Detectivity

In the case where these detectors may be used in conjunction with a pre-dispersive element or spectral filter system to obtain the wavelength selection, the sensitivity given in Figure 53 can be used for evaluation. Firstly, it is necessary to convert the spectral distribution of the expected radiant energy into units of photons per second. This is done for the case of the peak heating period (lifting trajectory, non-adiabatic case) as shown in Figure 54. The open circles on this figure are the values of photons per second per 50 Å band.

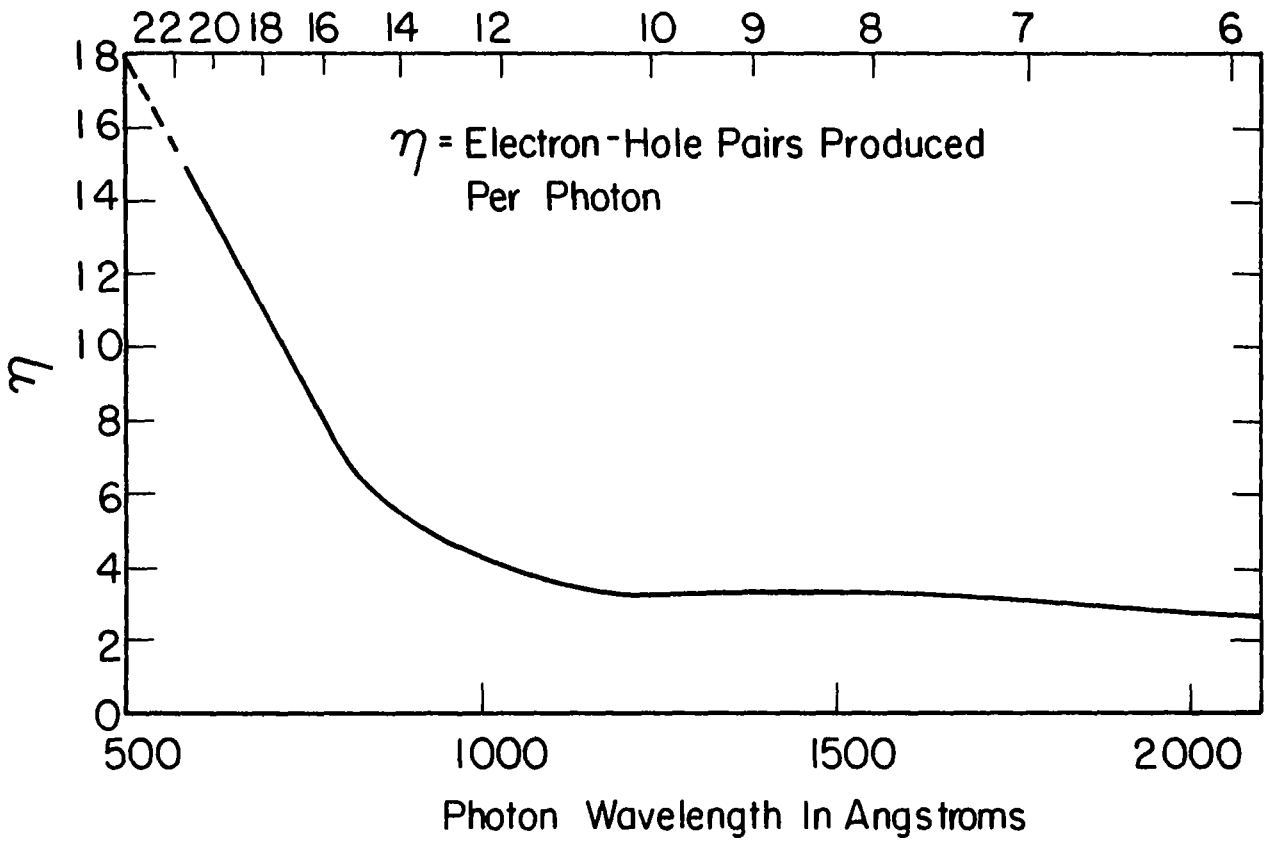

FIGURE 52. QUANTUM EFFICIENCY (η) OF SILICON. (FROM TUZZOLINO)

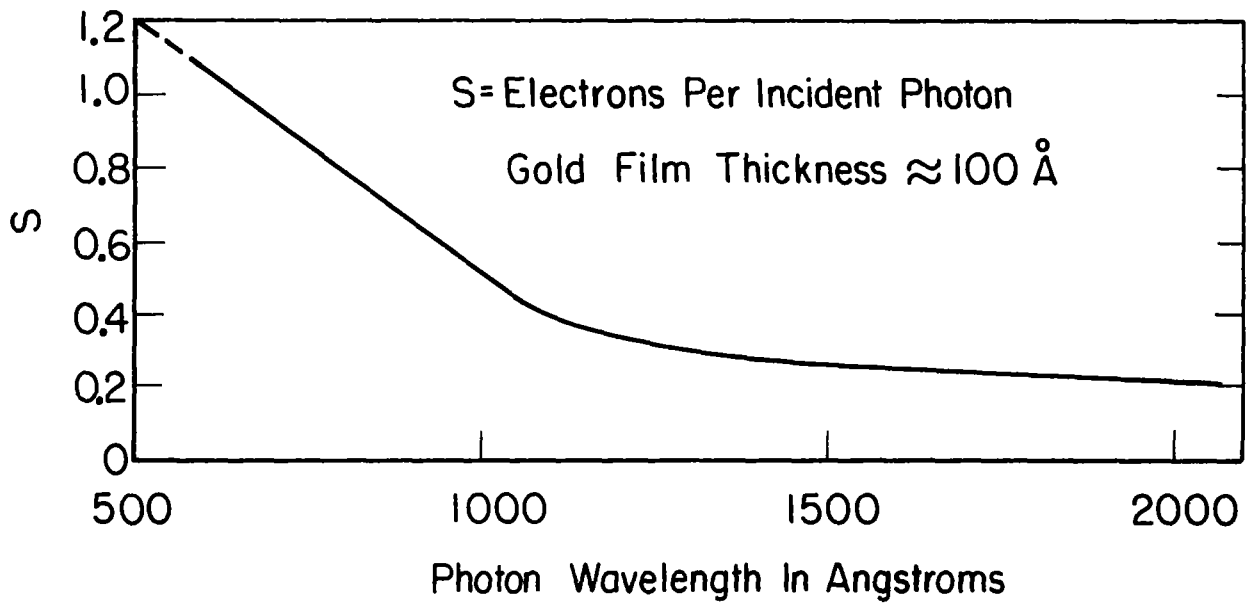

FIGURE 53. SPECTRAL SENSITIVITY OF SILICON PHOTODIODE.

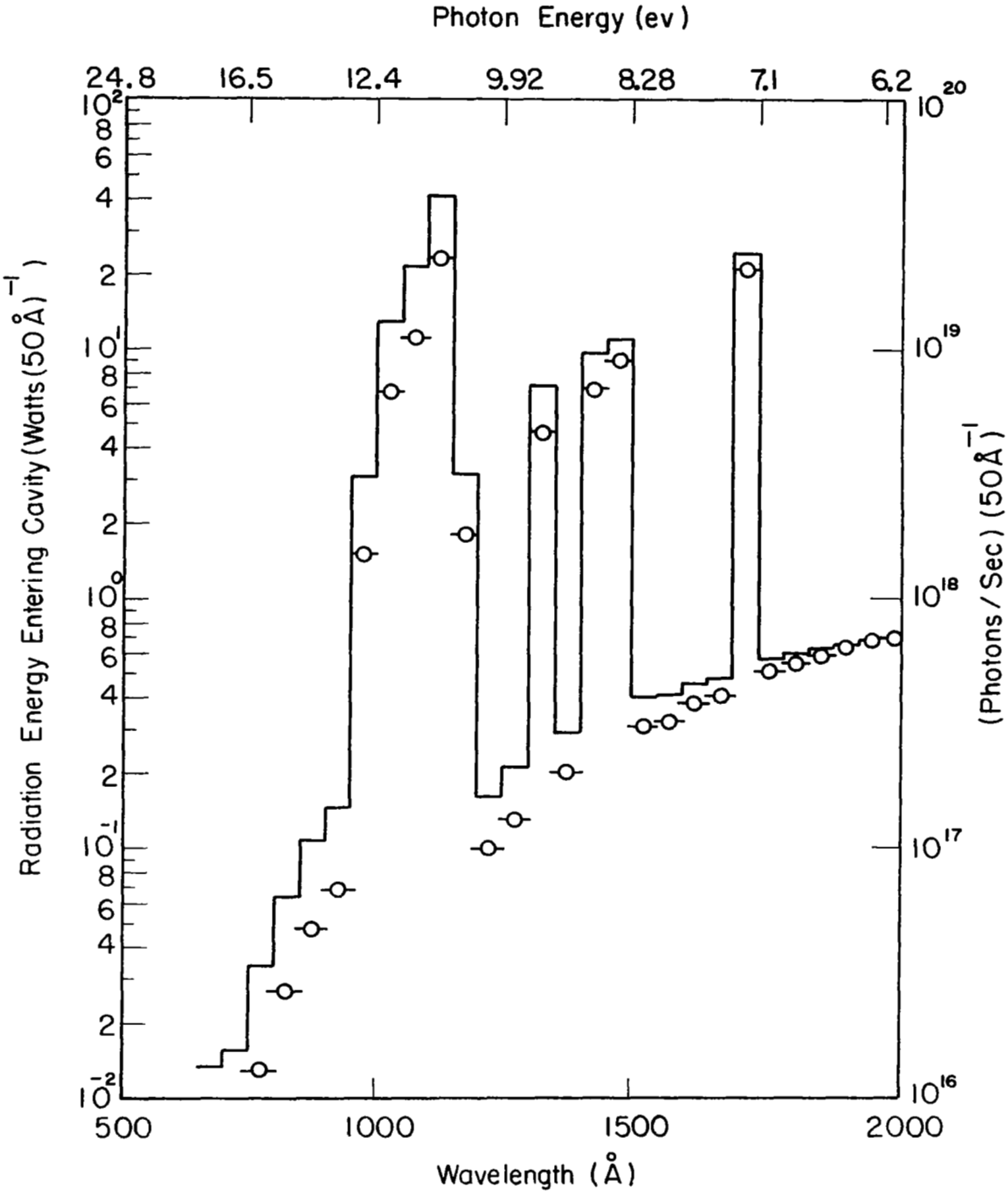

FIGURE 54. SPECTRAL DISTRIBUTION OF RADIANT ENERGY ENTERING CAVITY DURING PEAK HEATING PERIOD-LIFTING TRAJECTORY, NON-ADIABATIC CASE. CAVITY APERTURE 0.192 cm^2 (3/16 in. dia.)

For example, consider the region about 1250 Å where the peak intensity entering the cavity is about 10^{17} photons per second per band, and where the detector sensitivity is about 0.3 electrons per photon. Assuming that a grating system is used with an efficiency of one percent, the peak current signal in the detector load resistor is

$$I_L = 10^{17} \times 0.3 \times 10^{-2} \text{ electrons/sec}$$
$$= 3 \times 10^{14} \text{ electrons/sec}$$

Again referring to the data of Tuzzolino[68], the detector had a "dark current" of about 10^{-8} which is equivalent to 6×10^{10} electrons/sec. Thus the signal is about four orders of magnitude above the reverse bias dark current and simple low frequency techniques could be used for handling the signal. At 5 spectra/sec and 30 bands/spectra the detector time response is quite sufficient for the 150 measurements per second.

It is interesting to note that the detector sensitivity increases where the radiant energy spectral distribution decreases most rapidly, i.e. at wavelengths less than 1000 Å.

Temperature Dependence

The processes of the generation of charge carriers by the signal radiation and the subsequent collection of this charge signal will not be affected by nominal temperature changes in silicon. However, the reverse current or "dark" current, i.e. the steady current passed by the silicon detector in the absence of radiation with an applied reverse voltage bias, is temperature dependent. The temperature dependence of this reverse current for a typical gold-silicon surface barrier detector is shown in Figure 55[69]. For temperatures above room temperature the reverse current is seen to increase by about an order of magnitude for a 20°C temperature increase.

Such behavior must be considered since the reverse current directly limits the detectivity or "noise" properties of these detectors. However, the initial estimate of the expected high signal to dark current level indicates that one could use these detectors with a dispersive system with only modest temperature control necessary.

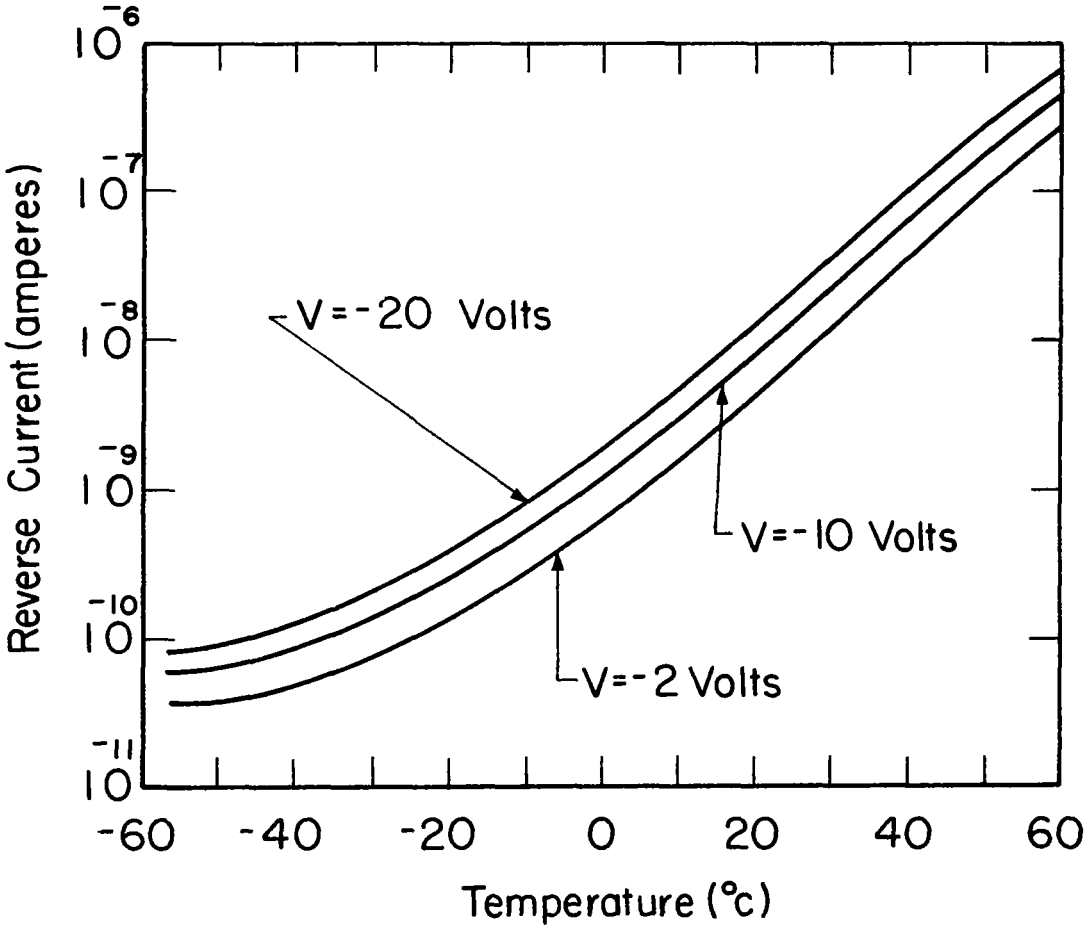

FIGURE 55. TEMPERATURE DEPENDENCE OF REVERSE CURRENT AT FIXED BIAS LEVELS FOR A TYPICAL GOLD-SILICON SURFACE-BARRIER DETECTOR. (FROM TAKAKI, etal.)

Silicon Photodiode with Wavelength Shifter (Phosphor)

The silicon surface barrier photodiode has also been tested in combination with a sodium salicylate phosphor as a wavelength shifter[68]. The spectral response of this combination is that of the excitation spectrum of the sodium salicylate, which has an essentially flat quantum efficiency over the wavelength region of interest. It was found that the absolute sensitivity value for this combination was about an order of magnitude less than that for the photodiode alone at 1250 Å. That is, a constant sensitivity of about 3×10^{-2} electrons per photon.

Since the silicon surface barrier detector has a good response to vacuum ultraviolet radiation there appears to be no advantage in the use of a phosphor wavelength shifter. For silicon detectors where there is an appreciable "dead-layer" of silicon, such as the Scanistor, which severely attenuates the ultraviolet, there would be an advantage in using a wavelength shifter to emit photons near the peak response of the device (usually in the red region about 8000 Å).

6. Wavelength Shifters

A wavelength shifter is a photoluminescent material (phosphor) which when excited by ultraviolet photons will luminesce or emit photons of a lower energy, i.e. at longer wavelengths usually in the visible region of the spectrum. Their obvious use is to present a useable light output, which one can either see or detect more readily, and is proportional to the intensity of the impinging ultraviolet light. The characteristics of interest in defining a phosphor are: 1) the emission spectrum; 2) the excitation spectrum; 3) the luminescence efficiency; 4) the effect of temperature on luminescence efficiency; 5) the decay time of the luminescence; and 6) the physical form of the phosphor.

Luminescent materials may be broadly typed into the categories of inorganic solids, organic solids, organic liquids, and gases. In general, the inorganic phosphors have better stabilities in physical form, in luminescence characteristics, and in luminescence efficiencies than the others. For those reasons we will be concerned primarily with the inorganic phosphors, although one must include the properties of sodium salicylate (the most commonly used wavelength shifter for vacuum ultraviolet detection) for comparison.

The inorganic phosphors are impurity activated luminescent materials usually in which atoms foreign to the host material are added in concentrations of tenths to several mole percent to form the "luminescent center". The phosphors are designated by host materials and impurity atoms in the following manner: ZnS:Cu means a zinc sulfide host material activated with a copper impurity. In some cases such as the $CaWO_4$ phosphor the material may be luminescent without the addition of foreign atoms. Presumably non-stoichiometry produces defects which serve as luminescence centers in such phosphors.

In the following section we will discuss the phosphor characteristics as they apply to this project's problem. Following that we shall list several phosphors which may be candidates for use in this application. Unfortunately not all the characteristics are known for some of the candidate phosphors.

Phosphor Characteristics

Emission Spectrum

Most phosphors emit broad bands of radiation with bandwidths at half maximum of hundreds of Angstroms. The luminescence emission spectra of sodium salicylate and ZnCdS:Ag (with a Zn to Cd ratio of 2 to 8) are shown in Figure 56. These curves are normalized at their peak emission. Also shown in the figure is the emission spectrum of YVO_4Eu. The emission from VYO_4:Eu is typical of the rare-earth activated vanadates and the yttrium oxide type phosphors which exhibit several relatively narrow emission bands.

More detailed information on the emission bands from yttrium vanadate phosphors, as measured by Ropp [70], is presented in Table 11. A variety of phosphors and the peaks of their emission spectra are listed in Table 12 in order of wavelength. This listing includes "blue" emitting phosphors which match the peak response of the common photocathodes and "red" emitting phosphors which would be better suited to the response of silicon devices.

Excitation Spectrum

In general the emission spectrum of a phosphor is independent of the wavelength or energy of the excitation photons. However, the efficiency of the photoluminescence

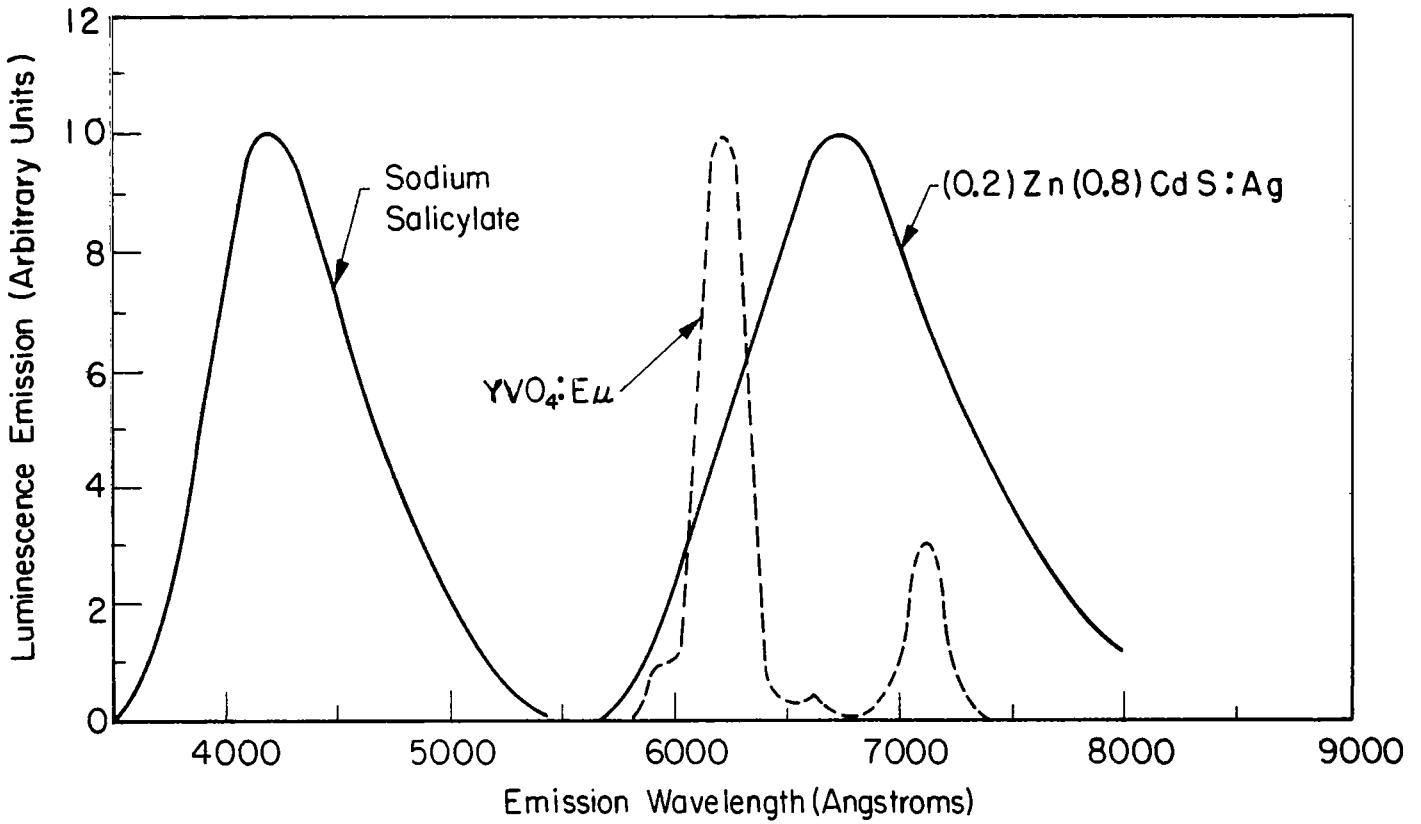

FIGURE 36. LUMINESCENCE EMISSION SPECTRA.

TABLE 11

LUMINESCENCE EMISSION BANDS FROM RARE-EARTH ACTIVATED VANADATE PHOSPHORS EXCITED AT 3200 Å*

Phosphor	Band Peak (Å)	Percent of Total Emission
YVO_4: Sm	5650	10.5
	6060	35.0
	6500	42.3
	7220	12.2
YVO_4: Dy	4790	36.9
	5780	59.5
	6700	3.6
YVO_4: Eu	5960	8.9
	6220	66.8
	6540	2.4
	7130	21.9

* Data from R. C. Ropp, J. Opt. Soc. Am. 57, 1240, 1967.

TABLE 12

LUMINESCENCE EMISSION BANDS FROM VARIOUS PHOSPHORS

Phosphor	Peak of Emission Spectra (Å)
KBr:Tl	3500
$BaSi_3O_5$:Pb	3700
$CaSiO_3$:Pb:Mn	3700-6100
KI:Tl	4100
$CaMgSiO_3$:Ti	4100
Sodium Salicylate	4200
CsI:Tl	4200-5700
$CaWO_4$	4320
ZnS:Ag	4480
$CaWO_4$Pb	4580
ZnO:(Zn)	5080
Zn_2SiO_4:Mn	5240
Y_2O_3:Eμ	6110
$Zn_3(PO_4)_2$:Mn	6200
(0.2)Zn (0.8)CdS:Ag	6750
$Mg_6As_2O_{11}$:Mn	6800
CdS:Ag	7300
CdS:Cu	8200

process is in most instances a function of the excitation wavelength. The curve of luminescence efficiency vs. excitation wavelength is the so-called excitation spectrum of the phosphor. Most of the excitation spectra measurements have been limited to a low wavelength cutoff at about 2000 Å. Thus there is not a complete set of data for all of the phosphors of interest in the detection of vacuum ultraviolet.

One of the early studies on phosphors excited by vacuum ultraviolet was Watanabe and Inn[71]. That work resulted in the discovery of the very useful properties of sodium salicylate as a wavelength shifter for ultraviolet detection. This phosphor has essentially a constant luminescent quantum efficiency for excitation photons from 500 Å up to 3500 Å. Recent studies[72] on sodium salicylate have shown that its efficiency drops by about 15% for wavelengths less than 600 Å. As mentioned previously, sodium salicylate is the most commonly used wavelength shifter for laboratory ultraviolet detection in conjunction with phototubes; and most of the data on other phosphors are obtained and presented relative to a sodium salicylate sample.

Thurnau[73] and Conklin[74] studied the response of several inorganic, oxygen-dominated host phosphors (such as phosphates, silicates and tungstates) excited in the wavelength range of 275 Å to 1715 Å. Later Bril[75] studied most of the above same phosphors with excitation wavelengths greater than 1800 Å. Sussmann, et al.,[76] have obtained the excitation spectra of ZnS:Ag and ZnS:Cu from 500 Å to 3000 Å, and Gergely, et al.,[77] amongst others, have reported excitation spectra of zinc sulfide type phosphors for the mid-ultraviolet range.

As an illustration of the varied excitation spectra observed for different phosphors, the excitation spectra of sodium salicylate, $CaWO_4$, and ZnS:Ag are shown in Figure 57. In contrast to the "flat" response of sodium salicylate, the other excitation threshold at long wavelength, and then the response decreases to a minimum value at shorter wavelengths. Most phosphors reported in the above references exhibit a strong increase in quantum efficiency at the very short wavelengths (1000 Å) as illustrated by the $CaWO_4$ and ZnS:Ag in Figure 57. These two phosphors are typical in the general behavior of their excitation curves to the majority of the inorganic phosphors; the differences being in the positions of the long wavelength excitation threshold.

Several alkali halide phosphors have also been studied with vacuum ultraviolet excitation by Ilmas[78].

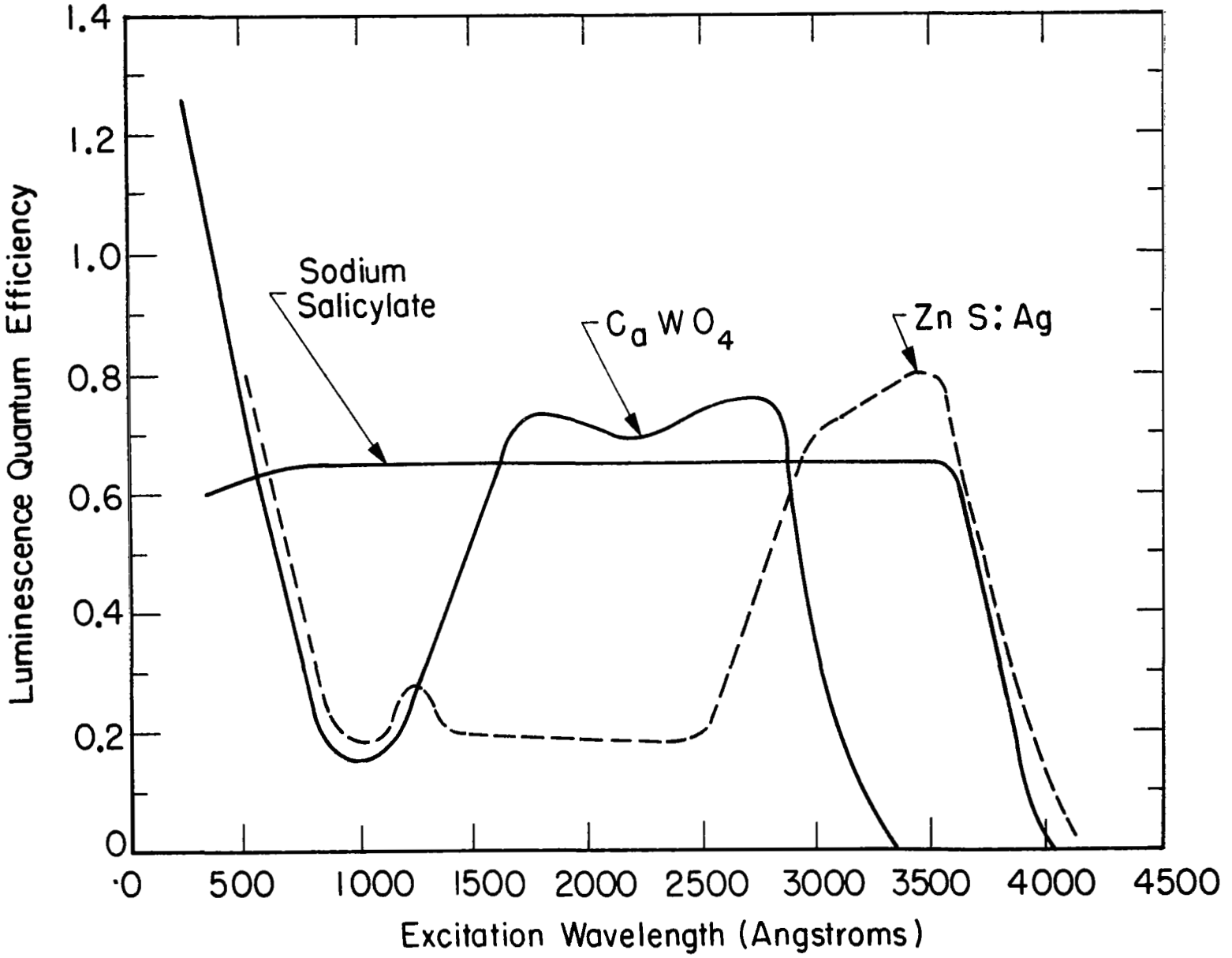

FIGURE 57. LUMINESCENCE EXCITATION SPECTRA.

Except for the fact that these phosphors exhibited two distinct excitation peaks in the longer wavelength region, their excitation spectra followed that typified above.

Luminescence Efficiency

The absolute luminescence quantum efficiency, η, i.e. the ratio of the number of luminescence emission photons emitted to the number of excitation photons, is rarely measured for individual phosphors. As mentioned above, most phosphor efficiency measurements are presented relative to sodium salicylate. Thus it is desirable to know the absolute efficiency of sodium salicylate as accurately as possible. Samson[79] lists luminescence efficiency values for sodium salicylate as determined by seven different groups. The efficiencies varied from 25% to 99% with the majority of the values between 60% and 65%. Samson concludes that a value of 65% for the absolute quantum efficiency of sodium salicylate for excitation radiation between 400 Å and 3400 Å appears to be a suitable compromise.

The spread in the reported values may be due to the different experimental techniques used, to different sample thicknesses, and to different sample handling and aging. It has been demonstrated that sodium salicylate coatings do change in efficiency with age. In fact, the observed decreases in efficiency are not always independent of excitation wavelength. Thus some observers have noted a decrease in the efficiency curve for decreasing wavelengths between 1600 Å and 1000 Å.

The luminescence quantum efficiencies of various phosphors at room temperature for 500 Å, 1000 Å, 2000 Å and 3000 Å excitation are listed in Table 13. In this table the phosphors are ordered the same as in Table 12, i.e. the "blue" emitting phosphors are listed first and the emission wavelengths increase from top to bottom. These values were taken from the various references given previously and the accuracies of the values are probably about $\pm$ 50%. In general, one can expect a good inorganic phosphor to have a quantum efficiency greater than 20% between 2000 Å and 1000 Å, and an increasing efficiency as the excitation decreases below 1000 Å.

It is sometimes convenient to use energy conversion efficiency units. For this efficiency the phosphor emission wavelength is needed. Since the photon energies are inversely proportional to their wavelengths, the energy conversion efficiency, ϵ, is

$$\epsilon(\lambda) = \eta(\lambda) \times \lambda exc./\lambda em.$$

TABLE 13

LUMINESCENCE QUANTUM EFFICIENCIES FOR VARIOUS PHOSPHORS AT SELECTED EXCITATION WAVELENGTHS

PHOSPHOR	QUANTUM EFFICIENCY IN PERCENT AT GIVEN EXCITATION WAVELENGTH*			
	500 Å	1000 Å	2000 Å	3000 Å
KBr:Tl	75	25	50	—
$CaSiO_3$:Pb,Mn	—	50	55	5
KI:Tl	50	20	20	—
$CaMgSiO_3$:Ti	50	15	35	—
Sodium Salicylate	65	65	65	65
$CaWO_4$	70	15	70	35
ZnS:Ag	80	20	20	70
ZnO:(Zn)	100	35	10	—
Zn_2SiO_4:Mn	—	70	70	25
Y_2O_3:Eμ	—	—	40	—
$Zn_3(PO_4)_2$:Mn	40	20	15	—
ZnCdS:Ag	—	—	—	20
$Mg_6As_2O_{11}$:Mn	—	—	40	75
YVO_4:Eμ	—	—	70	80

*All values are for phosphors at room temperature.

where

η (λ) = luminescence quantum efficiency at excitation wavelength

λexc. = excitation wavelength

λem. = luminescence emission wavelength.

These efficiency values are always less, of course, than the quantum efficiencies since the emission wavelengths are greater than the excitation wavelengths.

Temperature Effects

The luminescence efficiency decreases as the phosphor temperature is increased. This effect is called temperature quenching. Curves of luminescence efficiency versus temperature are usually very constant in efficiency value for a broad temperature range around room temperature and below. At elevated temperatures the efficiency curve decreases, sometimes with a very rapid slope and in other cases with a rather small slope. A common way of classifying the temperature quenching is to use the temperature at which the efficiency has decreased to one-half of its maximum value. These temperatures are listed in Table 14 for a variety of phosphors. The majority of these data was obtained from Reference [75].

A most interesting phosphor is the yttrium oxide (Y_2O_3:Eu) which retains its luminescence efficiency at temperatures appreciably above those of the other phosphors. In fact, luminescence has been observed from this phosphor at temperatures up to 800°C.

Decay Time

The response time of a phosphor detector is equivalent to the luminescence decay time. In most phosphors the decay of the emission intensity after cessation of the excitation is a negative exponential function with time, i.e. $I/I_o = \exp(-t/t')$, where t' is the decay time which is equivalent to the time at which the intensity has decreased to 1/e. The inorganic phosphors of interest in this report have decay times of milliseconds or less. These response times are quite adequate for this spectrometry application.

TABLE 14

LUMINESCENCE QUENCHING TEMPERATURES FOR VARIOUS PHOSPHORS

PHOSPHOR	TEMPERATURE AT WHICH LUMINESCENCE EFFICIENCY DECREASES TO 1/2 (max.)
Y_2O_3:Eu	> 650 °C
$CaSiO_3$:Pb,Mn	> 400
$Mg_6As_2O_{11}$:Mn	360
Zn_2SiO_4:Mn	350
$BaSi_2O_5$:Pb	280
ZnCdS:Cu	270
$Ca_3(PO_4)_2$:Tl	250
Zn_2SiO_4:Mn	240
ZnS:Cu	225
$CaWO_4$	210
ZnS:Ag	140
$MgWO_4$	110

Phosphor Screen Properties

In addition to the luminescent characteristics discussed above there are several physical properties of phosphors which must be considered in their application. The physical form of the phosphor and the optical index of refraction are two properties of interest.

All phosphors are available as powders and several of the inorganic phosphors are readily prepared as large transparent single crystals. Since the absorption depth of vacuum ultraviolet photons is on the order of microns there is no advantage in thick single crystals. Deposited thin layers or films of phosphor prepared by vacuum deposition, evaporation or sputtering techniques could be useful. The most commonly used inorganic phosphor sample geometry is a thin screen of powder settled from a liquid suspension. The organic sodium salicylate screens are usually made by precipitation from a methyl alchohol solution.

When using the phosphor in a transmission type geometry, i.e. where the final detector is on the side of the phosphor opposite the incident radiation, the screen thickness is an important parameter. The scattering and absorption of the emitted light in the powder screen will reduce the output intensity and will decrease the spatial resolution of the screen. In Figure 58 the luminescence output from the back side of a sodium salicylate screen is shown as a function of phosphor thickness[79]. The sharp rise in output at the low thicknesses is a function of the absorption of the incident radiation in the phosphor. The slow fall of intensity as the phosphor thickness is increased is due to the scattering and absorption losses of the emitted light. A sodium salicylate thickness of 1 to 2 mg/cm^2 is optimum for use in the vacuum ultraviolet. Thurnau[73] found that mass thicknesses of 5 to 12 mg/cm^2 were optimum for the inorganic phosphors. Since the densities of the inorganic phosphors are factors larger than the sodium salicylate, the linear optimum phosphor thicknesses are similarly about 10 to 20 microns.

Luminescence emission is isotropic so the phosphor geometry and index of refraction affect the useable light output from a screen surface. These effects can be calculated for ideal polished, optically transparent rectangular prisms or spheres[80]. For irregular powder screens, however, precise calculations are impossible. In practice one can expect about 20% to 40% of the luminescence emission to be useable.

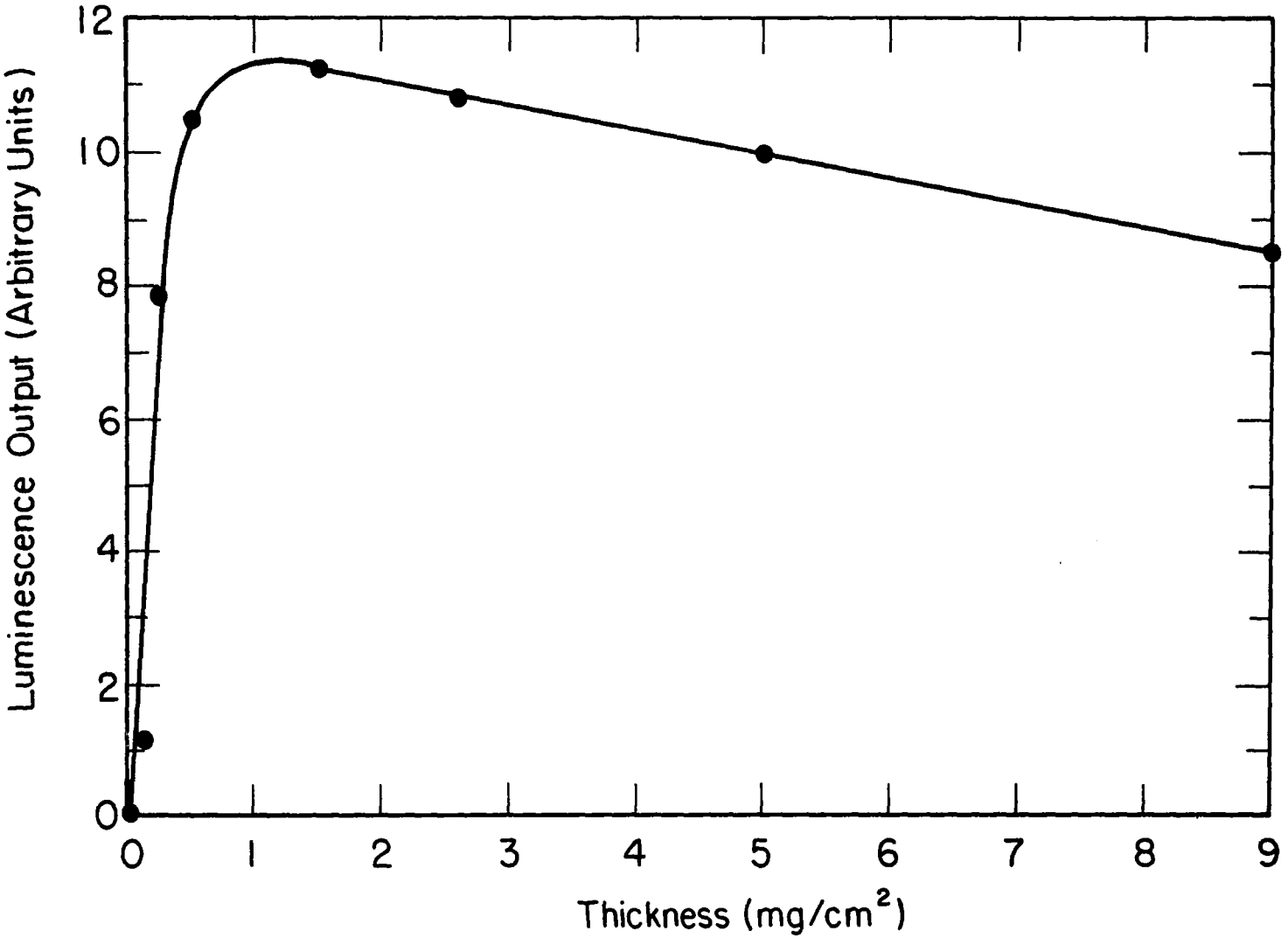

FIGURE 58. RESPONSE VERSUS THICKNESS OF SODIUM SALICYLATE LAYER EXCITED AT 1200 Å. (FROM SAMSON)

For example, taking the experimental results reported by Tuzzolino on the sensitivity to 1216 Å radiation of a silicon photodiode with and without a sodium salicylate screen we can estimate this geometry factor. He found that the photon sensitivity with the phosphor layer was 0.18 of that for a bare silicon detector. It can be shown from Tuzzolino's reported sensitivities at 1216 Å and 4358 Å (near the emission peak of sodium salicylate) that his silicon-gold photodiode had the same sensitivity per photon at these two wavelengths. Thus if we use a quantum efficiency of 0.65 for luminescence in the sodium salicylate, the geometry output factor of the screen is 0.18/0.65 = 0.28, or 28%.

B. Flux Detection with Energy Discrimination

1. Photoelectric Cathode with Retardation Grid Analyzer

A retarding potential analyzer is a device for analyzing the energy distribution of charged particles, usually electrons. The electrons are forced to travel against an electric field between two grids and the number passing the second grid is measured as a function of the retarding potential. By plotting this number against the retarding potential, and taking the derivative, the energy distribution of the particles is obtained. This device may be used to analyze the photoelectrons emitted by a surface subjected to ultraviolet irradiation. Since this electron energy distribution is a function of the wavelength of the light, the device can be used for spectral discrimination.

Hitherto the retarding potential analyzer appears to have been used only for very broad discrimination; it is well suited to the suppression of response of radiation above 1000 Å, thus preventing the interference of the strong Lyman-α radiation at 1216 Å [81]. Hinteregger et al[82] have also used the device to obtain better spectral selectivity, bandwidths of about 200 Å.

The basic concept employs a photocathode, analyzer and collector. There is an advantage in adding a multiplier because the collector becomes the first dynode[83]. Two kinds of analyzers have been reported in the literature, planar and spherical. The early work was carried out with planar analyzers: a grid in a plane parallel to the emitter establishes a retarding field perpendicular to the emitter surface. With

the planar analyzer the retarding field affects only the component of electron velocity normal to the cathode surface, so that differentiation of the current-voltage-distribution curve (CVD) yields only the "normal" energy distribution of the photoelectrons. In the second type of analyzer, the cathode is very small and is placed at the center of spherical grids: in this type of device the retarding field is nearly radial so that it affects the total velocity of the photoelectrons. By its nature the ideal spherical retarding potential analyzer (RPA) requires a point cathode. This is a practical disadvantage since radiation fluxes in the XUV are generally very small. The much larger signals attainable with a planar analyzer have caused this to be used more frequently than the spherical analyzer.

Since the RPA detects electrons, it is very important to suppress or remove stray charged particles in its vicinity. These particles may come from the gas cap in the reentry experiment, or may be generated photoelectrically by the intense UV radiation entering the instrument cavity. Problems of this kind have been encountered by Hinteregger et. al.,[82] who obtained environmental pick-up, and by Heroux et. al.[83] who found that careful design was required to minimize the detection of photoelectrons from stray UV radiation.

Figure 59 shows the arrangement of a planar RPA, with multiplier. This device monitors electrons emitted from the side of the photocathode facing the incident radiation. This does not have to be the case, with a thin film photocathodes radiation is transmitted through the cathode and electrons are emitted both sides (such a system is described by Heroux et.at.[83]) in which case additional light trapping is required.

Figure 60 shows a schematic diagram of a spherical RPA. A collimator is used before the photocathode and the electron multiplier is at right angles, both these precautions are necessary to minimize the number of stray electrons. The field grid is kept at cathode potential to minimize changes in the electric field at the cathode surface. The radiation transmitted by the cathode passes through a hole in the first dynode, and is eliminated.

CVD's for both planar and spherical RPA's are shown in Figure 61 to 64 (taken from Heroux et. al.[83]). Since the spherical RPA gives CVD's with more structure, and curves which are more distinct, it is to be expected that the best spectral resolution would be obtained with this, but no quantitative results have been reported. The greater spectral discrimination of the spherical RPA is exhibited qualitatively

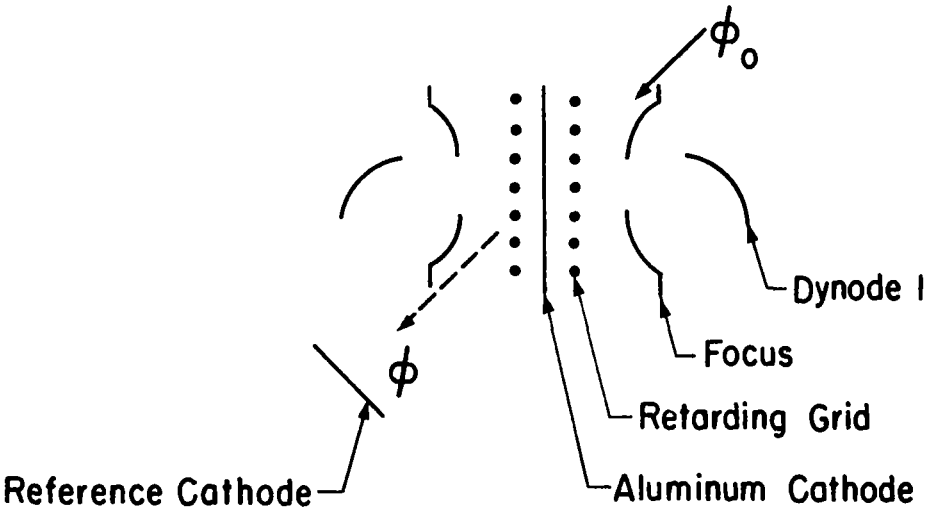

FIGURE 59. SCHEMATIC OF PLANAR RETARDING POTENTIAL ANALYZER FOR USE WITH THIN FILM CATHODES. Φ_0 REPRESENTS THE FLUX INCIDENT ON THE CATHODE AND Φ THE FLUX TRANSMITTED BY THE CATHODE.

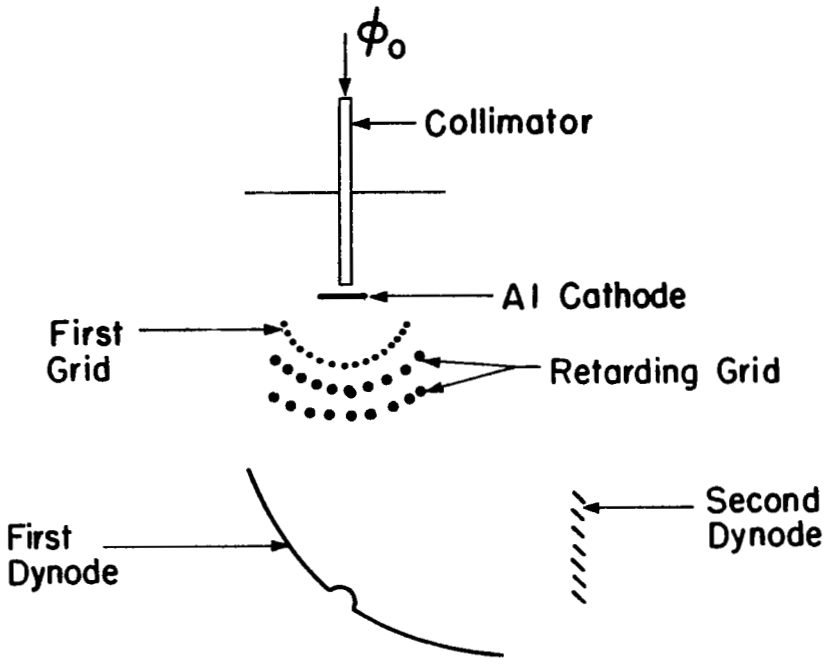

FIGURE 60. SCHEMATIC OF SPHERICAL RETARDING POTENTIAL ANALYZER, Φ_0 REPRESENTS THE FLUX INCIDENT ON THE CATHODE.

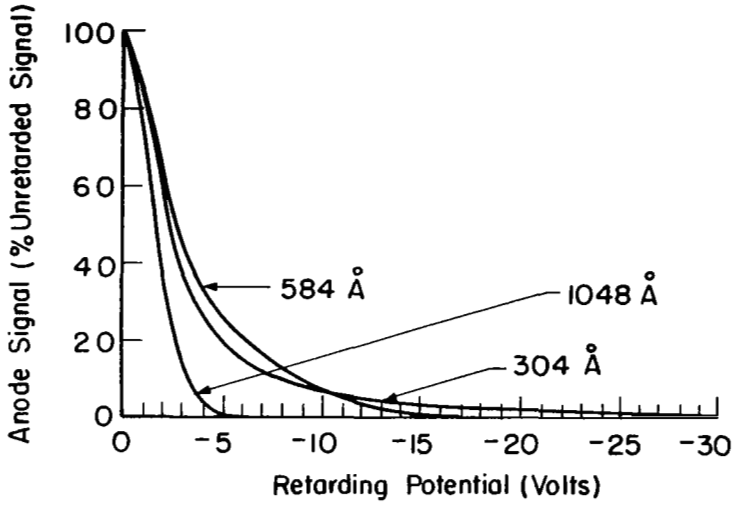

FIGURE 61. NORMALIZED CVD'S FROM PLANAR ANALYZER WITH ALUMINUM CATHODE, 1200 Å THICK.

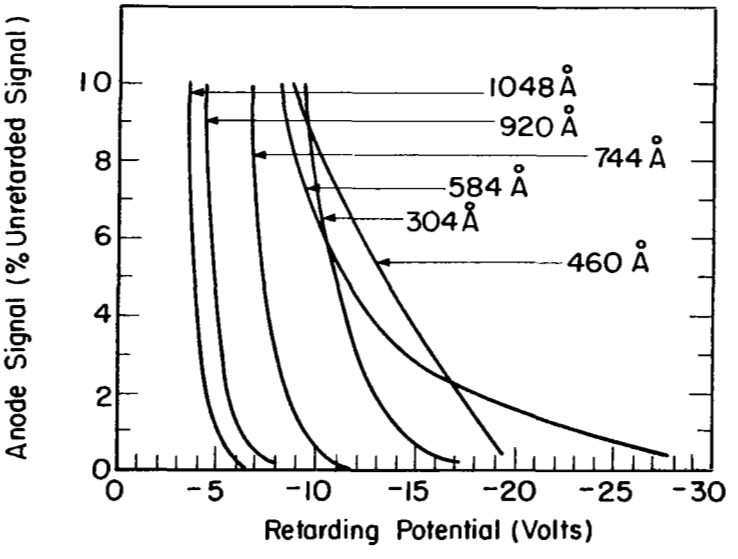

FIGURE 62. HIGH ENERGY PORTION OF NORMALIZED CVD'S FROM PLANAR ANALYZER WITH AN ALUMINUM CATHODE PLOTTED ON AN EXPANDED ORDINATE SCALE.

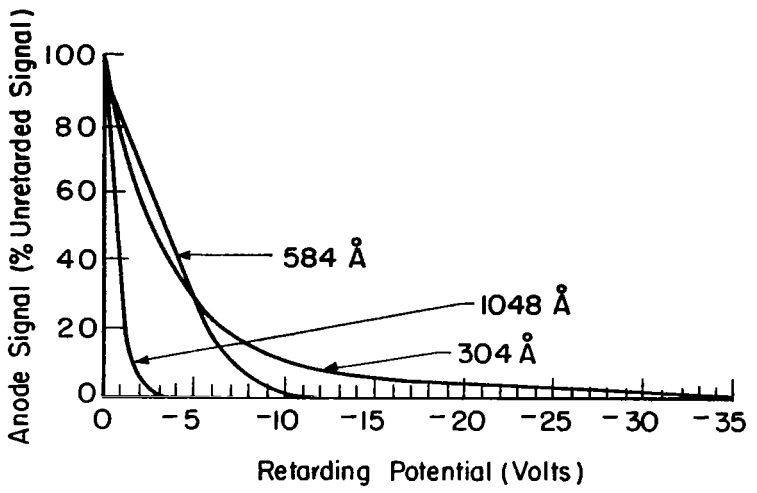

FIGURE 63. NORMALIZED CVD'S FROM SPHERICAL ANALYZER WITH ALUMINUM CATHODE, 3000 Å THICK.

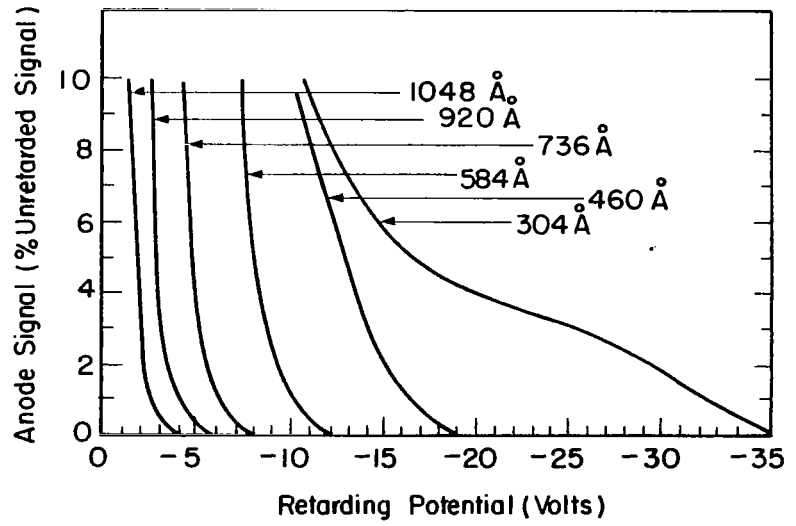

FIGURE 64. HIGH ENERGY PORTION OF NORMALIZED CVD'S FROM SPHERICAL ANALYZER WITH AN ALUMINUM CATHODE PLOTTED ON AN EXPANDED ORDINATE SCALE.

by comparing Tables 15 and 16. Heroux et. al. have demonstrated that the spherical RPA is more efficient at detecting photoelectrons below about 600 Å.

WAVELENGTH DISCRIMINATION

Only qualitative information is available in the papers of Hinteregger and his co-workers. It is a fact that monochromatic radiation, incident on a surface, generates heteroenergetic electrons. It is also a fact that the energy distribution of these electrons depends on the wavelength of the radiation. The problem now is to obtain the spectral energy distribution, given one such curve. The procedure adopted by Hinteregger et. al. was as follows. They treated the radiation as if it were emitted at several discrete wavelengths (584, 749, 1060, 1216 and over 2000 Å). The high voltage tail of the CVD obtained from their rocket flight was due to the radiation of lowest wavelength. Hence the contribution from this wavelength was subtracted out by matching the high voltage tail of the CVD for 584 Å to the experimental curve. Then each wavelength was subtracted out in the same way, proceeding from shorter to longer wavelengths. The CVD for radiation over 2000 Å was obtained by laboratory measurements using a high pressure xenon arc. In this manner a rather crude spectral energy distribution was obtained. This technique is really valid only when the radiation is monochromatic and the legitimate defense in their case was that no other measurement had been made. It is unlikely that a similar argument will be satisfactory here, so that more accurate methods are required. The methods used by Hinteregger et. al. could involve very large errors if strong lines are present which are not monitored specifically, .. e.g. neglection of Lyman-α at 1216 Å changed the result considerably. Furthermore, the effective band pass was not clearly defined.

An analytical approach to the problem is as follows. First consider n spectral groups, where n is made as large as necessary. With each group there is a radiation flux $f(\lambda_i)\ \Delta\lambda_i$. At each wavelength there is a particular quantum efficiency $Q(\lambda_i)$ and CVD, $R(\lambda_i, V_i)$. If rear emission is considered then there is also the transmittance of the material to be included, and this is wavelength dependent. Front emission only will be considered here since this is simpler. Assembling all these factors one obtains the current, as a function of wavelength and retarding potential

$$i(\lambda_i, V_j) = R(\lambda_i, V_j)\ Q(\lambda_i)\ f(\lambda_i)\ \Delta\lambda_i. \qquad (1)$$

TABLE 15. ALUMINUM CATHODE, 1200 Å THICK, IN PLANAR DETECTOR. ANODE SIGNAL (EXPRESSED IN PERCENTAGE OF SATURATION SIGNAL) FOR PARTICULAR VALUES OF RETARDING VOLTAGE V, AND FOR ILLUMINATION OF THE CATHODE WITH SEVERAL MONOCHROMATIC WAVELENGTHS. THE DATA ARE VALID FOR BOTH FRONT AND REAR SURFACE PHOTOELECTRONS.

Retarding Voltage (V)	Wavelength (photon energy)					
	1048 Å (11.8eV)	920 Å (13.5eV)	744 Å (16.7eV)	584 Å (21.2eV)	460 Å (26.9eV)	304 Å (40.7eV)
0	100	100	100	100	100	100
-1	74	80	89	85.5	90	85
-2	40	50	67.5	64	74.5	60
-3	14	24	47.5	45.5	55	38
-4	3.6	10.5	32	33	37	26
-5	1.0	3.9	21	26	23.5	19
-6	0.2	1.1	13	21	18	15
-7	0	0.5	5.8	16.5	14	12
-8	—	0.2	2.9	12.8	11	9.5
-9	—	0	1.2	10	9.3	7.5
-10	—	—	0.5	6.8	8.0	6.2
-12	—	—	0	3.0	5.9	4.4
-14	—	—	—	1.0	4.3	3.2
-16	—	—	—	0.4	2.8	2.4
-18	—	—	—	0.1	1.4	2.0
-20	—	—	—	0	0.1	1.5
-22	—	—	—	—	0	1.2
-24	—	—	—	—	—	0.9
-26	—	—	—	—	—	0.6
-28	—	—	—	—	—	0.4
-30	—	—	—	—	—	0.1
-32	—	—	—	—	—	0

TABLE 16. ALUMINUM CATHODE, 3000 Å THICK, IN SPHERICAL DETECTOR. ANODE SIGNAL (EXPRESSED IN PERCENTAGE OF SATURATION SIGNAL) FOR PARTICULAR VALUES OF RETARDING VOLTAGE V, AND FOR ILLUMINATION OF THE CATHODE WITH SEVERAL MONOCHROMATIC WAVELENGTHS.

Retarding Voltage (V)	Wavelength (photon energy)					
	1048 Å (11.8eV)	920 Å (13.5eV)	736 Å (16.8eV)	584 Å (21.2eV)	460 Å (26.9eV)	304 Å (40.7eV)
0	100	100	100	100	100	100
-1	36.5	47	66.5	78.6	75	76
-2	6.1	16	41.5	64.7	54.2	58
-3	1.1	3.9	24	52.7	40	45.5
-4	0.55	1.0	11.5	41	30.5	36.2
-5	0.31	0.3	3.75	28.7	24.1	29.4
-6	0.15	0	1.2	18.6	20	24
-7	0.03	—	0.31	10.8	16.6	18.6
-8	0	—	0.06	5.0	13.8	15.7
-9	—	—	0	2.35	11.7	13.0
-10	—	—	—	1.03	10.2	11.2
-12	—	—	—	0.076	6.25	8.18
-14	—	—	—	0	3.19	6.37
-16	—	—	—	—	1.21	5.2
-18	—	—	—	—	0.23	4.43
-20	—	—	—	—	0	3.92
-22	—	—	—	—	—	3.60
-24	—	—	—	—	—	3.22
-26	—	—	—	—	—	2.80
-28	—	—	—	—	—	2.35
-30	—	—	—	—	—	1.79
-32	—	—	—	—	—	1.08
-34	—	—	—	—	—	0.51
-36	—	—	—	—	—	0.11
-38	—	—	—	—	—	0

This expression is very similar to that given by Heroux et. al.[84] The data obtained from the RPA constitute

$$I(V_j) = \sum_{i=1}^{n} i(\lambda_i, V_j) \qquad (2)$$

The $R(\lambda_i, V_j)$ are measured in the laboratory during preflight calibration of the instrument, and the $Q(\lambda_i)$ are laboratory values for the photocathode used. Theoretically one might consider the $\Delta\lambda_i$ to be given by the distance between adjacent λ_i; assuming this, and that the wavelength interval is maintained constant, the suffix 'i' can be dropped.

From (1) and (2)

$$\begin{bmatrix} I_1 \\ I_2 \\ I_3 \\ \vdots \\ I_m \end{bmatrix} = \begin{bmatrix} R_{11} & R_{12} & \cdots & R_{1n} \\ R_{21} & R_{22} & \cdots & \\ \vdots & \vdots & & \vdots \\ R_{m1} & \cdots & & R_{mn} \end{bmatrix} \begin{bmatrix} F_1 \\ F_2 \\ \vdots \\ F_n \end{bmatrix} \Delta\lambda \qquad (3)$$

$$\text{or } \underline{I} = \underline{\underline{R}}\,\underline{F}\,\Delta\lambda \qquad (4)$$

$$\text{hence } \underline{F}\,\Delta\lambda = \underline{\underline{R}}^{-1}\,\underline{T} \qquad (5)$$

where $f(\lambda_i)\,Q(\lambda_i)$ has been written as $F(\lambda_i)$ for convenience. In the above equations 'm' constitutes the number of retarding voltages used in the measurements. Thus, in principle, it is only necessary to have CVD's for each wavelength interval in order to obtain the flux distribution $f(\lambda_i)$. The presence of

very intense spectral lines can be taken into account by introducing additional CVD's, remembering to add the same number of equations to (3), (4) and (5) since m = n is required for solution.

The feasibility of using equation (5) for determining the spectral flux distribution depends on accuracy. The more equations there are the greater the similarity between adjacent CVD's, and there comes a point where the differences are of the order of the experimental errors. The CVD's can probably be determined to high accuracy, simply by combining a large number of measurements, since this is a laboratory calibration. The measurement of $I(V_j)$ presents a greater problem: this measurement can be made once only and during the time the radiation flux is changing. Thus the change of radiation flux that takes place during one voltage scan constitutes an ultimate limitation, which may be translated into spectral resolution. The voltage scan rate is set primarily by the photon flux since a certain minimum number of counts is required to maintain accuracy. Thus this technique does require that the radiation flux be constant, in time, during the period of a single voltage scan.

For large numbers of photons, the probability of photon arrival is given by the Poisson distribution

$$P(x - \bar{x}) = \frac{1}{\sigma\sqrt{2\pi}} \quad e^{-x^2/2\sigma^2} \tag{6}$$

where this expression gives the probability of the deviation $(x - \bar{x})$ from the mean $\bar{x}$ and σ is the standard deviation. For the Poisson distribution $\sigma^2 = \bar{x}$. This expression can be used to give the probability that the total number of counts deviate by a certain amount from the expected mean, as a function of counting time, or number of pulses. If the required accuracy is set at $(\sigma/\bar{x}) = \pm 1\%$, this gives $(1/\bar{x})^{1/2} = \pm 10^{-2}$ or $\bar{x} = 10^4$, i.e. there must be 10^4 counts or more in order to achieve an accuracy of $\pm$ 1%. This figure can be used for examining the system -- better spectral resolution in general requires higher accuracy; with a digital system the accuracy should be limited by the number of counts only, without any contribution from other parts of the data handling system. When used with the estimated radiation flux levels the minimum period of a scan is obtained. This can be related to changing radiation conditions.

The question as to how great a spectral resolution can be obtained has to be considered in terms of the averages taken and the errors involved. Strictly speaking, the CVD's obtained in the laboratory apply for monochromatic radiation. When any one CVD is applied in a wavelength interval, say the 50 Å sought in the present study, then there is an inherent uncertainty due to the possibility that all the photons may lie at one or other wavelength extreme of the interval taken. Thus, if one desires an error no larger than $\pm$ q%, then the CVD's for the two ends of the interval must not differ by more than 2q%. If the radiation is fairly evenly distributed in the wavelength interval, this restriction does not apply. A conflicting requirement is the need for a large variation in CVD's with wavelength in order to separate out the different wavelength contributions; this is obviously necessary since the matrix $\underline{R}$ has no inverse $\underline{R}^{-1}$ unless the determinant $|R| \neq 0$, which it would be if any two CVD's were the same. The practical matter of how different the CVD's have to be, in order to achieve a desired spectral resolution, is dependent on the errors in the measurements.

Assume total fractional differences in radiation flux of q_2 are to be distinguished. Then

$$\left| \frac{F_{i+1} - F_i}{F_i} \right| \geq q_2 \tag{7}$$

where

$$q_2 \geq \frac{\delta F_i}{F_i} = \frac{1}{F_i} \sum_{j=1}^{n} \delta \left(R_{ij}^{-1} I_j \right) \tag{8}$$

Here δ signifies error. This relation can be expanded as

$$q_2 \sum_{j=1}^{n} R_{ij}^{-1} I_j \geq \sum_{j=1}^{n} \left| R_{ij}^{-1} I_j \right| \left[\left(\frac{\delta R_{ij}^{-1}}{R_{ij}} \right)^2 + \left(\frac{\delta I_j}{I_j} \right)^2 \right]^{1/2} \tag{9}$$

where the errors are now taken as standard deviations. If the fractional errors in R_{ij}^{-1} are assumed independent of j, then,

since

$$\sum_{j=1}^{n} R_{ij}^{-1} I_j \leq \sum_{j=1}^{n} \left| R_{ij}^{-1} I_j \right| \tag{10}$$

therefore an upper limit to the required accuracy is given by

$$q_2^2 \geq \left(\frac{\delta R_{ij}^{-1}}{R_{ij}} \right)^2 + \left(\frac{\delta I_j}{I_j} \right)^2 \tag{11}$$

for all j. Hence, if the errors in R_{ij}^{-1} and I_j are comparable, each must be less than $(q_2/\sqrt{2})$. Since R_{ij}^{-1} is given by

$$R_{ij}^{-1} = \frac{R_{ji}}{|R|} \tag{12}$$

where $|R|$ is an n x n determinant, it is seen that δR_{ij}^{-1} depends strongly on n. Clearly it is advantageous to make n small.

PROPERTIES OF PHOTOCATHODE MATERIALS

The photocathode one would use depends on the wavelength range of interest. It was seen earlier that there is a significant difference between the volume and surface photoelectric effect, in terms of quantum efficiency. Thus a material such as tungsten has a very low quantum efficiency down to about 1400 Å, at which point the volume photoelectric effect begins and a sharp rise is found. It was shown that one really required two different photocathode materials to cover the range 500 to 2000 Å. The same arguments apply in the present case.

Current-voltage distributions would have to be measured for any particular photocathode (these would, of course, have to be measured for a particular RPA before use). Published data are available for a few materials including tungsten [81], aluminum[83], copper and silver[84]; a few others, not all of them suitable for the XUV, are given by Weissler[85].

The quantum yields of copper and silver show steep rises between 1 and 2 eV photon energy (1.24 and 0.62μ respectively). Although these show a good response over the whole wavelength range of interest here, the long wavelength sensitivity rules out such photocathodes; there is a more stringent requirement for a RPA than for a spectrograph. It is possible that a photocathode such as gold would provide the best results since this material is sensitive over the whole range of interest and falls off shortly above 2000 Å. Electron energy distributions for this material are given by Weissler for three photon energies.

APPLICATION TO REENTRY EXPERIMENT

Providing a sufficient number of retarding potentials are utilized, and the measurements and calibration are performed with sufficient accuracy, there seems to be no reason why this device could not be used in the proposed experiment. The number of retarding potentials must be at least equal to the number of wavelength intervals. If it is possible to make more measurements this will allow

i) later re-working of the results to take into account such features as line structure and continuum edges and

ii) a more accurate CVD curve to be drawn for the experimental data - i.e. one might trade measurement accuracy for number of measuring points.

This method has a much greater chance of success if filters are used. One of these would be LiF; thus, of the whole photon energy range 6.2 - 25 eV., the range 12 - 25 eV would be excluded from one set of measurements, thereby improving the accuracy of determinations for wavelengths both above and below this cut-off wavelength. Another obvious filter would be fused quartz, of the variety which cuts off at around 2000 Å. The radiation from wavelengths longer than this is not required, but it will be detected if the photocathode responds up to 2000 Å, as cut-offs are not that sharp. Thus it is necessary to allow for the photoelectrons liberated by this long wavelength radiation. It is also necessary, of course, to allow for a small radiation flux at wavelengths shorter than 500 Å. As a result of these "end fluxes" it will be necessary to extend the wavelength range a little, since the radiation fluxes

deduced for the last two or three wavelength intervals will probably be rather inaccurate.

Another important limitation is the accuracy and reproducibility of the retarding voltages. Also there is the requirement that the radiation remain constant during the scan period. Unlike sequential scanning of detectors arranged around a conventional disperser, the radiation flux deduced at all wavelengths depends on each part of the record during the scan. It has been shown that the necessary photon counts are of the order of 10^4 per channel. From the previous reentry calculations the integrated flux is 0.91×10^{19} photons sec^{-1} in the wavelength range 500 - 2000 Å. The total number of counts to be recorded is 30×10^4, so that the time per scan would seem to depend on factors other than the radiation flux. This could be used to advantage, increasing the counts to 10^5 or 10^6 and so relaxing the counting accuracy required.

In a practical situation there would be the choice of using several instruments, with fixed filters, or one instrument with variable filters. In a non-steady, reentry type experiment it would probably be essential to use several instruments with fixed filters. There are two reasons for this, since

i) for wavelengths below 1050 Å there can be no window. Hence it will be necessary to use a narrow orifice with some differential pumping.

ii) If measurements with different filters are to be inter-compared, in order to simplify the analysis of non-filtered operation, then it is essential that the same radiation flux be viewed in each case. For reentry measurements this cannot be done without making the measurements simultaneously.

The minimum number of analyzers would then be two, with one of these operating in a windowless condition. The scans would be simultaneous, so that only one voltage supply and scanning mechanism would be required.

The device can probably be made to perform as required. Devices which have been described in the literature are not suitable, they have not been used for resolutions of the kind required, nor have they been used at such long

wavelengths. The research effort required to make such a device for the reentry experiment would be considerable (several man years) and unforeseen problems may exist. Further "analysis studies" could be profitable carried out.

2. Reverse Biased Diode as a Photon Counter

Referring to the quantum efficiency curve for silicon it appears that in principle one might be able to utilize the detector as a photon energy proportional device, similar to the application of junction semiconductor detectors for x-ray spectroscopy, in the very low wavelength region (500 Å to 1000 Å). This requires, however, that the signal due to a single absorbed photon be detectable. Unfortunately this latter requirement cannot be accomplished.

Morton[86] has recently discussed the subject of photon counting with solid state detectors and on the basis of a noiseless pre-amplifier he derives a signal-to-noise ratio, S/N, equivalent to

$$S/N = e\eta n t_a/2\ (kT\ C)^{1/2}$$

where e = electronic charge

η = quantum efficiency (charge carriers per photon)

n = photon flux (photons/sec)

t_a = time constant of input circuit

C = input capacitance (detector capacitance plus pre-amp circuit input capacitance).

Morton illustrates the case where $\eta = 1$, S/N = 4, and $n\ t_a$ (the number of photons in integration time t_a) equals one. The required capacitance in that case is of the order 10^{-19} farads which is so small as to make such a system completely unrealizable and impractical.

Even if we assume that $\eta = 10$ (the value in silicon for a 700 Å photon) and that one could utilize a signal-to-noise ratio of one, the required capacitance is up only to the order of 10^{-16} farads which is still small compared to the actual capacitances of 10^{-11} for the solid state detectors. Thus one would require an additional signal or charge carrier gain in the detector of 10^2 to 10^3 to make single photon detection

practical for random signals. This internal gain would have to be "noise free". Semiconductor photodetectors with internal gain have been described utilizing the avalanche amplification effect.[87,88] To date, however, none of these devices exhibit a "noise free" gain sufficient for this application.

An alternate way of stating the single photon detectivity of the semiconductor detectors is the current state-of-the-art in x-ray photon detection. Here the limitations are given for the detector and pre-amplifier combination usually in terms of noise in equivalent Kev of photon energy. These values are from 1 to 5 Kev depending upon the input capacitance. In silicon an x-ray photon creates charge carriers at an efficiency of about one charge carrier pair per 3.5 ev absorbed. Thus 1 Kev to 5 Kev is equivalent to about 300 to 1500 charge carriers per photon. Again this indicates that a carrier gain of greater than 100 would be necessary to bring the single ultraviolet photon signal up to the system noise level.

Furthermore, the resolution would be limited by the statistics of initial charge carrier production, i.e. on the standard deviations of the small number of 3 to 16. These resolutions would be very poor.

Even though this system is not useable for single photon counting in the vacuum ultraviolet energy range, for completeness, we will briefly describe the technique of semiconductor-detector pulse counting and analysis for x-ray or nuclear particle spectrometry.

The problems of pulse amplification, counting and analysis with semiconductor detectors have much in common with those of any other detecting system depending upon charge collection. However, voltage amplification type pre-amplifiers have drawbacks for use with reverse biased semiconductor detectors since the input varies with any change of bias, due to the change in detector capacitance. Better results and higher stability are obtained by the use of charge-sensitive pre-amplifiers which give output voltage pulse heights directly proportional to the charge pulse applied to the input.[89] They operate by employing negative charge feedback to the input capacitance. This feedback system is illustrated in Figure 65 which shows a block diagram of pulse height analysis system for spectrometry. The input charge is effectively transferred from C_1, the input capacitance which includes the detector capacitance and the circuit input capacitance, to the capacitance C_f which is a carefully chosen highly stable capacitor. Since Q/C_f is usually low in amplitude, a stage of low noise "post amplification" is necessary

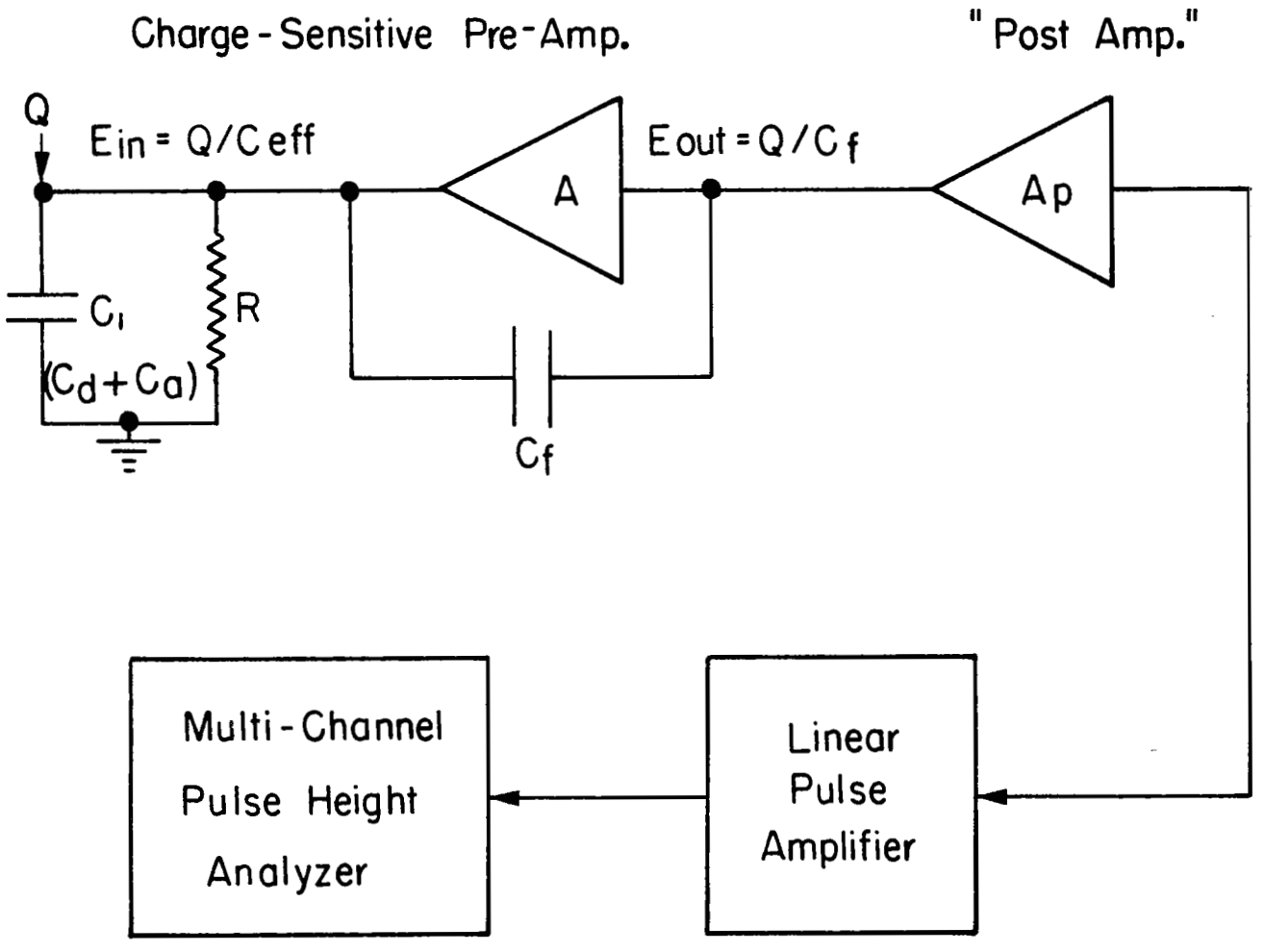

FIGURE 65. SPECTROMETRY SYSTEM FOR SEMICONDUCTOR DETECTOR.

to obtain adequate voltage pulse signals to feed the linear pulse amplifier and subsequent pulse height analyzer.* All of the above electronics has been transistorized for various space missions.

---

* It can be shown that the voltage pulses E_{in} and E_{out} are:

$E_{in} = Q/C_{eff}$, where Q is the charge pulse and

$C_{eff} = C_1 + C_f + AC_f$ (A is the amplification factor)

If AC_f is large compared to C_1 and C_f then

$E_{in} = Q/AC_f$ and $E_{out} = A\ E_{in}$, thus

$E_{out} = Q/C_f$.

3. Miniature Photodetector Arrays

Since semiconductor photodetectors can be made very small in size, a packaged array of many photodetectors is an obvious image detector. For spectroscopy a linear array could be placed at the image plane of a small vacuum ultraviolet spectrograph. Current fabrication techniques would permit a linear array to be either curved or flat to meet the focal conditions of the spectrograph. The use of a fixed array is desirable over a mechanically scanned single detector for the time resolutions needed in this application (5 spectra per second). Also it is probably not desirable to consider the use of some 30 separate signal channels, each associated with a detector element. Thus an image array scanner capable of switching electronically from many discrete radiation input points to a single output terminal is required.

The development and fabrication of solid-state image scanners has been an active field for many laboratory groups during the recent years,[90-95] and consequently several types are available. As with most imaging systems, the majority of the work is devoted to visible or IR systems. One must, therefore, extrapolate the reported sensitivity values to the vacuum ultraviolet or consider the use of wavelength shifters. It is fortunate that most of the imaging arrays developed to date utilize a silicon photodiode or phototransitor, and the photocarrier quantum efficiency of silicon has been studied under vacuum ultraviolet radiation. In a following section a discussion on the effects of surface states and surface oxide on the vacuum ultraviolet response of silicon will be presented to support the view that a silicon device is a potentially favorable choice. A photoconductor detector element of CdS has also been demonstrated in a scanned image array[95]. The advantages of a larger bandgap material such as CdS (or SnO_2) is the insensitivity of the detector to the longer wavelengths.

Characteristics of Solid-State Image Scanners

Integrated arrays of photodetectors and associated circiut elements have been fabricated by various companies and some of these arrays are available for use today. A basic design feature of these devices is electronic switching from a large number of discrete photosensitive elements to a single output terminal. The details of the electronic switching or scanning circuits are not discussed here. It is sufficient to state that these circuits have been fabricated in integrated circuits of small volume and power comsumption.

In general, for each photodetector element there is an associated blocking diode or charging diode intimate

with the photodetector element on the image sensitive array. These diodes serve as the switches for the signal interrogation of the photosensitive elements. A simple three terminal linear image array is described by Horton.[90] In this system a ramp voltage applied to the photodetector array bar terminal sequentially samples the individual pairs photodiodes and blocking diodes. Other systems require that gating pulses be applied to individual pairs of photoelements and switching diodes.

The linear arrays described have photosensitive elements set at intervals of from 5 to 2.5 mils on centers, i.e. line resolutions of 200 to 400 per inch. Horton describes a linear array of 75 elements. His photodiodes were fabricated on a 3 mil thick (76μ) silicon slab, and each junction had an area of 3 x 10 mils (1.9×10^{-4} cm^2) set at intervals of 5 mils on center. The total dark current of the array under back biased conditions was about 5×10^{-9} amps giving a dark current density of about 3×10^{-7} amps/cm^2 of photosensitive surface. This is similar to the dark current density of about 10^{-7} amps/cm^2 quoted by Tuzzolino[96] for large area silicon photodiodes.

All authors report essentially the same sensitivity of the various silicon detectors in the visible region. The observed sensitivity at the peak of the energy response curve (8000 Å to 9000 Å) is about 0.5 A/w, and the energy sensitivity then decreases as the wavelength decreases due to the increasing energy per photon and reflectivity of silicon. At 4000 Å to 5000 Å the energy sensitivity is about one-half of the peak value. If there is a thick oxide surface layer the response curve will change.

The minimum detectable signal depends upon the read-out method, the scan speed and the cross talk between elements, which becomes a problem as the density of the elements increases. Quoted detectivities for visible light vary from 0.14 ft - candles (0.23μw/cm^2) to 10^{-3} ft - candles. This latter value is reported by Weckler and Dyck[94] who used an array of silicon phototransistors (200 elements on 2.5 mil centers) scanned at 60 lines per second and operated in a photon flux integration mode.

In the photon flux integration (PFI) mode, also referred to as the storage mode, the photodetector is active during the entire scanning time, permitting readout of the integral of incident photon flux on a sampled basis. This operation is based on the principle that if a p-n junction is reversed biased, then open circuited, the charge stored on the depletion layer capacitance decays at a rate proportional to the incident

illumination level. Thus by monitoring the charge required to periodically re-establish the initial voltage condition one obtains a signal proportional to the incident illumination.

Response of Silicon Photodetectors in the Vacuum Ultraviolet

The response of silicon reverse biased photodiodes to vacuum ultraviolet radiation was shown in prior sections. This present discussion is a comparision of the visible and vacuum ultraviolet quantum efficiency and response. The interaction of incident vacuum ultraviolet photons with silicon surfaces is also presented.

In Table 17 the reflectivity, the quantum efficiency and the response of silicon photodetectors are listed for photon energies from 1.1 ev (11,300Å) up to 21.1 ev (585Å). Much of the data is from Tuzzolino, although the quantum efficiency in the visible range was measured by Vavilov[97]. The response values in parenthesis have been extrapolated on the basis of energy per photon from the corresponding response in electrons per photon or $\mu a/\mu w$. If the following assumptions are made: (1) photoemission may be neglected; (2) there is no loss of photon produced carriers due to recombination or trapping; (3) the presence of an oxide layer on the surface may be neglected; and (4) the silicon thickness is sufficient to absorb all of the photons (this is certainly true for vacuum ultraviolet photons where the silicon absorption coefficient is greater than than 10^5 cm^{-1}), then the photocurrent, I_{ph}, is

$$I_{ph} = q\eta\ (1 - R)\ N_o$$

where q = electronic charge

η = quantum efficiency (electron-hole pairs per photon)

R = reflectivity

N_o = incident photons per unit time.

Because of the increasing quantum efficiency and decreasing reflectivity the electron per photon sensitivity increases in the vacuum ultraviolet.

TABLE 17

SUMMARY OF SILICON PHOTODETECTION PROPERTIES

WAVELENGTH		REFLECTIVITY	QUANTUM EFFICIENCY	SENSITIVITY		NOTES
ev	Å	R	η	el./photon	$\mu a/\mu w$	
1.1	11300	0.30	(bandgap)			
1.5	8300	0.32	1		0.50	1, 3, 6
2.3	5460	0.35	1	(0.3)	0.31	1, 3, 5
3.4	3650	0.55	1		0.13	1, 3, 5
4.9	2540	0.65	2	0.18	0.10	2, 3, 4, 5
6.0	2060	0.60	3	0.21		2, 4, 5
10.0	1240	0.20	3	0.30	(0.1)	2, 4, 5
14.0	885	0.10	5	0.56		2, 4, 5
16.7	742	—	9.5	0.80		4, 5
21.2	585	—	15	1.1	(0.15)	4,5

NOTES:
1. Reflectivity values of fresh bulk silicon.
2. Reflectivity values of detector measured by Tuzzolino.
3. Quantum efficiency values from Vavilov.
4. Quantum efficiency values from Tuzzolino.
5. Sensitivity values from Tuzzolino.
6. Sensitivity values from various references.

It is importance to note that in most devices the collection barrier or junction is at the surface facing the incident radiation, except for the device described by Horton (the Scanistor) in which the junction was on the back side of a 76 micron thick slab of silicon. Yet Horton reports the standard sensitivity to 4000Å to 5000Å photons. The absorption of these photons in silicon is such that 90% are absorbed within 1 to 4 microns of the incident surface. Thus there was sufficient photocarrier diffusion to the back junction.

Tuzzolino's discussion of the experimental observations is pertinent to the use of silicon devices for vacuum ultraviolet detection[96]. The fatigue effect is one which must be examined more closely by further laboratory experiments. Attempts to measure the photoresponse on photodiodes which had been aged for only three or four days ("new" samples) have been unsuccessful. Not only were these new samples unstable in the environment of the sample vacuum chamber (this instability was usually evident as a varying or negligible response and at times, a very high noise level), but also exhibited irradiation fatigue at the 1216Å hydrogen line. These fatigue effects were observed after a time of irradiation varying from 10 sec to 1 min, depending upon the sample, and were observed as a sudden decrease in photosignal. After this sudden decrease, the photosignal decreased more slowly with time, dropping to a negligible value after a total time of a few minutes. The measurements were taken at an intensity of 2×10^{10} photons/sec (at 1216 Å) through a 1 x 5 mm slit. These fatigue effects were not observed at other wavelengths, possibly because of lower intensities and insufficient observation times.

Fortunately, it was found that if the photodiodes were allowed to age for at least one week, they were stable under the vacuum conditions in the sample chamber, although they were still subject to fatigue effects under the full intensity of 1216Å photons. However, by reducing the intensity at 1216Å it was possible to measure the response of the aged samples over the entire spectral range without any evidence of environmental instabilities or irradiation fatigue effects. Repeated determinations of the photoresponse of any of the aged samples agreed within experimental error.

One possible explanation for the instability of new samples under vacuum and the fatigue effects exhibited eventually by all samples is that the surface states necessary for the existance of the barrier region can be altered significantly by conditions of moderate vacuum, by high energy photon irradiation, and possibly by hydrogen ions from the illumination

source discharge tube. Sufficient alteration or loss of such surface states would result in destruction of the barrier region and consequently in a loss in photosensitivity. If these surface states result from the oxide layer or adsorbed species on this layer, it is reasonable to assume that these impurities are not tightly bound to the surface and may be altered or removed from the surface fairly easily by vacuum or bombardment, particularly when the surface is new. In most cases, the response of samples which had shown fatigue effects or instabilities was restored by removing the samples from the chamber and allowing them to age again for several days, supporting the above view.

The generally lower value of reflectivity, particularly at the shorter wavelengths, compared with published values for silicon is expected, since the magnitude and spectral detail of the reflectivity of a semiconductor are strongly dependent upon the surface quality. The published values of the reflectivity of silicon are usually obtained on fresh surfaces while the surfaces used here were purposely aged. Reflectivities below 1000Å were not measurable. Since the reflectivity for fresh surfaces is less than 0.3 at 1000Å and decreases rapidly with decreasing wavelength, the values for the aged surfaces are probably much less than 0.1 below 1000Å. A reflectivity of zero was assumed for the efficiency calculations. No attempt was made to correct for any oxide layer on the crystal surface. An oxide layer of 25 - 50Å thick and adsorbed impurities are normally present at silicon surfaces.

In considering the first assumption, any photoemission from a semiconductor such as silicon may be either a surface effect or a volume effect. In general, surface states on a semiconductor will absorb very little of the incident light. Absorption of about 10% is probably the upper limit. For most materials studied the photoemission has been found to be a volume effect.

A study of photoelectric emission from silicon has been reported for the energy range of 4.9-6.3 ev. Over this energy range the photoemission yield is less than 10^{-3} electrons per photon. The yield is interpreted as being due to a volume excitation effect and their data indicate that any photoemission from surface states is negligible. Unfortunately, no data are available over the photon range considered here. Although the yield may increase at higher photon energies, it seems unlikely that it would exceed 0.20, which appears to be the upper limit for the yield observed for similar materials

studied. Assuming the yield does attain a value of 0.20, the corrected values for η would be at most 20% higher than quoted.

The justification for the assumption of negligible loss of generated carriers in the barrier region follows from the fact that the carrier lifetimes (~400 μsec) were much longer than the carrier transit time across the barrier region (~ 10^{-9} sec). The assumption of negligible loss of photocarriers at the surface is supported by the measurements made on the seven different samples. During these measurements the surfaces were exposed to different conditions of vacuum and atmosphere. In addition, the photoresponse was measured at several applied bias voltages which gave rise to different magnitudes of electric fields at the surface of the samples. It seems reasonable to assume that the photodiode samples had significantly different surface recombination characteristics. Since the same value of efficiency was obtained for all samples, within the experimental error, any effects of recombination at the surface were small. In addition, for photon energies greater than 6 ev the importance of surface effects should decrease since the absorption coefficient of silicon decreases with increasing energy above 6 ev.

Although the effects of the oxide film on the recombination of photocarriers at the surface appears to be small, the same is not necessarily true of the effect of the oxide-film optical absorption on the number of photocarriers produced in the silicon. No detailed information is available on the physical or optical properties of oxide films on silicon so that it is not possible to predict quantitatively the effect such films may have. However, one may estimate the amount of absorption by these films if it is assumed that the absorption coefficient lies in the range of 10^5-10^6 cm^{-1} for photon energies above that where the fundamental absorption sets in. Assuming the fundamental absorption by the oxide film is important above 8 ev (as is indicated by published data) and choosing a value of 10^6 cm^{-1} for the absorption of the oxide, the measured values of η would be too small by a factor of about 1.4 for a 40Å thick film. Hence, the assumption that the effect of the oxide film is negligible may not be valid, and the use of the quoted silicon quantum efficiency values are certainly indicative of the practical device sensitivity, and the general dependence of η on photon energy is characteristic of bulk silicon.

Application to Spectrometer

If we take the visible detectivity of the Scanistor of 0.2 μ w/cm^2 and a sensitivity of 0.5 μ A/μ w, the

number of photocarrier electrons can be calculated. This is,

$$0.2\ \mu\ w/cm^2 \times 0.5\ \mu A/\mu w \times 6.2 \times 10^{12}\ \text{electron/sec-}\mu A$$

Using a value of 0.3 electron/photon for the sensitivity at midrange of the desired spectrum, the required number of incident photons for minimum detectability is

$$2.1 \times 10^{12}\ \text{photons/sec-cm}^2.$$

Assume a spectrometer with a slit height of 3 mm and a dispersion of 50Å/mm. At a resolution of 2 elements per 50Å band each element could be 0.4 mm wide, giving an element area of 1.2×10^{-3} cm^2. (Note that these element sizes and spacings are easily within the realm of the fabrication art). The required number of incident photons per element is then

$$2.5 \times 10^{9}\ \text{photons / sec.}$$

If the spectrometer has a total thruput efficiency of 10^{-6}, a 50Å band of the initial intensity of 10^{17} photons/sec will be imaged at an intensity of 10^{11} per sec per mm and the element will see 4×10^{10} photons/sec. This intensity is ten times the minimum detectable. An improved signal will, of course, be obtained with an increased spectrometer efficiency, which is likely. Also, the use of the storage mode (PFI) of operation and phototransistors will improve the detectivity if necessary.

One concern is the reported fatigue or radiation effects observed under vacuum ultraviolet irradiation. This will have to be experimentally determined. If the effect is found to be a serious limitation, it is possible to use a wavelength shifter to protect the silicon. The sensitivities with a wavelength shifter will be reduced by a factor of about ten.

IV PRELIMINARY SYSTEM DESIGN AND CALIBRATION

Spectrometer Design

Based on the evaluation of the various detector-spectrometer systems, the most favorable device appears to be a wavelength-dispersing system followed by a miniature diode

array. Such a system has a high degree of reliability and the ability to obtain high-resolution spectral measurements of both the relative and absolute radiation levels. Actually, the diode array might be improved by an array of photoconductors if these operate above the noise. Based on the flux levels available from the proposed grating, the diode array detectors may be operating very close to their noise levels. In such a case, the flux integration mode of operation may be advantageous.

Photoelectric cathode with retardation grid analyzers also show promise as future detectors in high vacuum situations. However, with the required helium window, their employment would be difficult. Other complications arise, first because of the use of filters or two to three analyzers to obtain the desired resolution, and second due to required differential pumping for the region below 1050Å. The reliability and resistance to g-loading and vibration are also unknown for these analyzers.

Wavelength shifters and systems based on wavelength filters for certain spectral regions are possible and may be desirable for total flux measurements, but they cannot attain the 50Å resolution without undue complications. The remaining detectors, namely photomultipliers and ionization chambers, with the exception of channel multipliers, can be successfully employed for the region above 1050Å alone and with a wavelength shifter, such as sodium salicylate (if aging fall off is avoided), can cover the remaining 1050 to 500Å region, however, they are quite large. Also, the connection of a large number of such devices electronically may be quite difficult. Channel multipliers, which will probably be affected by the helium atmosphere, are of the ideal size when considering photomultipliers.

An initial system design is the heat shield orifice followed by the entrance slit of a grating spectrometer. The entrance slit is imaged on an array of detectors to monitor the radiation between 500 and 2000Å. The need for a transparent window necessitates filling the cavity with helium maintained at a slight positive pressure to prevent the ingress of ionized gases. A spectrometer having a concave grating of 20 cm radius, a ruling of 1200 lines/mm, and operating in the first order has a plate factor (reciprocal dispersion) of approximately 50Å/mm. Thus with three to four detector elements per mm the resolution requirement can easily be met. Due to second-order overlap at 1000Å, the first-order region between 1000 and 2000Å may have to be covered with a LiF filter. Data for the expected response from such a spectrometer has been presented in earlier sections.

An actual grating would depend on the exact size of the spectrometer cavity. Prices vary from $350 to $3000 for stock gratings. The platinum coating is $150 extra. In some cases a specially designed grating is required for optimum performance.

Thus far no one has measured the vacuum UV response of miniature diode arrays. Such measurements are essential since the entire spectrometer relies on the detector, and no meaningful estimate of the flight model cost can be made until this information is known. If a detector system can be established for the VUV region, design of the spectrometer optical system should follow. Parameters related to the detector shape will determine the grating and general optical configuration.

The grating-detector array system should have a high level of reliability since there are no moving parts. A simple electronic scan technique, such as the scanistor, will also improve the reliability. The need for a cooling system will depend on the final optical configuration and the removal of longer wavelength radiation. Additional investigations should be made on the fatigue and radiation effects of silicon.

Calibration

Absolute intensity calibrations in the XUV present a problem, as there are no standards. The closest one can get to an absolute source is synchrotron radiation from an electron synchrotron[98]. Here the theory is presented sufficientrly well for one to have confidence in the calculated absolute intensity of the polarized radiation. Such a calibration source is rather inconvenient but could be used if necessary and would cover the whole wavelength range of interest here.

Other methods of calibration which have been suggested or used are the thermopile and ionization chambers. When coated with gold black, the thermopile has an absorptance that is very nearly unity, and so has a flat spectral response[99]. On account of its very low sensitivity, the thermopile is not a convenient device for the far ultraviolet, where laboratory sources are weak. Samson reports that the ionization efficiency of the rare gases is unity below certain wavelengths (1350Å for Ne) so that these may also be used as absolute detectors, against which other detectors can be calibrated. A third method is employing sodium salicylate, which has a quantum efficiency that is very nearly flat in the spectral range of interest. The detector, possibly a photomultiplier, is coated

with a thin layer of this compound and then calibrated at one point. This point is taken as 1216Å, the wavelength of hydrogen Lyman-α, for which Watanabe has given the quantum efficiency of NO, so that an ionization chamber containing NO yields the absolute calibration. Mention may be made of one more method which has been used in ultraviolet calibrations--actinometry; this technique does not seem to have been applied at wavelengths shorter than 1750Å and there may be good reasons why. Hence until tried, it would be well to discount this method.

Recommendations for Future Work

1) Actual measurements of the sensitivities and detectivities of miniature diode arrays to vacuum UV radiation.

2) Detailed design of a grating system to provide the required radiation flux levels and dispersion for proper evaluation of the detectors in the vacuum UV region.

REFERENCES

1. D. L. Cauchon, Private Communication, NASA, Langley Research Center.
2. W. A. Page and J. O. Arnold, NASA TR R-193, April 1964.
3. A. Seiff and M. E. Tauber, "Minimization of the Total Heat Input for Manned Vehicles Entering the Earth's Atmosphere at Hyperbolic Speeds," NASA TR R-236, May 1966.
4. E. Sullivan, Private Communication, NASA, Langley Research Center.
5. T. H. Slocumb, Jr. and R. W. Buchan, Private Communication, NASA, Langley Research Center.
6. A. Muzyka and H. E. Blanton, "Optimum Earth Reentry Corridors," NASA CR-394, March 1966.
7. U. S. Standard Atmosphere, 1962, NASA, USAF, and U. S. Weather Bureau.
8. E. B. Pritchard, J. Spacecraft and Rockets 1, (6), 605, December 1964.
9. H. Lomax and M. Inouye, "Numerical Analysis of Flow Properties About Blunt Bodies Moving at Supersonic Speeds in an Equilibrium Gas," NASA TR R-204, July 1964.
10. J. T. Howe and J. R. Viegas, "Solutions of the Ionized Radiative Shock Layer, Including Reabsorption and Foreign Species Effects, and Stagnation Region Heat Transfer," NASA TR R-159, 1963.
11. H. Hoshizaki and K. H. Wilson, AIAA Journal 3, (9), 1614, September 1965.
12. A. Seiff, "Recent Information on Hypersonic Flow Fields," in Pac. NASA-University Conference on the Science and Technology of Space Exploration, Vol. 2, 1962-NASA SP-11.
13. A. J. Eggers and N. B. Cohen, "Progress and Problems in Atmosphere Entry," in Propulsion and Reentry, p.399, Ed. Michal Lunc, Gordon and Breach, New York, 1966.
14. B. Kivel, J. Aero Space Sci. 28, 96, 1961.
15. T. N. Canning and W. A. Page, "Measurements of Radiation from the Flow Field of Bodies Flying at Speeds up to 13.4 Kilometers per Second," in The High Temperature Aspects of Hypersonic Flow, Ed. W. C. Nelson, The MacMillan Company, New York, 1964, p.569.
16. B. H. Wick, "Radiative Heating of Vehicles Entering the Earth's Atmosphere," in The High Temperature Aspects of Hypersonic Flow, Ed. W. C. Nelson, The MacMillan Company, New York, 1964, p.607.
17. R. A. Allen, "Air Radiation Graphs: Spectrally Integrated Fluxes Including Line Contributions and Self Absorption," AVCO - Everett Research Report 230, September 1965.
18. P. J. Bobbitt, "Effects of Shape on Total Radiative and Convective Heat Inputs at Hyperbolic Entry Speeds," Advances in the Astronautical Sciences Vol. 13, 1963, Ed. E. Burgess, p.290.

REFERENCES (CONTINUED)

19. H. Hoshizaki and K. H. Wilson, "Convective and Radiative Heat Transfer During Superorbital Entry," NASA CR-584, September 1966.
20. H. J. Allen, "Gas Dynamics Problems of Space Vehicles," p.251 of NASA SP-11, December 1962.
21. P. C. Stainback, "Convective and Equilibrium Radiation Heat Transfer Predictions for Project Fire Reentry Vehicle," NASA TN D-2867, July 1965.
22. L. Dunkelman, "Ultraviolet Photodetectors," NASA TN D-1718, 1963.
23. A. K. Stober, "Ceramic Vacuum Ultraviolet Ion Chambers," NASA TN D-1180, March 1962.
24. A. K. Stober, R. Scholnik, J. P. Hennes, Appl. Optics 2, 735, July 1963.
25. H. Friedman, T. A. Chubb, J. M. Siomkajlo, "A Manual on Molecular Oxygen Determination for the IQSY," COSPAR Working Group II for the IQSY, June 4th, 1964. A64-18683.
26. S. A. Korff, H. Kallmann, Electron and Nuclear Counters, D. Van Nostrand Co., Inc., New York, 1955.
27. H. Friedman, "Geiger Counter Tubes," Proc. IRE, 37, 791, 1949.
28. T. A. Chubb, H. Friedman, "Photon Counters for the Far Ultraviolet," Rev. Sci. Insts., 26, 493, 1955.
29. N. N. Axelrod, "Volume Photoelectric Effect in Metals," J. Opt. Soc. Amer. 56, 203, 1966.
30. G. L. Weissler, Handbuch der Physik, S. Flugge, Ed., Springer-Verlag, Berlin 1956, Vol. XXI, p. 304.
31. L. Dunkelman, W. B. Fowler, and J. Hennes, Appl. Optics 1, 695, 1962.
32. L. Dunkelman, "Ultraviolet Photodetectors," NASA TN D-1718, 1963.
33. J. Sharpe, "Photoelectric Cells and Photomultipliers," Publication of EMI Ltd. U.K.
34. L. Heroux and H. E. Hinteregger, Rev. Sci. Insts. 31, 280, 1960.
35. G. W. Goodrich and W. C. Wiley, Rev. Sci. Insts. 32, 846, 1961.
36. A. F. Timothy, J. G. Timothy, and A. P. Willmore, "The Performance of Open Structure Photomultipliers in the 1100-Å to 250-Å Wavelength Region," Applied Optics 6, 1319, 1967.
37. G. W. Goodrich and W. C. Wiley, Proceedings of the Image Intensifier Symposium, NASA SP-2, June 1962.
38. Oschepkov. et al. Pribory i Tekhnika Eskperimenta 4, 89, 1960.

REFERENCES (CONTINUED)

39. W. R. Hunter, "Extreme Ultraviolet Detection with the Bendix Channel Multiplier," Space Research, III, Ed. W. Priester, Interscience Pubs. 1963, p.1187.
40. J. Adams and B. W. Manley, Electron. Eng. 37, 180, 1965.
41 J. Adams and B. W. Manley, Philips Tech. Rev. 28, 156, 1967.
42. D. J. Michels and W. R. Hunter, Appl. Optics 6, 384, March 1967.
43. W. R. Shockley and J. R. Pierce, Proc. I.R.E. 26, 321, 1938.
44. A. Rose, "Photoconductivity in Perspective," J. Phys. Chem. Solids 22, 1, 1961.
45. F. D. Morten and R. E. J. King, "Photoconductive Indium Antimonide Detectors," Appl. Optics, 4, 659, 1965.
46. R. H. Buba, Photoconductivity of Solids, John Wiley and Sons, Inc., New York, 1960, p.230.
47. H. Levinstein, "Extrinsic Detectors," Appl. Optics, 4, 639, 1965.
48. R. C. Jones, Proc. Inst. Radio Engrs. 47, 1498, 1959.
49. A. Smith and D. Dutton, "Ultraviolet Sensitivity of Lead Slufide Photocells," University of Rochester report to AFOSR, Contract AF 18 (600)-193, December 1957.
50. J. S. Humphrey, Appl. Opt. 4, 665,1965.
51. T. H. Johnson, H. T. Cozine, and B. N. McLean, Appl. Opt. 4, 693, 1965.
52. Private communications with Joseph Mudar, IRIA, Willow Run Laboratories, University of Michigan.
53. E. Mollow, "Electrical and Optical Properties of ZnO," in Photoconductivity Conference, Ed. R. G. Breckenridge, John Wiley & Sons, Inc., New York, 1954, p.509.
54. M. L. Schultz and W. E. Harty, Private communications, RCA Laboratories.
55. Y. Nakai and K. Teegarden, "Photoconductivity in RbI and KI," J. Phys. Chem. Solids 22, 327, 1961.
56. G. Kuwabara and K. Aoyagi, "Photoconductivity of Some Alkali Halide Crystals in the Fundamental Absorption Range," J. Phys. Chem. Solids 22, 333, 1961.
57. E. Becquerel, "On Electric Effects Under the Influence of Solar Radiation," Compt. Rend. 9, 561, 1839.
58. C. G. B. Garrett and W. H. Brattain, "Interfacial Photo-effects in Germanium at Room Temperature," in Photo-conductivity Conference, Ed. R. G. Breckenridge, John Wiley & Sons, Inc., New York, 1954, p.298.
59. R. H. Buba, p.382.

REFERENCES (CONTINUED)

60. "Research Directed Toward the Improvement of the Efficiency of Silicon Batteries by Utilization of Unabsorbed Photons," AFCRL-475, Technical Operations, May 1961.
61. L. R. Koller, Ultraviolet Radiation, John Wiley & Sons, Inc., New York, 1965, p.295.
62. V. K. Zworykin and E. G. Ramberg, Photoelectricity and Its Application, John Wiley & Sons, Inc., New York, 1949, p.213.
63. W. Shockley, Bell Systems Tech. J. 28, 435, 1949.
64. J. L. Moll, Proc. IRE 46, 1076, 1958.
65. G. R. Pruett and G. L. Petritz, Proc. IRE 47, 1524, 1959.
66. M. R. Holten, et. al., "Fundamentals of Infrared Technology," The MacMillan Co., New York, 1962.
67. A. J. Tuzzolino, et. al., J. Appl. Phys. 33, No. 1, 148, 1962.
68. A. J. Tuzzolino, Rev. Sci. Instr. 35, No. 10, 1332, 1964.
69. R. Takaki, et. al., IRE Trans. on Nuclear Science NS-8, No. 1, 64, 1961.
70. R. C. Ropp, J. Opt. Soc. Am. 57, 1240, 1967.
71. K. Watanabe and E. Inn, J. Opt. Soc. Am. 43, 32, 1953.
72. R. Allison, et. al., J. Opt. Soc. Am. 54, 747, 1964.
73. D. H. Thurnau, J. Opt. Soc. Am. 46, 346, 1956.
74. R. L. Conklin, J. Opt. Soc. Am. 49, 669, 1959.
75. A. Bril and W. van Meurs - Hoekstra, Philips Res. Repts. 19, No. 3, 296, 1964.
76. R. Sussmann, et. al., Phys. Status Solidi (Germany) 9, No. 3, K173, 1965.
77. G. Gergely, et. al., J. Phys. Chem. Solids 24, 687, 1963.
78. E. R. Ilmas, et. al., Optics and Spect. (USA) 18, No. 3, 255, 1965.
79. James A. R. Samson, "Techniques of Vacuum Ultraviolet Spectroscopy," Johy Wiley & Sons, Inc., 1967, pp. 212-216.
80. Allan Shepp, "The Index of Refraction Effect on Absolute Fluorescence Measurements," AFOSR-TN-56-184, April, 1955.
81. L. Heroux and H. E. Hinteregger, "Photoelectron Energy Distribution Measurements for 10 to 50 eV Photons with a Planar Analyzer and Electron Multiplier," Appl. Optics, 1, (6), 701, 1962.
82. H. E. Hinteregger, K. R. Damon and L. A. Hall, "Analysis of Photoelectrons from Solar Extreme Ultraviolet," J. Geophys. Res., 64 (8), 961, 1959.
83. L. Heroux, R. G. Newburgh, W. J. McMahan and H. E. Hinteregger, "Detection of Extreme Ultraviolet Radiation by Retarding Potential Analyzers," Appl. Optics, 7 (1), 37, 1968.

REFERENCES (CONTINUED)

84. C. N. Berglund and W. E. Spicer, "Photoemission Studies of Copper and Silver: Experiment," Phys. Rev., 136 (4A), 1044, 1964.
85. G. L. Weissler, "Photoionization in Gases and Photoelectric Emission from Solids," Handbuch der Physik, Vol. 21, p. 304.
86. G. A. Morton, Appl. Optics 7, 1, 1968.
87. R. B. Emmons, J. Appl. Phys. 38, No. 9, 3705 (1967).
88. R. J. Locker and G. C. Huth, Appl. Phys. Letters 9, No. 6, 227, 1966.
89. E. Fairstein, IRE Trans. on Nuclear Science NS-8, No. 1, 129, 1961.
90. J. W. Horton, et. al., Proc. IEEE 52, 1513, 1964.
91. M. A. Schuster and W. F. List, Trans. of Met. Soc. of AIME 236, 375, 1966.
92. R. A. Anders, et. al., IEEE Proc. of WESCON 1967, paper 13/1, 1967.
93. G. P. Weckler, Electronics 40, No. 9, 75, 1967.
94. G. P. Weckler and R. H. Dyck, IEEE Proc. of WESCON 1967, paper 13/2, 1967.
95. P. K. Weimer, et. al., IEEE Proc. of WESCON 1967, paper 13/3, 1967.
96. A. J. Tuzzolino, Phys. Rev. 134, A205, 1964.
97. U. S. Vavilov, Phys. and Chem. Solids 8, 223, 1958.
98. K. Codling and R. P. Madden, "Characteristics of the Synchrotron Light from the NBS 180-MeV Machine," J. Appl. Phys. 36, 380, 1965.
99. J. A. R. Samson, "Absolute Intensity Measurements in the Vacuum Ultraviolet," J. Opt. Soc. Amer. 54, 6, 1964.

"The aeronautical and space activities of the United States shall be conducted so as to contribute . . . to the expansion of human knowledge of phenomena in the atmosphere and space. The Administration shall provide for the widest practicable and appropriate dissemination of information concerning its activities and the results thereof."

—NATIONAL AERONAUTICS AND SPACE ACT OF 1958

NASA SCIENTIFIC AND TECHNICAL PUBLICATIONS

TECHNICAL REPORTS: Scientific and technical information considered important, complete, and a lasting contribution to existing knowledge.

TECHNICAL NOTES: Information less broad in scope but nevertheless of importance as a contribution to existing knowledge.

TECHNICAL MEMORANDUMS: Information receiving limited distribution because of preliminary data, security classification, or other reasons.

CONTRACTOR REPORTS: Scientific and technical information generated under a NASA contract or grant and considered an important contribution to existing knowledge.

TECHNICAL TRANSLATIONS: Information published in a foreign language considered to merit NASA distribution in English.

SPECIAL PUBLICATIONS: Information derived from or of value to NASA activities. Publications include conference proceedings, monographs, data compilations, handbooks, sourcebooks, and special bibliographies.

TECHNOLOGY UTILIZATION PUBLICATIONS: Information on technology used by NASA that may be of particular interest in commercial and other non-aerospace applications. Publications include Tech Briefs, Technology Utilization Reports and Notes, and Technology Surveys.

Details on the availability of these publications may be obtained from:

SCIENTIFIC AND TECHNICAL INFORMATION DIVISION

NATIONAL AERONAUTICS AND SPACE ADMINISTRATION

Washington, D.C. 20546